TÉCNICO LISBOA

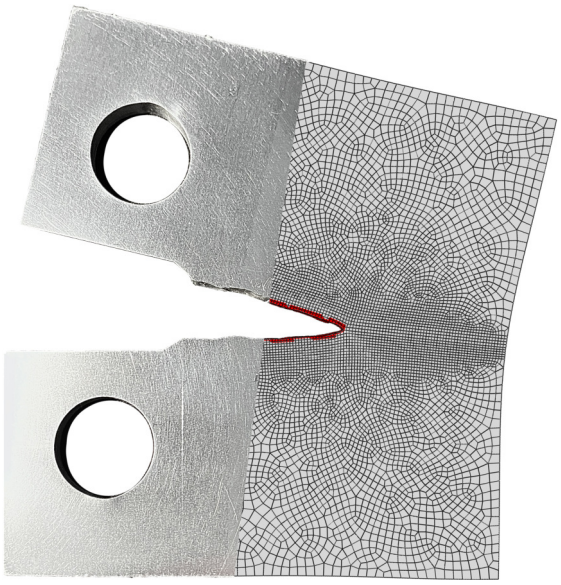

# Fatigue Crack Propagation in Friction Stir Welded Aluminium Alloy 5083

Experimental and Numerical Analysis

**Nikita Kaminskyy**

Thesis to obtain the Master of Science Degree in

## Aerospace Engineering

Supervisors: Prof. Virgínia Isabel Monteiro Nabais Infante
Prof. Daniel Filipe Oliveira Braga

### Examination Committee

Chairperson: Prof. Fernando José Parracho Lau
Supervisor: Prof. Daniel Filipe Oliveira Braga
Member of the Committee: Prof. Pedro Miguel Guimarães Pires Moreira

**January 2021**

Dedicated to my parents for helping me get through these (too) many years of madness.

*Modern problems require modern solutions.*

# Acknowledgments

First and foremost, I would like to acknowledge my deep gratitude to both my supervisors, Professor Virgínia Infante and Professor Daniel Braga, for all their tireless guidance and support throughout this research, who always strived to solve any difficulty that arose along the way. I extend my gratitude to Fundação para a Ciência e a Tecnologia (FCT) project PTDC/EME-EME/29340/2017—DisFri and project PTDC/EME-EME/29339/2017 – MIAMI, whose valuable funding made this investigation possible.

Additionally, several people who directly impacted this investigation are to be acknowledged in the following paragraphs.

Professor Patrizia Paradiso, who guided me throughout the surface roughness measurements and showed her entire availability in any question that I had (and I had many).

João Marques, who guided me during tensile tests and always gave his honest opinions and suggestions for any thesis-related questions.

Mr. Pedro and Mr. João, for their technical and expert assistance, either concerning the material machining or any other laboratory concerning question.

Vasco Centeno, Francisco Lopo, and André Painha, for not only their friendship but also their deep knowledge in *Matlab* and *Photoshop*.

Furthermore, I would like to thank my family, my girlfriend, my friends, and colleagues for helping me complete this entire journey from the very beginning. Their unconditional emotional support, love, and friendship made it look like ”smooth sailing on rough seas”.

Last but not the least, I would like to thank Instituto Superior Técnico (IST) as a whole for teaching me one of the most important skills required nowadays - resilience (also known as *desemerda-te* in Portuguese).

# Resumo

A redução do peso das estruturas associada a uma procura de economizar combustível, estão entre os principais desafios enfrentados atualmente pela indústria aeroespacial. Numa área altamente regulamentada, onde todas as tecnologias devem ser comprovadas antes de serem aprovadas, superar os requisitos adjacentes a estas sem comprometer a segurança e o desempenho da próxima geração de veículos aeroespaciais, é de máxima prioridade quando se trata de implementar novas técnicas de ligação entre componentes e avaliar o seu desempenho em condições de operação.

Assim, este estudo aborda um problema comum, responsável por grande parte das falhas em estruturas submetidas a condições de carregamento cíclico, nomeadamente a fadiga. Em particular, esta investigação foca-se no estudo da Propagação de Fenda por Fadiga (PFF) em duas chapas de liga de alumínio não tratável termicamente, unidas com uma técnica de soldadura inovadora denominada por Soldadura por Fricção Linear (SFL).

Com base no trabalho já existente acerca do tema em estudo, foi realizada uma investigação multidisciplinar numa junta de topo a topo, para avaliar seu comportamento quando submetida à PFF. Esta pesquisa incluiu uma caracterização aprofundada do material, onde foram realizados ensaios de tração, juntamente com a técnica de Correlação Digital de Imagem (CID) para medições de campos de extensão, análise de microestrutura e microdureza, bem como medições de rugosidade superficial da junta. Além disso, foi desenvolvido um estudo numérico de PFF recorrendo a um software de Engenharia Assistida por Computador (EAC) com a ajuda do Método de Elementos Finitos eXtendidos (MEFX).

De entre os dados obtidos, destaca-se o desempenho mecânico da junta que demonstrou resultados inconsistentes, maioritariamente devido à existência ao defeito de Kissing Bond (KB) encontrado durante a análise à microestrutura da junta. Por outro lado, a análise numérica feita demonstrou capacidades promissoras em complementar ou mesmo substituir os estudos experimentais, desde que o modelo esteja corretamente configurado dentro do software.

**Palavras-chave:** Soldadura por Fricção Linear, Propagação de Fenda por Fadiga, MEFX, Ligas de Alumínio Não Tratáveis Termicamente

# Abstract

Fuel economy and weight reduction are among key challenges currently faced by the aerospace industry. In an already highly regulated field, where every technology must be proven before it is approved, overcoming these without compromising the safety and performance of the next generation of air and space vehicles is a top priority when it comes to employing new joining techniques and evaluating its performance in operating conditions.

Ergo, this study tackles a common problem responsible for a great part of failures in engineering structures subjected to cyclic loading conditions, fatigue. In particular, this investigation focuses on Fatigue Crack Propagation (FCP) in two non heat-treatable aluminium alloy sheets joined with an innovative solid-state joining method dubbed Friction Stir Welding (FSW).

Building on the existent work available on this matter, a multi-subject investigation was performed on the FSWed butt joint to assess its behaviour when subjected to FCP. The research included an in-depth material characterization, and evaluation, where tensile tests paired with Digital Image Correlation (DIC) for strain field measurements, microstructure and microhardness analysis, as well as surface roughness measurements were done. Additionally, a numerical study of FCP was developed within a Computer-Aided Engineering (CAE) software with the help of the eXtended Finite Element Method (XFEM).

Among the obtained data, the mechanical performance of the joint revealed inconsistent results mostly due to the existence of the Kissing Bond (KB) defect found during microstructure analysis. The numerical analysis demonstrated promising capability in complementing or even replacing the experimental studies as long as correctly modelled into the software.



**Keywords:** Friction Stir Welding, Fatigue Crack Propagation, XFEM, Non-Heat Treatable Aluminium Alloy

# Contents

# List of Tables

# List of Figures

# Nomenclature

## Acronyms

| | |
|---|---|
| **ASTM** | **A**merican **S**ociety for **T**esting and **M**aterials |
| **AS** | **A**dvancing **S**ide |
| **BC** | **B**oundary **C**onditions |
| **BM** | **B**ase **M**aterial |
| **CAD** | **C**omputer-**A**ided **D**esign |
| **CAE** | **C**omputer-**A**ided **E**ngineering |
| **CA** | **C**onstant **A**mplitude |
| **CCT** | **C**enter-**C**racked **T**ension |
| **CT** | **C**ompact **T**ension |
| **DIC** | **D**igital **I**mage **C**orrelation |
| **EDM** | **E**lectro **D**ischarge **M**achining |
| **FAA** | **F**ederal **A**viation **A**dministration |
| **FCP** | **F**atigue **C**rack **P**ropagation |
| **FE** | **F**inite **E**lement |
| **FM** | **F**racture **M**echanics |
| **FPS** | **F**rames **P**er **S**econd |
| **FSW** | **F**riction **S**tir **W**elding |
| **HAZ** | **H**eat **A**ffected **Z**one |
| **IATA** | **I**nternational **A**ir **T**ransport **A**ssociation |
| **KB** | **K**issing **B**ond |
| **LEFM** | **L**inear **E**lastic **F**racture **M**echanics |

**NASA** **N**ational **A**eronautics and **S**pace **A**dministration

**RS** **R**etreating **S**ide

**SEM** **S**canning **E**lectron **M**icroscope

**SIF** **S**tress **I**ntensity **F**actor

**SMRT** **S**urface **M**echanical **R**olling **T**reatment

**SZ** **S**tir **Z**one

**TMAZ** **T**hermo-**M**echanically **A**ffected **Z**one

**TTT** **T**ransient **T**hermal **T**ensioning

**TWI** **T**he **W**elding **I**nstitute

**USB** **U**niversal **S**erial **B**us

**UTS** **U**ltimate **T**ensile **S**trength

**VA** **V**ariable **A**mplitude

**WLI** **W**hite **L**ight **I**nterferometry

**WN** **W**eld **N**ugget

**XFEM** e**X**tended **F**inite **E**lement **M**ethod

# Symbols

$\Delta K_{th}$ Treshold stress intensity factor

$\nu$ Poisson's ratio

$\sigma_a$ Stress amplitude

$\sigma_c$ Critical stress

$\sigma_f$ Stress at fracture

$\sigma_m$ Mean stress

$\sigma_r$ Stress range

$\sigma_y$ Yield Strength

$\sigma_{max}$ Maximum stress

$\sigma_{min}$ Minimum stress

$\sigma_{UTS}$ Ultimate Tensile Strength

| | |
|---|---|
| $a$ | Crack length |
| $E$ | Young's modulus |
| $f$ | Frequency |
| $G$ | Energy release rate |
| $G_c$ | Critical energy release rate |
| $K$ | Stress Intensity Factor |
| $K_{Ic}$ | Fracture toughness |
| $N$ | Number of fatigue cycles |
| $P$ | Potential energy |
| $R$ | Stress ratio |
| $R_a$ | Arithmetic mean deviation linear roughness |
| $Y$ | Shape factor |

# Chapter 1

# Introduction

## 1.1 Motivation

The aerospace industry is constantly bombarded with new and formidable challenges where innovative techniques and attractive solutions are getting harder to find with each passing day. The ever increasing demand to reduce the weight of components and the demand for hybrid structures has increased in the recent past. Requirements for an adequate joining process between similar and dissimilar materials have been established and researched since.

For the past century, aluminium alloys have been extensively used in aviation making up to 75% - 80% of a modern aircraft [1]. Its extensive use results from the fact that these materials present an attractive combination of properties, including high strength-to-weight ratio, good thermal stability and exceptional corrosion resistance [2].

Welding metal alloys to one another could have a major application in aerospace structures where the need for more fuel-efficient and environmentally friendly aircraft, without sacrificing its safety and reliability, has become a top priority. However, welding of aluminium alloys using traditional welding methods is a difficult task due to the un-weldability of most of them, more defects in weldment, presence of aluminum oxide film, among others [3]. This is where Friction Stir Welding (FSW) comes in - a novel solid-state joining process that uses frictional heat generated by a rotating tool to join materials without melting them in the process [4].

As this technique reaches the early stage of commercial use, with great emphasis on transportation, a considerable amount of research [5–13] has already been conducted on Fatigue Crack Propagation (FCP) behaviour of FSWed aluminium alloys. Acknowledging the fact that fatigue is usually the dominant failure mode for components in service, especially for weldments, it is of utmost importance to have a good understanding of the performance of FSWed joints under cyclic loading conditions. This study will also present a Finite Element (FE) model of Compact Tension (CT) specimen under fatigue, in order to compare experimental and numerical results obtained in a commercially available FE analysis software Abaqus.

It's important to understand that aerospace manufacturing is a highly regulated field that requires

constant certification and long validation processes where new technologies have to be proven before they are applied. In light of this and with the aim to expedite the finding of an effective solution to the challenges of joining materials with FSW, this master's thesis attempts to summarize the current state of the art and provide data and information that can hopefully be useful for researchers in the near future.

## 1.2 Objectives

The main objective to be fullfilled within this research is to investigate FCP in FSWed non heat-treated aluminium alloy sheets and validate it with simulations in a Computer-Aided Engineering (CAE) software with the help of eXtended Final Element Method (XFEM). This broad topic can be split into several questions to be answered during this study:

- What mechanical and microstructural properties do the FSWed material present and how can they influence the outcome of FCP?
- How does the crack behave when crossing characteristic FSW regions?
- What capabilities does the Abaqus offer in FCP analysis and how reliable are the results when compared to the experimental study?

## 1.3 Thesis Outline

In order to address all the challenges of this master's thesis, the following structure has been adopted:

- **Chapter 2 - State of the Art**

  A detailed background review on the matter is performed regarding the FSW process, an overview on Linear Elastic Fracture Mechanics (LEFM), FCP with great emphasis in FSWed aluminium alloys, and the application of XFEM in FCP simulations.

- **Chapter 3 - Methodology**

  This chapter is split into three major sections: Material Characterization, Experimental Setup, and Final Element Model. In the first, detailed material characterization is made regarding tensile, microhardness, and microstructure analysis. Next, a description of the experimental tests for FCP is made. Finally, an explanation of how the FE model was created in Abaqus, and step by step guide to recreate it is given.

- **Chapter 4 - Results**

  Critical analysis of achieved experimental and numerical results.

- **Chapter 5 - Conclusions**

  Final conclusions are written and future outlook in regard to the work completed and studied are suggested.

# Chapter 2

# State of the Art

This chapter presents an overview of the FCP process itself and its importance in engineering, as well as some insights about LEFM and XFEM. Although FSW will not be under the spotlight of this chapter nor this master's thesis overall, it is important to present to the reader an overview of this technique in addition to its actual and potential applications in the aerospace industry. Several papers will be referenced to establish the state of the art in terms of the FCP in FSWed aluminium alloys as well as XFEM capabilities in FCP investigation.

## 2.1 Friction Stir Welding

Techniques for joining materials are becoming increasingly important in the manufacturing of hybrid structures and components for engineering applications. Welding is one of them and has been part of the aerospace industry for many years. It consists in joining materials, usually metals or thermoplastics, by using heat to melt the parts together and allowing them to cool causing fusion.

Although FSW has *welding* in its name, this process differs from conventional fusion welding. It is essentially a solid-state joining process that is both efficient, environmentally friendly, and versatile in its applications that doesn't require any filler material - virtually any alloy can be joined without consideration of the compatibility of composition as opposed to conventional welding methods where compatibility is an issue [14].

### 2.1.1 Process description

FSW was developed and patented by The Welding Institute (TWI) of UK in 1991 as a solid-state joining technique, and it was originally used to join Al. It can be applied to similar as well as dissimilar materials that have been used and researched in the recent past. In particular, it can be used to join high-strength aerospace aluminium alloys and other metallic alloys, such as titanium alloys, that are hard to weld by conventional fusion welding.

The basic concept of FSW is simple. A non-consumable rotating tool with a specially designed pin and shoulder is inserted while rotating into the abutting edges of sheets or plates to be joined and

traversed along the line of joint as can be seen in Figure 2.1. The tool serves two primary functions: heating of the work-piece via friction and material flow to produce the joint. Generated heat softens the material around the pin and a combination of tool rotation and translation leads to the movement of material from the front to the back of the pin. As a result, a joint is produced in 'solid-state' [15], without the phase transformation as it happens in conventional fusion welding.

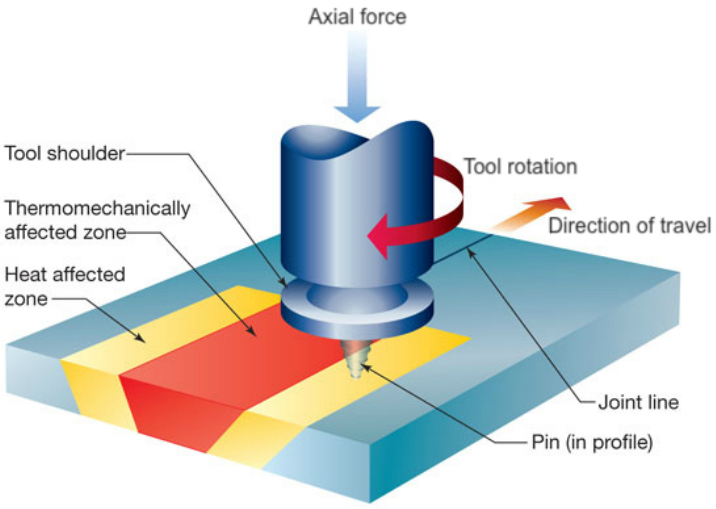


Figure 2.1: Detailed visual representation of FSW. Adapted from [16]

The entire process can be divided into four major phases [17], represented in Figure 2.2:

1. **Plunge phase** - The rotation of the welding tool is initiated and the tool slowly plunges into the workpiece. As the material is relatively cold, only the pin is in contact with the workpiece. The axial force and the torque applied to the tool are high, and in most cases, reach their highest values. At the end of the plunge phase, the pin has fully penetrated the workpiece and the shoulder is in contact with the upper surface of the workpiece.

2. **Dwell phase** - Begins when the desired plunge depth has been achieved. The axial force is maintained on the tool during this stabilization phase. The combined effect of the relative speed between the rotating tool and the material with the applied axial force generates heat due to friction at the tool-material interface. The tool is kept in place for a sufficiently long time to reach the temperature required for welding. This phase is also called the ”preheating phase”

3. **Welding phase** - The tool starts to advance and accelerates to the prescribed translational velocity along the weld line. The acceleration may be fast if the dwell phase was sufficiently long and the temperature is high in the weld zone. However, too fast of acceleration can result in high mechanical stresses for both the tool and welding equipment, reducing their useful lifetime. Depending on the design of the tool and the specific process parameters, the FSW tool may be tilted slightly (a few degrees) to improve the quality of the weld.

4. **Retracting phase** - The tool is extracted from the plate leaving behind a characteristic keyhole.

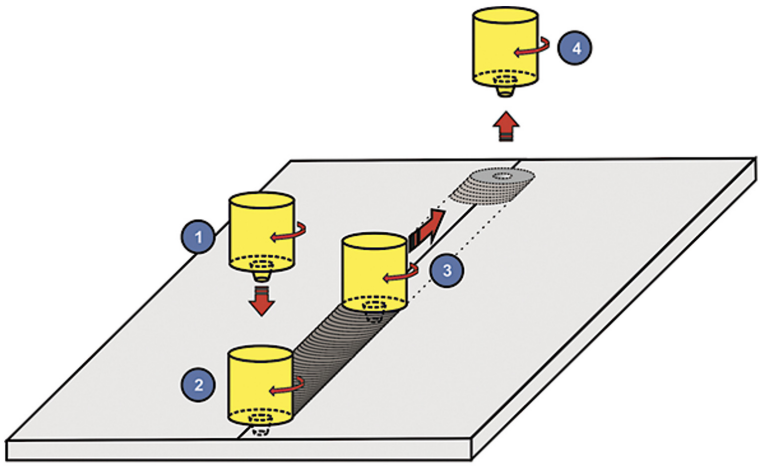


Figure 2.2: Four phases of FSW process. Adapted from [17]

During the FSW process where plastic deformation, as well as high heat, are applied, both materials undergo a complex recrystallisation process leading to a modified metallographic structure in the joint cross-section as can be seen in Figure 2.3.

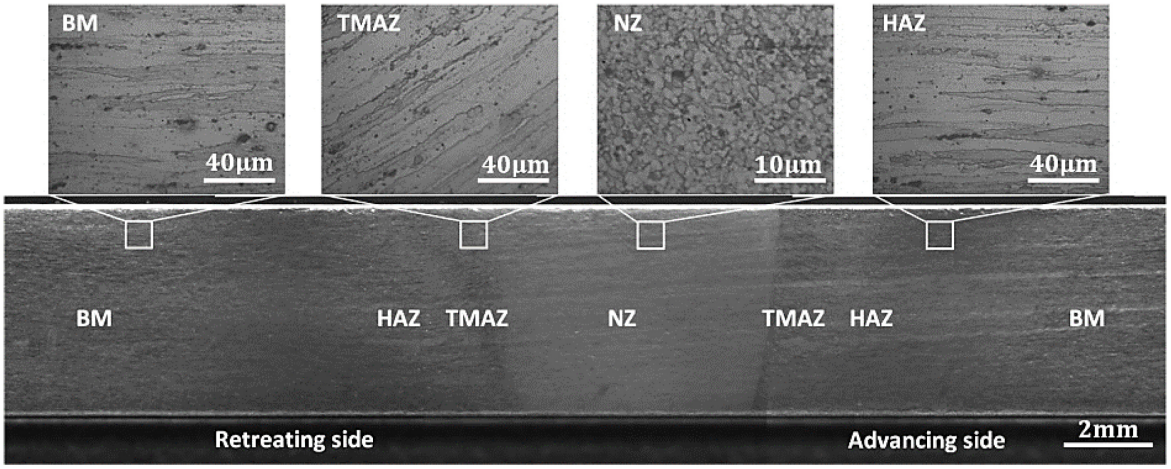


Figure 2.3: Typical microstructure of the joint produced by FSWelding AA7075-T6 in butt joint configuration. Adapted from [18]

Based on variation of the microstructure and/or properties, four microstructural zones are usually defined in friction-stirred materials [19]:

- Base Material (BM) - is the unaffected material, where no deformation has occurred resulting from heat flow.
- Heat Affected Zone (HAZ) - is common to all welding processes. The region suffers from a thermal cycle, causing the softening of the material and modifying its mechanical properties. Even though this zone is not affected by plastic deformation and the temperatures are lower than those found in the TMAZ, it may still have a significant effect if the micro-structure is thermally unstable.
- Thermo-Mechanically Affected Zone (TMAZ) - occurs on either side of the stir zone. This region has been plastically deformed by the tool and the heat flux can significantly alter the material

properties. The material softened and plastic flow is noticeable here by the elongated, deformed, and re-oriented grains. Grain growth and coarsening of strengthening precipitates occur in this region.

- Stir Zone (SZ) - or Weld Nugget (WN), is where the original grain and sub-grain boundaries appear to be replaced with fine, equiaxed recrystallized grains characterized by a smaller nominal dimension of a few micrometres. This zone is shaped based on welding parameters employed - such as rotation speed, traverse speed, and axial force -, and the base material. The pin used is also a defining factor, the larger the pin diameter, the larger the WN and rounder will be the zone shape.

Although the most frequently found configurations in literature are the butt-joints and overlap joints, it is possible to achieve a wide variety of joint geometries by combining these two. Figure 2.4 presents other possible configurations in FSW.

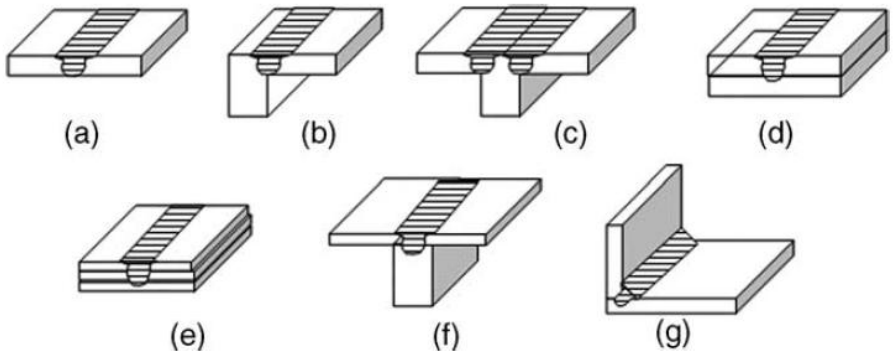


Figure 2.4: Joint configurations for friction stir welding: a) square butt, b) edge butt, c) T butt joint, d) lap joint, e) multiple lap joint, f) T lap joint, and g) fillet joint. Adapted from [20]

According to the literature, it is not unusual for the welded joint to be classified according to its efficiency. The efficiency of a joint, given by Equation 2.1, is the ratio between the Ultimate Tensile Strength (UTS) of the welded joint and the UTS of its base material:

$$Efficiency\ [\%] = \frac{\sigma_{UTS_{FSW}}}{\sigma_{UTS_{BM}}} \cdot 100 \tag{2.1}$$

### 2.1.2 Aerospace Industry and future applications

Weight is one of the greatest challenges to aircraft manufacturers. FSW is studied as a method of permanent joining in special aerospace structures made of aluminium, titanium, magnesium alloys, and high-temperature steels. By joining sub-components used to produce most of the primary structural components in the airframe, such as aluminium alloy stringers to skins for aircraft wings and fuselage structures, will reduce weight through the removal of thousands of rivets, and any overlapping aluminium material resulting in cost savings of up to 30% and weight savings of up to 10% for a typical airframe structure [21]. One leading aircraft manufacturer estimated that it is possible to obtain weight savings of approximately 1 kg/m of FSW [22] while another stated that by replacing riveted splice where usually 3

rows of rivets are required with a typical overlap of about 75 mm, leads to a potential weight saving up to 0.8 kg/m of joint [23].

The maturity of FSW as a technology lead to the appearance of new numerically controlled equipment, tools and control methods, allowing this joining method to be used in the production of spacecraft, military, and civilian aircraft as well as jet engine parts. In the aerospace industry, FSW is used in the manufacture of components from high-strength aluminium alloys, such as large satellite panels and external fuel tanks for rockets, spacecraft, and test prototypes [24].

As an example of real-world engineering problems, Figure 2.5 presents how SpaceX used a circumferential FSW machine in order to join the barrel sections of the Falcon 9 second stage back in 2008 [25]. Eclipse 500, manufactured by Eclipse Aviation in 2002, is another great example of FSW use in the aerospace industry. Not only it was the first aircraft to receive approval from the Federal Aviation Administration (FAA) to employ FSW on most of its airframe by joining stiffeners and frames to the skin panels, they also made 128m of FSW per airframe, replacing approximately 7000 rivets which is equivalent to about 60% of the rivets used in the assembly process [26].

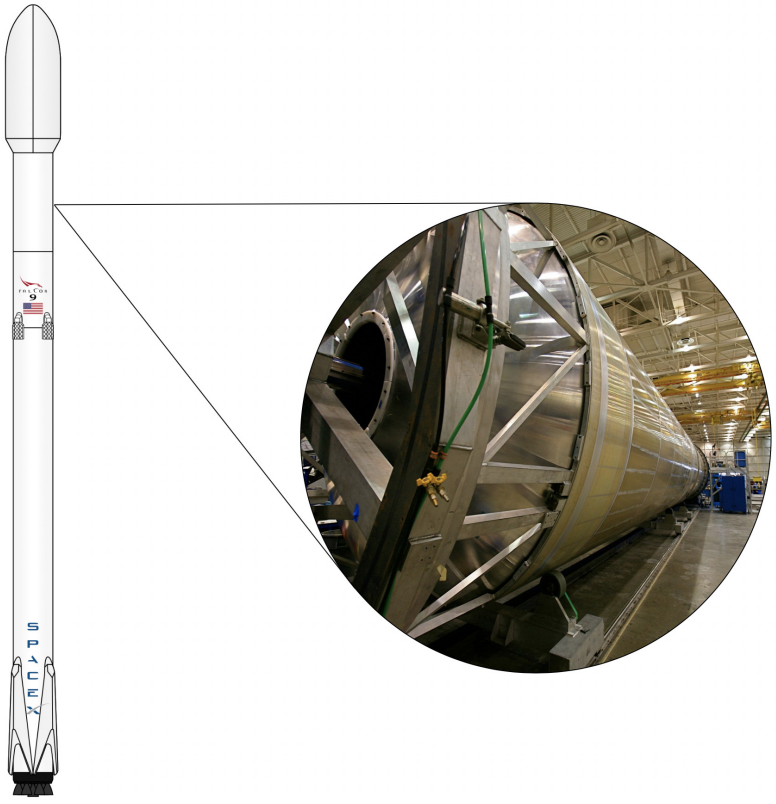


Figure 2.5: Use of FSW on Falcon 9 second stage. Adapted from [25]

At this point in time, beyond the examples presented and a few others omitted, the applications of FSW in the industry are still limited due to a highly regulated certification process.

The aerospace industry with great emphasis on commercial aviation is in constant need of new and lighter aircraft capable to deal with the continual growth of air travellers around the world, expected to double in the next 2 decades according to IATA [27]. Figure 2.6 showcases an ever-growing use of titanium on airplanes produced by the two biggest aircraft manufacturers. With that in mind, FSW gains

even bigger importance in the future of the aerospace industry as there will be a great need in joining dissimilar materials to produce aircraft of the future.

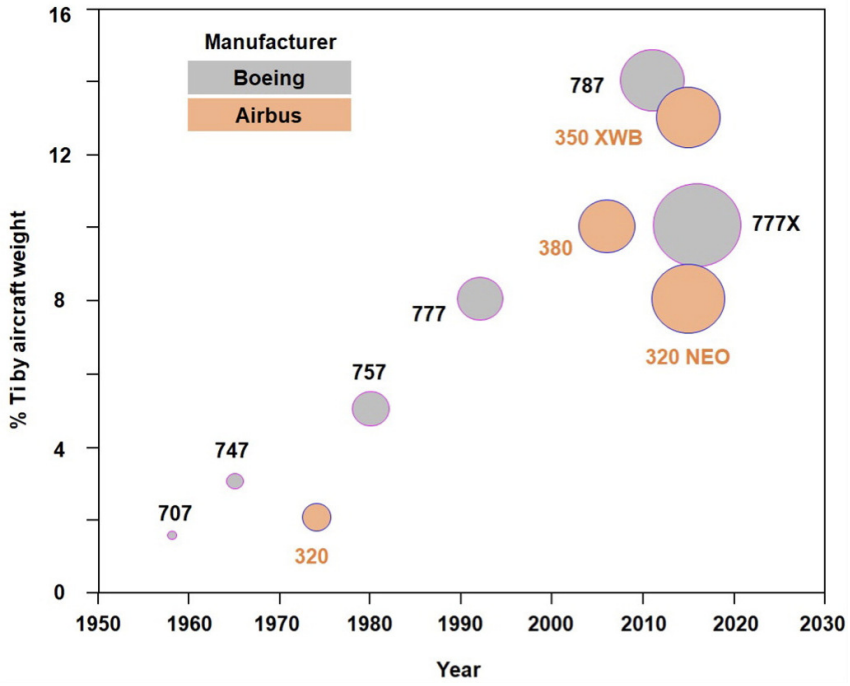


Figure 2.6: Increasing use of Titanium in commercial aircraft. Bubble size denotes the passenger capacity. Adapted from [28]

## 2.2 Linear Elastic Fracture Mechanics

Sudden fracture of structural materials was one of the most common causes of accidents in early aircraft. Materials for early aircraft were selected for maximum strength and minimum weight, and their fracture resistance was not an overriding consideration. Furthermore, the capability of materials to resist cracking and sudden failure was not well understood in the design and construction of these early aircraft [29].

In the aviation industry, de Haviland Comet airliner is one of the most known examples of failures caused by metal fatigue, with three major accidents occurring between 1953 and 1954. Injury patterns in all crashes exhibited that the aerial window mounted to the cabin roof by riveting produced microcracks around the rivet holes. Repeated pressurization of the aircraft cabin accelerated the crack propagation by the effect of metal fatigue. Then the joining section of the aerial window could not withstand the internal pressure of the aircraft cabin and the fuselage exploded catastrophically during flight, soon after take off. It was later proven by the conducted investigation tests that up to 70% of the aircraft's ultimate stress accumulated on the corners of the aircraft's windows [30].

The serious injuries and fatalities during the first decades of powered flight forced engineers to consider fracture as a critical factor in the safe design of aircraft structures, and later, jet engines.

Fracture Mechanics (FM) is a field of research used to predict and diagnose the failure of a part with an existing crack or defect. The presence of a crack in a part magnifies the stress in the vicinity

of the crack and may result in failure prior to that predicted using traditional strength-of-materials methods, namely yield or ultimate strength, depending on the failure criteria established during the project development [31].

Many analytical methods are available to calculate the fracture strength of materials containing cracks, and almost all are based on the principles of Linear Elastic Fracture Mechanics (LEFM). LEFM is a highly simplified, yet sophisticated, theory that deals with sharp cracks in elastic bodies. It can be simply described as the analysis of materials containing one or more cracks that fail by brittle fracture. Originally developed by Griffith [32] in 1921 whose idea was to explain the behaviour of flaws in a specimen, which resulted in a linear relationship between an artificial flaw length $a$ and stress at fracture $\sigma_f$ presented in Equation 2.2

$$\sigma_f \cdot \sqrt{a} \approx C \tag{2.2}$$

where $C$ represents a constant. In 1957, Irwin [33] completed this relation in its essential form through a thermodynamic approach, by taking into account the plastic deformation that occurs in crack front in ductile materials. In the same paper, one of the most important and useful parameters in FM was introduced - the Stress Intensity Factor (SIF), K - that will be explored in more detail later in this Section.

### 2.2.1 Crack-tip geometry

Crack-tip can be defined as an infinitesimally small region at the extreme end of the crack. In the case of the crack being analysed in a 2D environment, the crack-tip is a single point. On the other hand, a 3D analysis transforms a crack-tip in a line [34]. Both situations are also highly dependent on another condition that is whether the crack propagates partially or entirely through-thickness, as shown in Figure 2.7.

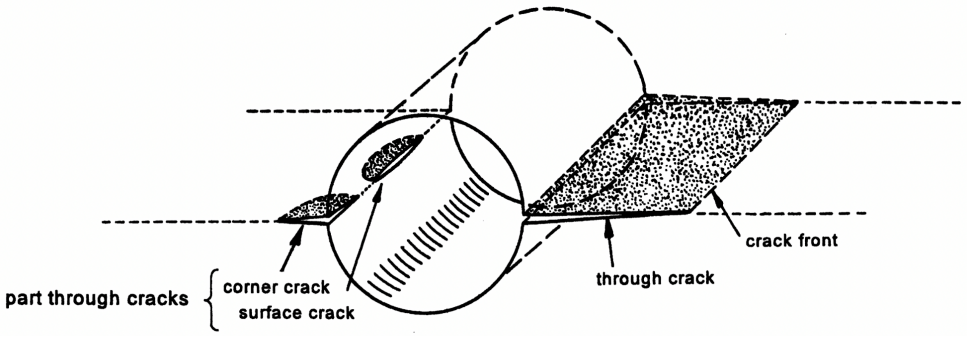


Figure 2.7: Representation of different crack types. Adapted from [35]

Complete through-thickness propagation can be treated as a 2D crack-tip region as in Figure 2.8 (a), and corresponds to a plane strain analysis, while the latter will lead to a more complex 3D crack-tip region, represented in 2.8 (b), where plane strain conditions are used, except for the surface point, where plane stress still applies [32, 33, 35].

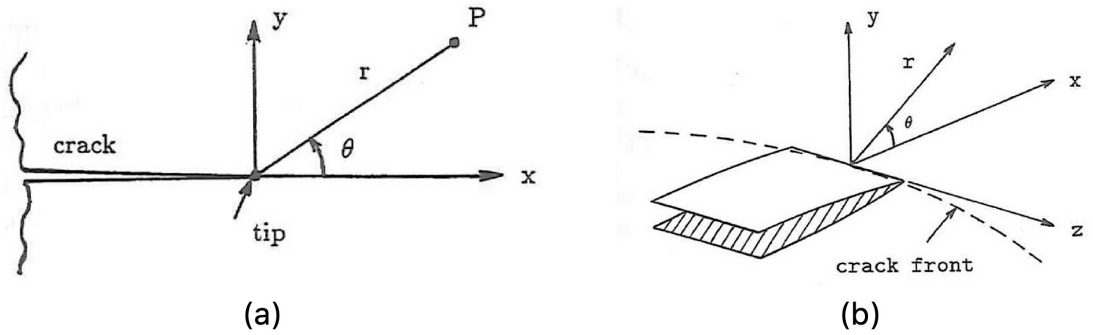


Figure 2.8: Representation of the crack-tip geometry in (a) 2D and (b) 3D environment. Adapted from [34]

Cartesian ($x$,$y$,$z$) and polar ($r$, $\theta$, $z$) reference systems are used to characterize both crack tips, with $z$-axis always tangent to the crack line and $x$-axis laying on the uncracked region.

### 2.2.2 Crack propagation

In FM there are three major mechanisms that enable cracks to propagate as displayed in Figure 2.9.

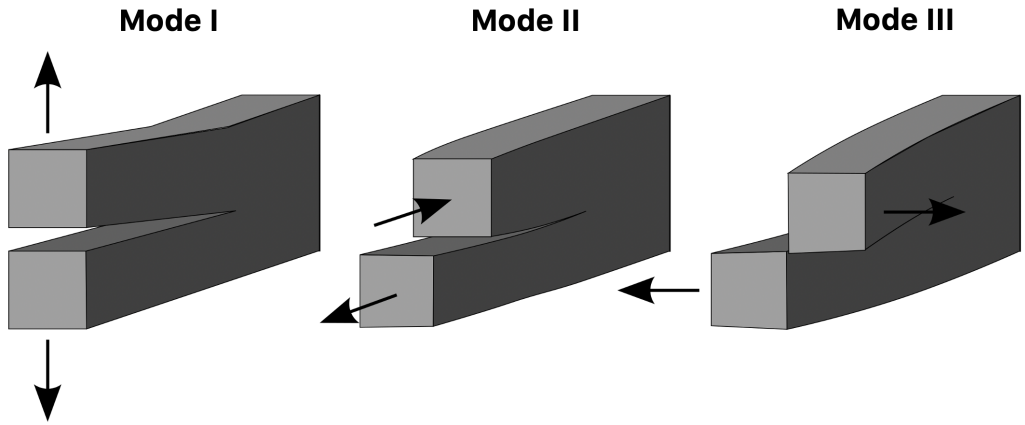


Figure 2.9: Main fracture modes for crack propagation. Adapted from [36]

• **Mode I** or opening mode - the most dominant mode for crack growth where tensile stress is applied normal to the plane of the crack. It is the only mode that allows for the calculation of Fracture Toughness, $K_{Ic}$;

• **Mode II** or sliding mode - shear stress acting parallel to the plane of the crack and perpendicular to the crack front, *i.e.*, in-plane;

• **Mode III** or tearing mode - shear stress acting parallel to the plane of the crack and parallel to the crack front, *i.e.*, out of plane.

A combination of these crack propagation modes can also happen. In this case, the fracture mechanism is called a mixed-mode fracture and it is as important a research subject as other modes. The reason behind it is that many service failures occur from the growth of cracks subjected to mixed mode loadings [37].

### 2.2.3 Stress Intensity Factor

SIF is the main parameter used to describe a LEFM crack growth and can be defined as a measure of the elastic energy change due to fracture growth computed at each fracture tip node [38]. From the physical standpoint, it is a correlation between the stress conditions in the plate and the actual crack dimensions.

According to Griffith criterion, a small crack of length $a$ can only grow to a new length $a + \delta a$, in a plate thickness $t$, *if the work done by the applied loads is greater than or equal to the change of elastic energy plus the energy absorbed at the crack tip, then fast fracture will occur* [34]. This exact statement can be translated into the following mathematical expression:

$$\delta W \geq \delta U^{el} + G_c \cdot t \cdot \delta a \tag{2.3}$$

where $\delta W$ is the work done to create a crack extension, $\delta U^{el}$ is the change in elastic strain energy and $G_c$ is the critical energy release rate that indicates how easily a material can crack - the greater this value is, the harder it is for material to crack.

The Equation 2.3 can be rewritten in terms of critical energy release rate, $G_c$, and a critical stress $\sigma_c$, expressing the failure in an infinite plate with central crack:

$$G_c = \frac{\sigma_c^2 \cdot \pi \cdot a}{E} \tag{2.4}$$

which can be further refined into a more familiar expression for Fracture Toughness, $K_{Ic}$:

$$\sigma_c \cdot \sqrt{\pi \cdot a} = \sqrt{G_c \cdot E} = K_{Ic} \tag{2.5}$$

Extending the concept, SIF, is given by

$$K = \sigma \cdot \sqrt{\pi \cdot a} \tag{2.6}$$

with units usually in MPa$\cdot\sqrt{\text{m}}$.

Irwin [33], on the other hand, proposed a fundamental definition 2.7 by defining the energy release rate $G$,

$$G = -\frac{dP}{da} \tag{2.7}$$

which is the rate of change in potential energy with the crack area [39].

Equations 2.4 and 2.7 are considered to be a cornerstone of LEFM analysis in its general form. The change in potential energy is considered to act on closing a small segment of crack length, equating this quantity to the work required to close the segment without any external work variation [40]. The following equations are valid for a general crack mode, for plane stress and plane strain, respectively:

$$G = \frac{1}{E} \cdot (K_I^2 + K_{II}^2) + \frac{(1+\nu)}{E} \cdot K_{III}^2 \tag{2.8}$$

$$G = \frac{(1-\nu^2)}{E} \cdot (K_I^2 + K_{II}^2) + \frac{(1+\nu)}{E} \cdot K_{III}^2 \tag{2.9}$$

where $K_I$, $K_{II}$, and $K_{III}$ represent SIF of the respective crack growth mode, $E$ is Young's modulus of the material, and $\nu$ is the Poisson's ratio of the material.

## 2.3 Fatigue Crack Growth

As already mentioned throughout this master's thesis, fatigue is responsible for most structural failures in engineering, with an estimation of 90% frequency when it comes to metal failure [41]. In fatigue, the failure occurs when the stress is lower than the strength, but it is applied repeatedly over a long period of time by the effect of the cyclic loadings.

The process of fatigue failure is physically and macroscopically described by crack-growth behaviour.

A glimpse at the Figure 2.10 depicts three distinct stages in the fatigue crack-growth mechanism [41, 42]:

1. **Crack initiation** — Fatigue cracks frequently initiate at a free surface and near a stress riser, *e.g.*, sharp notches, corners. This stage is characterized by a slow crack growth process, usually in the order of $\frac{da}{dN} \leq 10^{-9}$ m/cycle, which is mostly related to localized discontinuities in the metal's crystal structure. The generation and movement of these discontinuities go by the name of strain hardening, a phenomenon that actually strengthens the metal through plastic deformation. As the metal becomes work hardened, it loses its ability to plastically deform in the localized area where cyclic stresses are evident. Once the metal reaches its plastic deformation limit, the discontinuity becomes a small crack.

2. **Crack propagation** — Once a crack has developed, continued cyclical stresses promote a continuous crack's growth. This fatigue process is referred to as the power growth behavior usually characterized by the Paris law that will be dealt with later in this section. One particularity of the surface characteristics is the formation of beach marks and striations in some metallic materials. They indicate a successive advance of one stress cycle and can only be observed with the Scanning Electron Microscope (SEM).

3. **Fracture** — The final failure event typically is an abrupt one and it can be ductile or brittle, depending on the material, thickness, temperature, and the applied stress. The fatigue-induced fracture surfaces of a broken component are typically smooth and show no evidence of plastic deformation.

The curve is limited in the horizontal axis by two values, $\Delta K_{th}$ and $K_{Ic}$. Below $\Delta K_{th}$, the loads are too low and crack will not develop. Above $K_{Ic}$, the crack has grown to certain dimensions where it is considered to have material failure by fatigue.

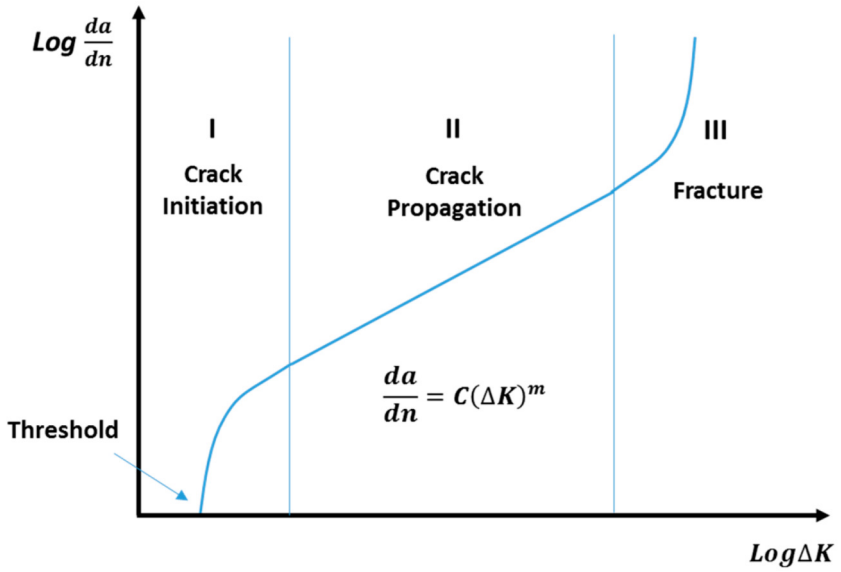


Figure 2.10: Typical crack-growth curve characterized by three different stages. Adapted from [43]

### 2.3.1 Fatigue loading

Fatigue exists only when the stress applied on a certain component is dynamic, *i.e.*, when it fluctuates throughout time. Mechanical components can be subjected to two types of load history: Constant Amplitude (CA) loading and Variable Amplitude (VA) loading.

Although almost all engineering components are subjected to a variable amplitude loading, as in Figure 2.11, the first step in understanding the fatigue properties of materials is determining their response under simple cyclic loading conditions that do not involve random stress cycles.

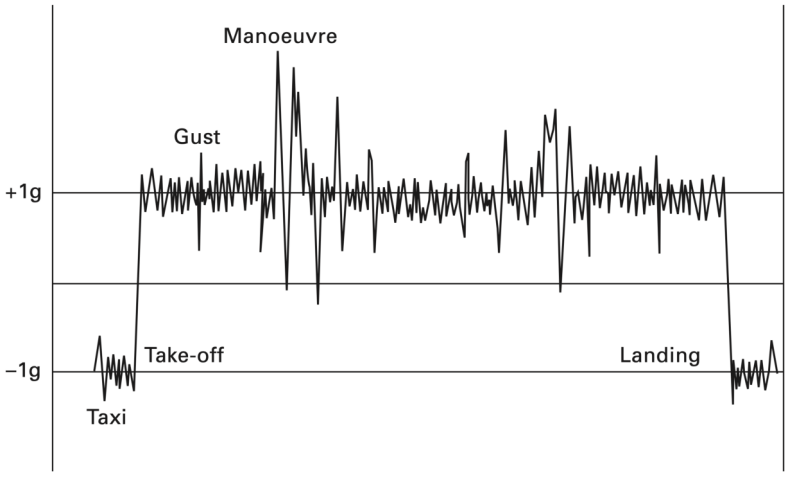


Figure 2.11: Typical fatigue stress profile of an aircraft wing during one complete flight cycle. Adapted from [44]

In CA stress curves, represented in Figure 2.12, it is possible to identify several key parameters that can affect the fatigue properties of materials. $\sigma_{max}$ and $\sigma_{min}$ are maximum and minimum stress values, respectively, and are measured with respect to the null stress condition. The stress range $\sigma_r$ is defined

by the Equation 2.10

$$\sigma_r = \sigma_{max} - \sigma_{min} \tag{2.10}$$

Stress amplitude, $\sigma_a$, is given by the half of the $\sigma_r$

$$\sigma_a = \frac{\sigma_{max} - \sigma_{min}}{2} = \frac{\sigma_r}{2} \tag{2.11}$$

and the mean stress, $\sigma_m$ is the average of the maximum and minimum stresses, $\sigma_{max}$ and $\sigma_{min}$

$$\sigma_m = \frac{\sigma_{max} + \sigma_{min}}{2} \tag{2.12}$$

Another important value in fatigue is the stress ratio, $R$. Having $R > 0$ usually affects the fatigue life of a component in a negative way. It represents the relative magnitude between the minimum and maximum stresses in each cycle and it goes by the following expression

$$R = \frac{\sigma_{min}}{\sigma_{max}} \tag{2.13}$$

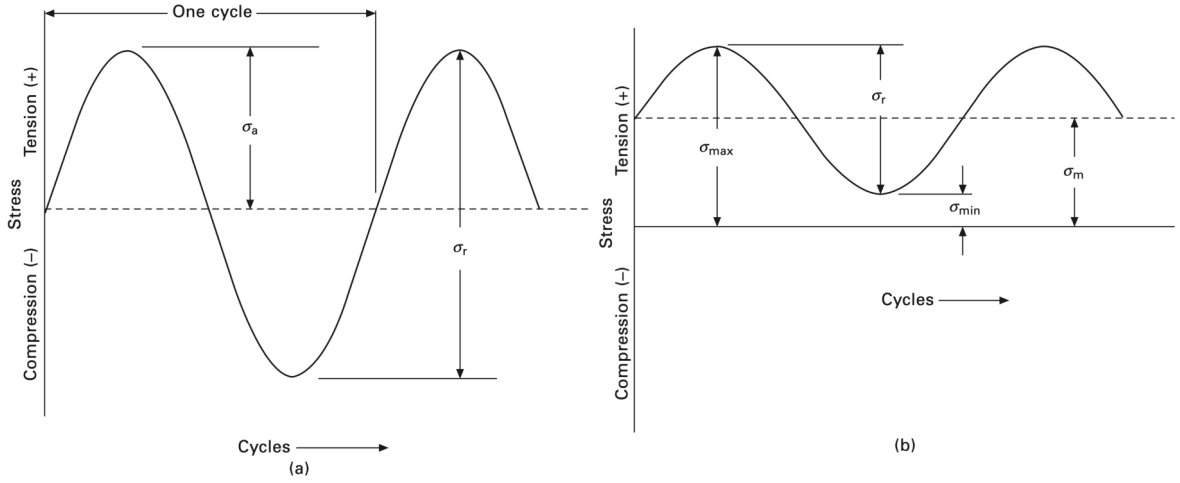


Figure 2.12: Fatigue stress profiles for (a) fully reversed and (b) repeated stress cycling. Adapted from [44]

### 2.3.2 Paris Law

Most commonly known as Paris law, it was one of the first crack propagation relations, proposed by Paris and Erdogan [45] in 1963, to correctly quantify the rate of crack growth da/dN within a certain range of $\Delta K$. From the experimental data available plotted on a $\log$-$\log$ scale, they observed that, not only the crack growth was limited by two vertical asymptotes given by $\Delta K_{th}$ and $K_{Ic}$, values that have already been explored at the beginning of this section, but that the same plots presented a straight line which corresponds to the second stage of crack growth. This implies that

$$\log\left(\frac{da}{dN}\right) = m \cdot \log(\Delta K) + \log C \tag{2.14}$$

and without $\log$, the expression 2.14 takes a more familiar form in the equation 2.15

$$\frac{da}{dN} = C \cdot \Delta K^m \tag{2.15}$$

where $C$ and $m$ are materials constants.

For the first time, it became possible to make a correct quantitative prediction of residual life for a crack of a certain size by simply finding limits on the integration in terms of crack size. It can be done by simply replacing $K_{Ic}$ in the modified Equation 2.6 that includes the shape factor, $Y$, to find the critical crack size $a_f$.

Separation of the variables $a$ and $N$ and substitution for the range of stress intensity by the equivalent equation in terms of stress and crack size gives

$$\frac{da}{dN} = C \cdot (Y \cdot \Delta\sigma \cdot \sqrt{\pi \cdot a})^m \tag{2.16}$$

presenting the final solution in an integral form

$$\int_0^{N_f} dN = \int_{a_i}^{a_f} \frac{da}{C \cdot Y^m \cdot \Delta\sigma^m \cdot (\pi \cdot a)^{\frac{m}{2}}} \tag{2.17}$$

Expression 2.17 presents an approximation for fatigue life expectancy for the most basic geometry. More complex geometries imply having a more complex definition of $\Delta K$ and with it a more sophisticated way of determining fatigue life.

### 2.3.3 Fatigue in FSWed aluminium alloys

In light of this master's thesis main investigation subjects being the crack propagation in FSWed 5xxx series aluminium alloy, it is of great significance to make a good literature overview of the recent advances in the field.

From this perspective, one of the first papers that *pop-up* on the topic was published in late 2018 by Hongjun Li et al. [5]. They made an exhaustive literature review of dozens of papers and summed up that the fatigue performance of FSWed joints can be affected mainly by welding process parameters, test environment, stress ratio, residual stress, and weld defect. They also found out that fatigue crack initiation generally started at the surface of the weld, located in between the TMAZ and the HAZ. At last, laser peening was recommended as a post-weld treatment, as it can greatly decrease FCP rate and improve material fatigue life.

Das et al. [9] also reviewed the literature on process parameters effect on FCP rate in several FSW metal alloys, among which aluminium. From the majority of conclusions drawn, tool rotational speed and welding speed presented the largest influence on FCP as they are directly connected to the microstructure of the weld line.

Zadeh et al. [6] studied FCP in different FSW joint zones of AA2024, using a combination of Paris and Forman-Newman-de Koning models where they concluded that this method can lead to a higher

level of accuracy of crack growth behaviour prediction.

Al 7xxx series alloy has been extensively utilized in the aerospace industry, mostly aircraft structural parts. Sivaraj et al. [7] investigated the FCP behaviour of 12 mm thick AA7075-T651 plates joined by FSW using a center cracked tensile (CCT) specimen. From tensile testing, they understood that the FCP resistance becomes greater as the tensile strength or the yield strength obtained from the static tensile test becomes greater because the plastic strain per load cycle is reduced. Also, reduced elongation of the FSW joint also imparts lower resistance to FCP.

Labeas and Peppa [8] explored FCP in two 2xxx series Al alloys, AA2198-T3 and AA2139-T3, in several specimen thickness, frequencies, and loads, with crack growing parallel to the FSW joint and towards it, respectively for each alloy. In the case of a crack propagating parallel to the weld line and inside the weld centre, a marginal decrease of the FSW fatigue crack growth behavior was observed. In the case of a crack propagating towards a longitudinal weld, the AA2139-T3 welded material exhibited FCP behaviour similar to that of the parent material. In the end, they concluded that the weld interface between WN and TMAZ was the most susceptible area of the weld for crack initiation and fast crack propagation.

Zhou et al. [10] studied the influence of the KB on the mechanical properties and fracture behaviour of 6 mm AA5083-H112 FSW butt welds. They found out that the fatigue life of the welds was inversely proportional to the size of KB in the joints, and the last one depends linearly on the amount of heat generated during FSW. Another interesting finding was the strong correlation of UTS and fatigue life with the fracture types obtained in tensile testing. Shear fracture resulted in higher tensile UTS and longer fatigue life, while poor strength and fatigue properties were associated with the welds showing a fracture path along the kissing bond.

Zhang et al. [11] made profound research of AA6061-T6 FSWed joint, including FCP. Beyond all the conclusions drawn about microstructure and mechanical properties of the joint, they also tried to study the FCP of different FSW zones. What they found was an unstable crack growth in the WN for certain values of a and $\Delta$K. Base material showed the best stability in FCP followed by HAZ. Compressive residual stresses were also found in the SZ.

In 2019, Dong et al. [12] used surface mechanical rolling treatment (SMRT) in 25 mm thick AA7075-T651 FSWed joints in order to produce a near-polished surface by eliminating the microgrooves. During uniaxial fatigue testing, they were able to find out that SMRT increased dramatically fatigue life in the joints, with two orders of magnitude extension, while exhibiting failure mode transitions from the surface to interior.

Ilman et al. [13] applied transient thermal tensioning (TTT) to AA5083-H116 FSWed plates in an attempt to improve the fatigue life of the joints. Results showed that TTT treatments modify the distribution of residual stresses and cause microstructural changes, two factors that strongly influence fatigue performance of the weld joints and mechanisms of the fatigue crack growth.

In the previous paragraphs, a tiny example of published studies about this topic was presented. Although there is many more literature available, it is not possible to include every single study in this document as they come in all different kinds and shapes. Nevertheless, according to [5], the amount of

data available for each and every alloy is still scarce, and much more investigation can be done.

## 2.4 XFEM applied to FCP

The genesis of the Finite Element (FE) method came from the need to solve complex elasticity and structural analysis problems in civil and aerospace engineering. Although it is not easy to trace back an exact date to the invention of this method, one of the first works was published by Clough et al. [46], back in 1956. Many more were published in the following decades with the method gaining its real impetus between the 1960s and 1970s, a time frame that also coincided with the National Aeronautics and Space Administration (NASA) developing a well known structural analysis solver tool named NASTRAN. Nowadays, and with the tools available, the FE method can be applied to several engineering fields among which structural analysis, heat transfer, fluid flow, mass transport, and electromagnetic potential.

The eXtended Finite Element Method (XFEM) resulted from the difficulty to model discontinuities and fractures using conventional FE analysis combined with FM laws [47–49], as it requires a constant remeshing around the crack in order to capture the singular asymptotic field accurately. First proposed by Belytschko and Black [50] and Duarte et al. [51], it is based on the concept of partition of unity, introduced by Melenk and Babuška [52] in 1996.

XFEM is used in the approximation of discontinuities and singularities, like the displacement near a crack, by enriching its degrees of freedom. The key elements of XFEM are two local enrichment functions - an asymptotic crack tip function $F_\alpha(x)$ responsible for the singularity around the crack tip, combined with a discontinuity function $H(x)$, also know as the *jump* function, that represents the gap between the crack surfaces [53]. By enriching the conventional finite element approximation, the displacement field is described as [54]

$$u = \sum_{j=1}^{n} N_j(x) \cdot \left[ u_j + H(x) \cdot a_j + \sum_{\alpha=1}^{n} F_\alpha(x) \cdot {b_j}^\alpha \right] \tag{2.18}$$

where $N_j(x)$ is the standard FEM shape function of the node $j$, $u_j$ is the classical nodal displacement, $H(x)$ is the Hevyside function represented in Equation 2.19, $a_j$ is the nodal enriched DOF, $F_\alpha(x)$ is the enrichment function, also represented in Equation 2.20, $b_j$ stands for DOF associated with $F_\alpha(x)$, and $n$ denotes the number of enrichment functions for node $j$. Translating the Equation 2.18 in simpler terms: the first part is applicable to all the nodes in the model, the second part is applied to the set of nodes enriched by the discontinuous function, *i.e.*, crack interior, while the third part is a set of nodes with tip enrichment functions, *i.e.*, crack tip.

Graphical representation of the discontinuous *jump* function can be observed in Figure 2.13 (a) and is defined as [55]

$$H(x) = \begin{cases} 1, & \textit{if } (x - x^*) \cdot n \geq 0 \\ -1, & \textit{otherwise} \end{cases} \tag{2.19}$$

where $x$ is an arbitrary point near the crack face, $x^*$ is the closest point to $x$ located on the crack face

and $n$ is the outward unit vector normal to the crack at $x^*$.

As for the third term in Equation 2.18, it shows the crack tip function in an isotropic material and is given by [54]

$$F_\alpha(x) = \left[\sqrt{r}\cdot\sin\frac{\theta}{2}, \sqrt{r}\cdot\cos\frac{\theta}{2}, \sqrt{r}\cdot\sin\theta\cdot\sin\frac{\theta}{2}, \sqrt{r}\cdot\cos\theta\cdot\cos\frac{\theta}{2}\right] \tag{2.20}$$

where $r$ and $\theta$ are variables of the polar coordinate system in the local crack tip coordinate system.

Figure 2.13 (b) is represented an arbitrary crack in a 2D enriched mesh where the encircled nodes are enriched with the Heavyside function and the nodes highlighted by a square have been enriched with both enrichment functions, responsible for capturing the crack-tip singularity.

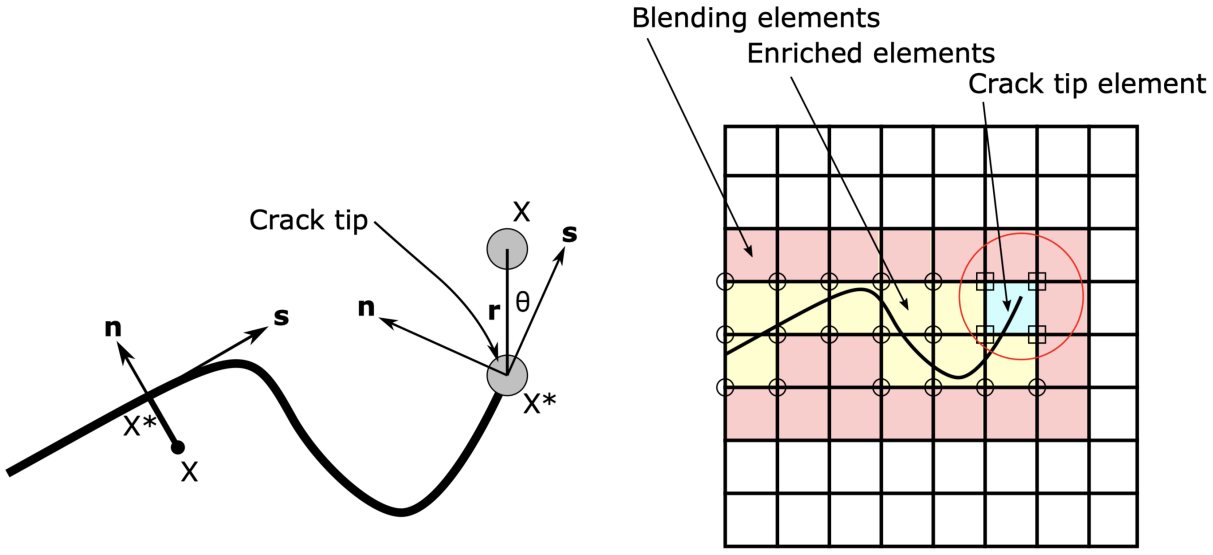


(a) *Jump* / Heavyside function [55]

(b) Arbitrary crack in 2D enriched mesh [55]

Figure 2.13: Graphical representation of crack growth computation using XFEM

With the XFEM-based formulation, it became possible to simulate crack propagation in a wide range of commercially available FE software, among which Abaqus. In recent years, several studies have been published where XFEM was used to study crack propagation under different conditions. For instance, Solob et al. [56] used XFEM analysis to evaluate FCP in damaged wing-fuselage attachment lug. Nikfama et al. [57] performed an experimental FCP in steel welded T-joints and later compared it with XFEM modelling of high cycle fatigue crack growth, with the obtained being results reasonably comparable. They concluded that the XFEM results showed to be conservative in higher cycle fatigue tests and mean errors in the XFEM predictions for the fatigue life ranged from -20.7% to +0.9%. Kumar et al. [58] studied mixed-mode creep crack growth in an aero-engine turbine disc using XFEM. In 2016, Wang et al. [59] performed an XFEM based uncertainty study on crack growth in welded joints with defects, where the applied method proved to be capable of studying the uncertainties induced by random defects and vehicle loads in the early stage of FCP. Bergara et al. [60] showed the capabilities of the XFEM-based LEFM approach, in Abaqus, by simulating FCP on a four-point bending specimen and comparing the obtained results with the experimental part of the investigation. They confirmed that both the shape of the crack and the number of cycles obtained in the numerical simulations have been

very similar to those obtained in the experimental cases.

In Abaqus, FCP can be achieved with a direct cyclic approach, using low cycle fatigue criteria in a combination with a modified Paris law [54]. Modified because all the fracture criteria must be given based on an energy release rate formulation instead of the most common SIF notation 2.15. According to [54], the delamination growth rate, $\frac{da}{dN}$ is given by

$$\frac{da}{dN} = c_3 \cdot \Delta G^{c_4} \tag{2.21}$$

where $\Delta G$ is the fracture energy release rate. $c_3$ and $c_4$ are Abaqus input parameters related to material constants, $C$ and $m$, and can be calculated using expressions 2.24 and 2.25, respectively.

In order to determine the above-mentioned parameters, $\Delta G$ must be defined in its usual formulation [61], in terms of $\Delta K$ and $E'$, as follows

$$\Delta G = \frac{\Delta K^2}{E'} \tag{2.22}$$

with

$$\begin{cases} E' = E, & \textit{in plane stress} \\ E' = \frac{E}{1-\nu^2}, & \textit{in plane strain} \end{cases} \tag{2.23}$$

With this established, $c_3$ and $c_4$ are defined by

$$c_3 = C \cdot {E'}^{c4} \tag{2.24}$$

$$c_4 = \frac{m}{2} \tag{2.25}$$

All the fracture criteria must be input into the model using Abaqus keywords. In the case of FCP simulation with the low-cycle fatigue criterion using a direct cyclic approach, they have the following configuration:

*FRACTURE CRITERION, TYPE=FATIGUE, MIXED MODE BEHAVIOR=POWER

c1, c2, c3, c4, r1, r2, $G_{Ic}$, $G_{IIc}$,

$G_{IIIc}$, $a_m$, $a_n$, $a_o$

Despite the fact that there is a growing number of studies of FCP using XFEM is being published, only a small amount of them explores what is being investigated in this master's thesis.

## 2.5 Final remarks for Chapter 2

This chapter presented an overview of the state-of-the-art that included topics such as FSW, LEFM, FCP, and XFEM applied to FCP.

In the beginning, FSW was introduced as a technique of the future when it comes to joining materials considered hard to join using conventional fusion techniques. Its main principles and intricate challenges

were presented, followed by some real-world examples where this technique is already being applied.

LEFM was the next in line, where basic concepts of cracks and their propagation were presented combined with the historic origin of the most important parameter in FM, the SIF.

Fatigue was presented as the primary cause for failure in the majority of engineering structures. Split into four parts, three characteristic stages of FCP were explained in the first, fatigue loading and Paris law followed the trend, and the current developments in FCP in FSWed alluminium alloys closed this section.

At last, theoretical concepts behind XFEM-based analysis were overviewed with several recent successful examples of its application presented. The application of FCP using a direct cyclic approach with low-cycle fatigue criteria concluded the background chapter of this master's thesis.

# Chapter 3

# Methodology

The purpose of the current chapter is to present a detailed description of all the experimental parameters and procedures, as well as machines used to characterize the material under study, develop the experimental and numerical analysis. The present master's thesis is based on the comparison of the results obtained by two analysis, which will be discussed and from where conclusions will be drawn.

## 3.1 Material Characterization

An aluminum alloy is a chemical composition where other elements are added to pure aluminum in order to enhance its properties, primarily to increase its strength while maintaining its lightweight characteristics. These other elements include iron, silicon, copper, magnesium, manganese, and zinc at levels that combined may make up as much as 15% of the alloy by weight. Alloys are assigned a four-digit number, in which the first digit identifies a general class or series, characterized by its main alloying elements and are split into three types: commercially pure, heat-treatable, and non heat-treatable [62].

### 3.1.1 Material properties and specimen preparation

Aluminium 5xxx series, also known as an Al-Mg alloy, is a non heat-treated alloy type strengthened through cold-working. In particular, AA5083 has attracted a lot of attention because of its exceptional performance in extreme conditions as it revealed to be highly resistant to attack by both, seawater and industrial chemical environments, and retains very good strength after welding. AA5083-H111 has also been confirmed to have exceptional corrosion resistance in deep water environment [63] and is the material under investigation in this Master Thesis. Mechanical properties and chemical composition of this alloy are shown in Tables 3.1 and 3.2 , respectively.

Table 3.1: Mechanical properties of 5083-H111 aluminium alloy. Adapted from [64]

| **Parameter** | **E (GPa)** | $\sigma_y$ **(MPa)** | $\sigma_{UTS}$ **(MPa)** | **Elong. (%)** | $\nu$ |
|---|---|---|---|---|---|
| **Value** | 70.3 | 161 | 302 | 20 | 0.33 |

Table 3.2: Chemical composition of 5083-H111 aluminium alloy. Adapted from [64]

| **Element** | **Al** | **Mg** | **Mn** | **Fe** | **Cr** |
|---|---|---|---|---|---|
| **Weight (%)** | bal. | 5.26 | 1.02 | 0.19 | 0.15 |

Two 300 x 100 mm sheets with a thickness of 5 mm have been previously FSWed in butt configuration using an *ESAB Legio FSW 3UL* numeric control equipment. The tool employed in the production had a 16 mm wide shoulder with threaded tapered pin profile on its end and it rotated in the clockwise direction. Welding parameters are presented in Table 3.3.

Table 3.3: FSW parameters used to join two 300 x 100 mm AA5083-H111 sheets with 5 mm thickness. Adapted from [64]

| **Parameter** | **Axial force (kgf)** | **Rotation sp. (rpm)** | **Traverse sp. (mm/min)** | **Plunge (mm)** | **Tilt (°)** |
|---|---|---|---|---|---|
| **Value** | 550 | 1000 | 10 | 4.3 | 0 |

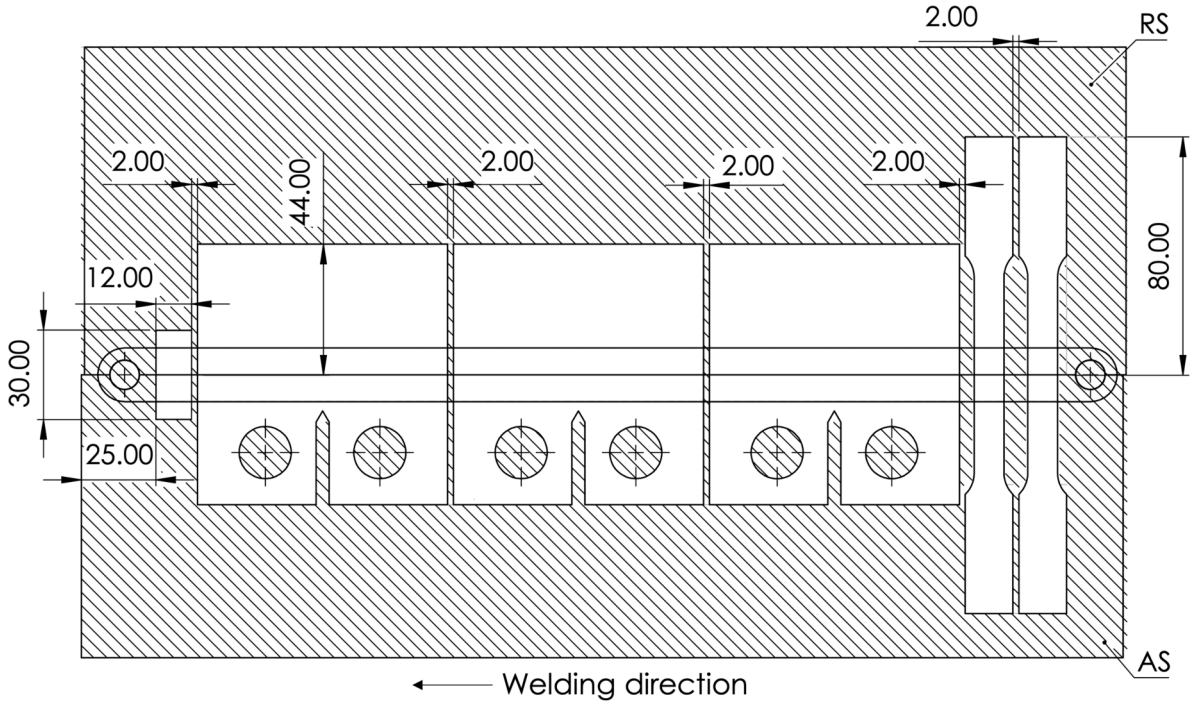


Figure 3.1: Arrangement of AA5083-H111 FSWed sheets used for fatigue, tensile and metalographic specimen manufacture. All dimensions are indicated in mm

As for the specimen preparation, a total of 6 of them were produced - 3 CT specimens for FCP testing, 2 tensile specimens for Digital Image Correlation (DIC) analysis, and 1 metallographic sample to be used in micro-hardness and microstructure observation - using wire Electro Discharge Machining (EDM) [65]. All of the specimens and their respective drawings were made according to the American Society for Testing and Materials (ASTM) E647 [66] and E8 [67] standards, using *Solidworks 3D* CAD software with Figure 3.1 showcasing the final drawing sent for manufacturing. CT specimen development is explained in more detail in Section 3.2.

### 3.1.2 Tensile tests

Tensile tests were conducted to determine *quasi-static* mechanical properties of the joint as well as extract stress-strain curves from various characteristic weld zones, namely SZ and TMAZ, using 2D DIC. Specimen, illustrated in Figure 3.2 with dimensions in mm, have been manufactured according to ASTM E8 [67] standard and tests executed on *INSTRON 3369* universal testing system with 50 kN of maximum load capacity, with the applied crosshead speed of 1 mm/min.

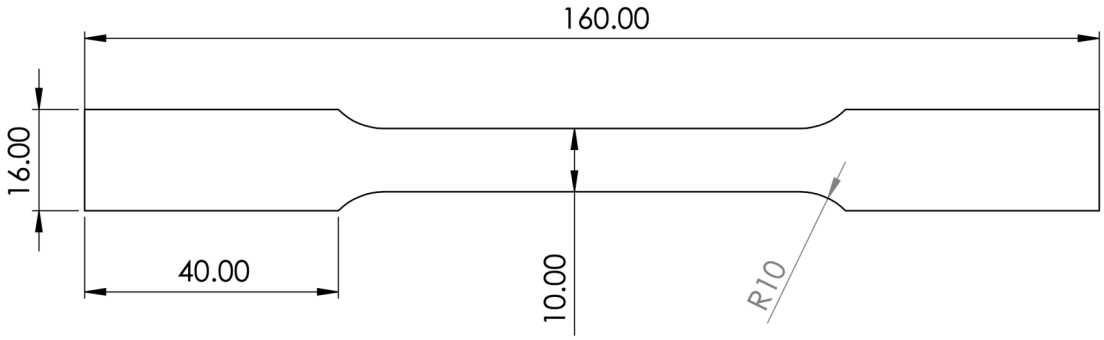


Figure 3.2: Drawing of the tensile specimen used for testing. All dimensions are in mm

DIC is a non-contact optical technique that provides a full field strain measurement. It measures the surface displacement and strains over the entire area of interest using optical photogrammetry techniques, *i.e.*, by tracking the position of multiple surface points in two consecutive images by using a correlation algorithm [68].

Both specimens were spray-painted a stochastic pattern on the surface where the weld line was located. For image acquisition, one *Allied Vision Stingray F504B* high-performance camera paired with *Hedler DX15* lighting system was required. The image capture speed was set to 3 frames per second.

Post-processing was done in *Correlated Solutions VIC-2D 2009* software. Figure 3.3 shows two frames of Specimen 1 during testing - an undeformed one corresponding to the first frame in the beginning of the test and a deformed one, corresponding to the exact frame prior to breaking. Colors represent the extension in $y$-direction across the entire field of the specimen.

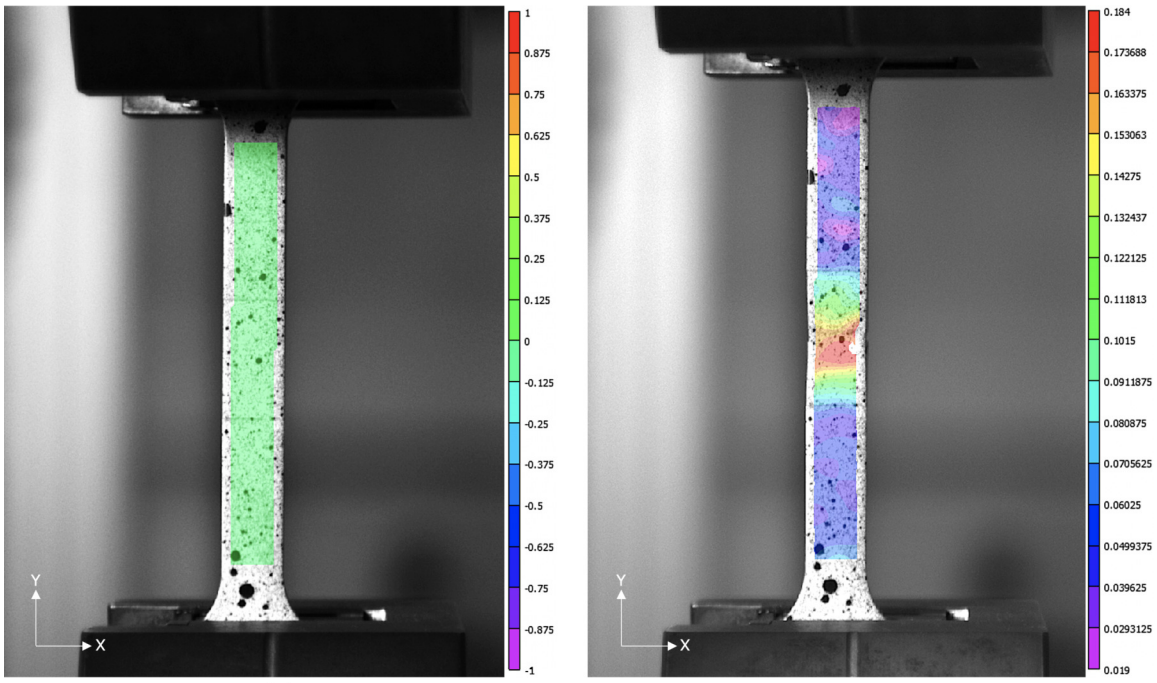


Figure 3.3: Post-processing of the Specimen 1 tensile test with (a) representing the first frame in the beginning of the test and (b) representing the frame immediately before rupture

### 3.1.3 Roughness measurements

Roughness can be defined as a measurement of the small-scale variations in the height of a physical surface. It consists of surface irregularities which result from the various machining process where FSW is one such process. In order to determine the linear surface roughness of the welded joint area, prior to any machining or polishing of the specimen, a *Filmetrics Profilm 3D* optical profilometer, with a 20x objective, was used to analyze regions of interest using White Light Interferometry (WLI) [69]. The raw data files were post-processed with the corespondent computer software and its online counterpart.

The strategy behind roughness measurements consisted of taking 5 independent images, with a surface scanned area of 1.0 x 0.85 $mm^2$, along the weld line from three characteristic FSW zones - TMAZ+HAZ-AS, SZ, and TMAZ+HAZ-RS - making a total of fifteen scans, as it can be observed in Figure 3.4 (a) (the red squares indicate the scan areas). Moreover, in Figure 3.4 (b), (c), and (d), 3 examples of the morphology of different regions can be observed as 3D topographic images.

Linear roughness values were measured 6 times in each of 15 scans - 3 measurements along *x*-direction and another 3 measurements along *y*-direction - using a tool in *Profilm 3D* software named *Line Roughness* which calculates an arithmetic mean deviation linear roughness ($R_a$) along a defined path.

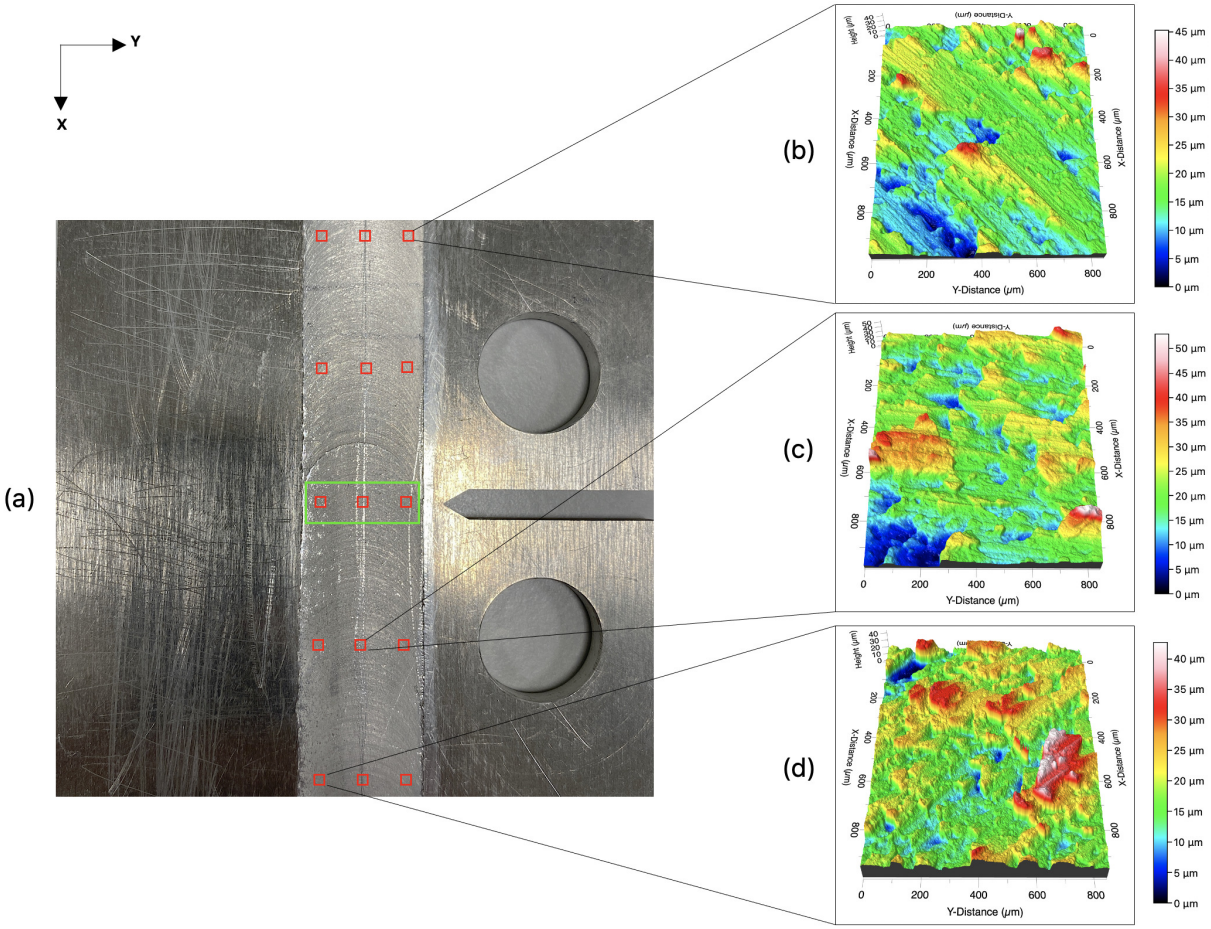


Figure 3.4: (a) Photograph of the analyzed CT specimen, where the areas observed through optical profilometry are represented by red squares. Green rectangle highlights the area corresponding to the 3D image shown by the Figure 4.1. (b), (c) and (d), are examples of the three-dimensional characteristic surface morphology of TMAZ+HAZ on AS, SZ and TMAZ+HAZ on RS, respectively.

Additionally, it was decided to take an image of a bigger area across the entire joint width, around the region where the crack shall grow during fatigue testing (the area was evidenced in Figure 3.4 by the green rectangle). In order to form a topographic image with an approximate area of 17 x 5 $mm^2$, a total of 189 images of 1 x 0.85 $mm^2$, with a 20% of overlap, were obtained and stitched together, with the results presented in Chapter 4 in Figure 4.1.

### 3.1.4 Microstructure analysis

During FSW, several changes at the microscopic level occur on the material to be joined. As a matter of fact, all three FSW characteristic areas are micro-structural modifications resultant from the mechanical and thermal changes. WN is the most affected one as it undergoes mechanical stirring, resulting in severe plastic deformation and recrystallisation caused by frictional heat generated by the tool in the material workpiece. Most of the time, it presents equiaxed grains in a banded structure. The flow arm zone is at the top of the WN, where the grains are finer as a result of more intense stirring from the tool shoulder [70]. On the other hand, TMAZ tends to go through some plastic strain without recrystallisation. Visible elongation and rotation of the parent material grain structure occur in this zone

during welding [71]. At last, HAZ, which is common to all welds experiences some thermal cycling, but without any deformation and presents a different micro-structure when compared with the base materials one. The difference in local properties of these micro-structural zones and the presence of defects makes the mechanical behaviour and failure mechanics of FSW a complex subject.

Specimen preparation for this part was not complex but rather a necessary one. A 30 x 12 mm sample was embedded in a small cylindrical container within an epoxy mixture with a ratio of 25 : 3 parts of resin to hardener and left to cure for two days at an ambient temperature. Followed by several stages of grinding and polishing, being the last step a 1 $\mu m$ diamond paste polish, the specimen, illustrated in Figure 3.5 (a) was ready to be analyzed. An *Olympus CK40M* optical microscope paired with a digital camera, with the entire setup represented in Figure 3.5 (b), was used in order to examine the areas with more detail and are presented in Chapter 4.

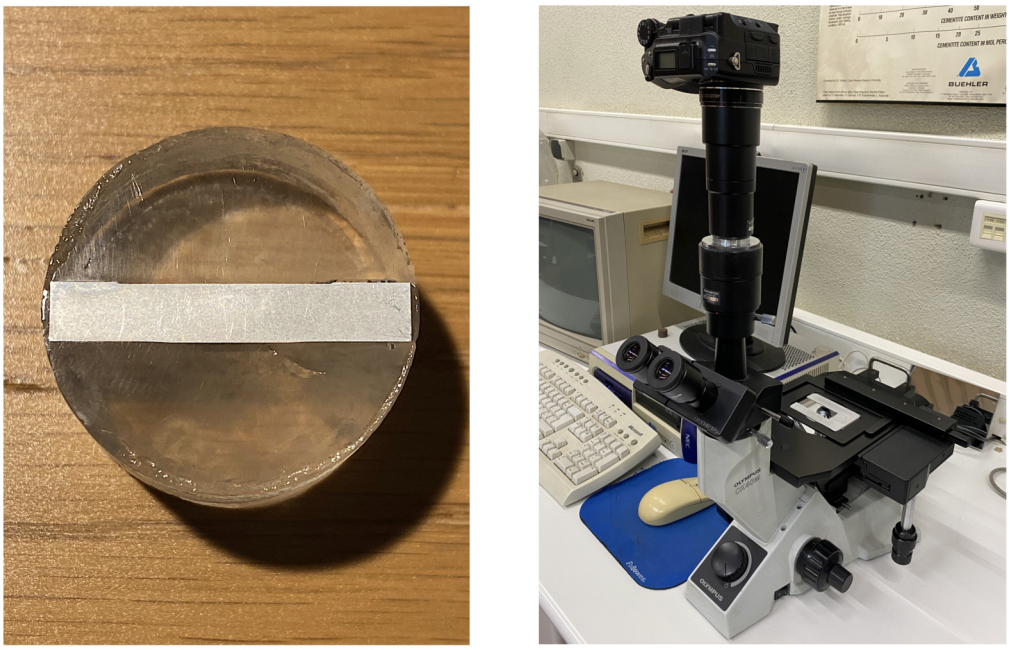


(a) (b)

Figure 3.5: Metalographic specimen (a) and microscopic apparatus (b) used for microstructure analysis

### 3.1.5 Microhardness measurements

Vickers microhardness [72] assessment was performed on the same sample that was used in the microscopic analysis and no additional preparation was done to the specimen. The tests were carried out on *Shimadzu HMV-2* microhardness tester with a load of 200 g and 10 seconds of force duration. Test results on the cross-section of connections for three different measurement lines, upper, middle, and lower, are shown in Figure 4.13.

A total of 117 measurements were made (39 measurements per line), at 1.0 mm (upper), 2.5 mm (middle), and 3.5 mm (lower) from the top of the sample. The middle 10 mm of the specimen were measured with an interval of 0.5 mm between each indentation and, outside of this area, all indentations were made with 1.0 mm between each other.

## 3.2 FCP Testing

### 3.2.1 Specimen design and preparation

This part required the design and manufacture of CT specimen according to ASTM E647 [66] standard. Standards are voluntary documents that set out specifications, procedures, and guidelines that aim to ensure consistent and reliable results that can be easily replicable in any part of the world. The geometry of the designed specimen is shown in Figure 3.6.

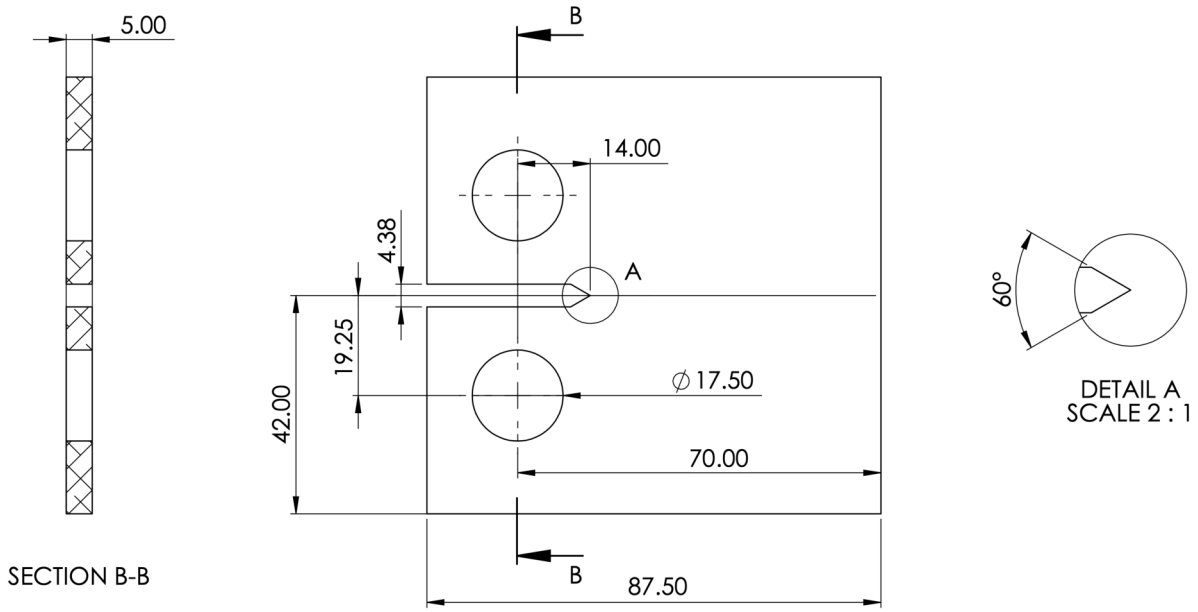


Figure 3.6: CT specimen drawing according to ASTM E647 standard

The reason behind the choice of the CT specimen is the existence of a notch. According to the theoretical concepts presented in Chapter 2, notches and acute angles are known to be stress concentrators that help to develop a rapid growth of cracks under cyclic loading. As the main objective in the development of this investigation was to study the speed of FCP across FSWed characteristic zones and the shortage of testing material was also an issue, these fit perfectly in the needs of the present study.

For that matter, a series of criteria respecting the size of the specimen as well as the size of valid crack growth had to be respected in order for the results to be considered valid from the scientific standpoint.

According to ASTM E647 [66], this validation comes from the first criterion where it is stated that the specimen must be predominantly elastic at all values of applied force. For CT specimen, this criterion can be translated in the following expression

$$(W - a) \geq \left(\frac{4}{\pi}\right) \cdot \left(\frac{K_{max}}{\sigma_y}\right)^2 \tag{3.1}$$

where $(W - a)$ is the specimen's uncracked ligament, $K_{max}$ is the maximum SIF, and $\sigma_y$ is BM's 0.2% offset yield strength. The load applied to the specimen was $P_{max}$ = 4 kN, as it allowed for a satisfactory crack growth length of approximately 33 mm according to the expression 3.1, falling short of 2 mm

of FSW joint width, *i.e.*, HAZ RS - the underlying reasons for this decision will be better explained in Chapter 4.

As already mentioned, all the specimen were produced using wire EDM, a technique that allows for great precision cuts. In order to be able to observe crack propagating, CT specimen had to be subjected to several treatment and machining processes, among which surface milling on both sides, grinding with five different wet sandpapers ranging from 300 to 4000 grit, and finally polishing with a fine paste, obtaining, in the end, a surface with mirror-like finish. An example of the first two stages is shown in Figure 3.7.

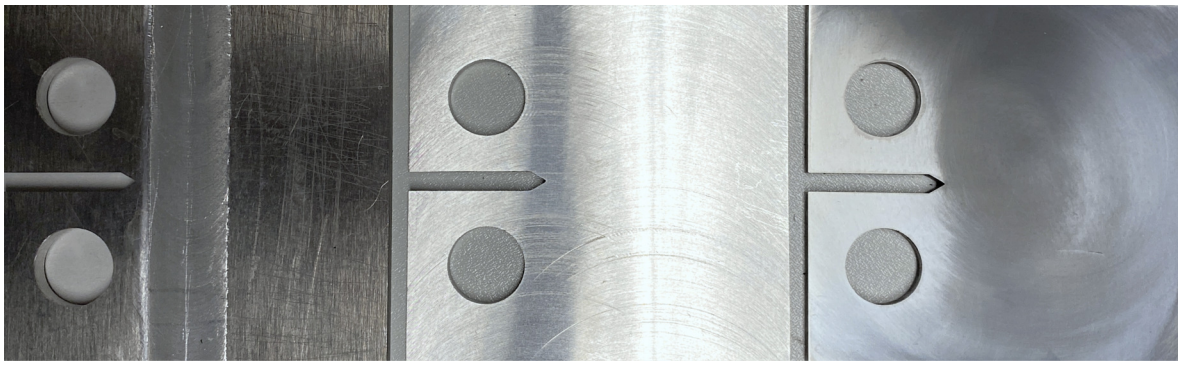

Figure 3.7: Specimen finish from left to right: in the beginning with the FSW joint easily visible, after surface milling, and after grinding with a 2500 grit wet sandpaper

### 3.2.2 Apparatus

The fatigue crack growth rate was evaluated on an *Instron 8502* servohydraulic fatigue testing system with a load cell rated at 10 kN for dynamic purposes. All the tests were performed as per standard ASTM E647 [66]. Monitoring of the cracks was done with the help of two USB digital microscopic cameras, *Dino-Lite Edge* and *Veho Discovery Deluxe*, one for each side of the specimen. Both of them were mounted on purposely designed and fabricated 3D-printed supports, shown in Figure 3.8, and fixed onto vertical metallic rods installed close to the hydraulic pistons of the main testing equipment.

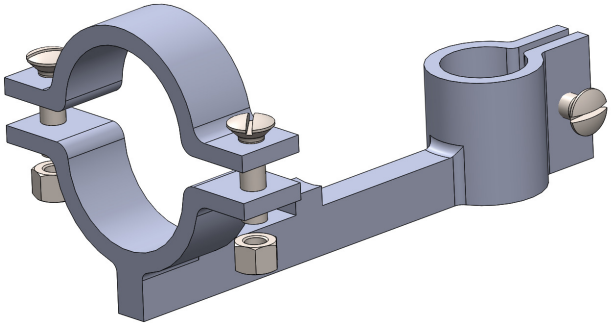

Figure 3.8: CAD of the support for microscopic cameras, designed in *Solidworks*

Additionally, two LED lights were used to illuminate and highlight the cracks as they can only be seen under certain load and lighting conditions. The entire setup can be observed in Figure 3.11.

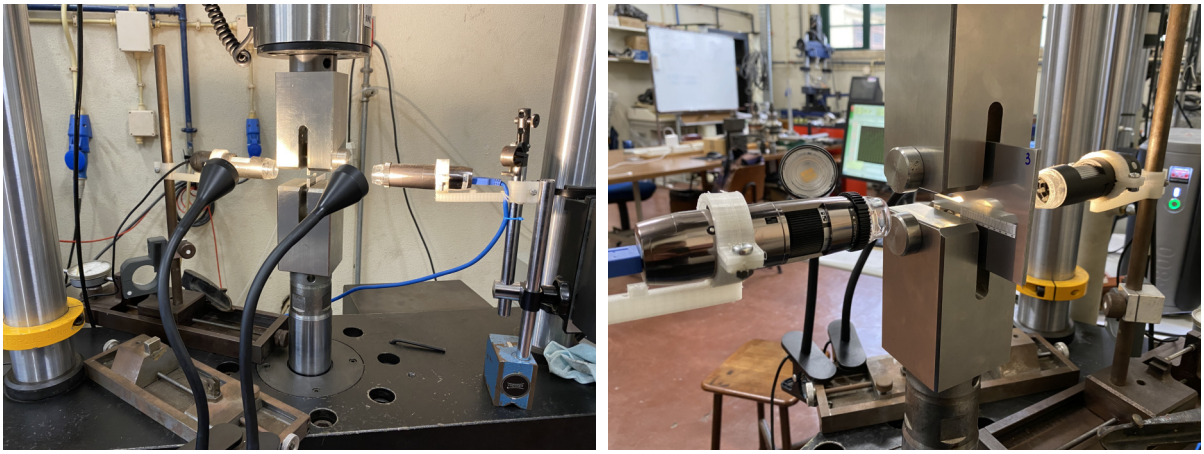

(a) (b)

Figure 3.11: Experimental setup seen from different perspectives, (a) and (b)

For the crack measurements, *Dino-Lite* and *Fiji* software were used. On each side of all three specimens, a real size 40 mm ruler was attached to serve as a calibration scale to the microscopic cameras in order to obtain the most reliable experimental data. Figure 3.12 depicts an image taken during measurement of the crack after a certain amount of cycles, and with $P_{max}$ = 4kN applied to the specimen. The negative effect applied to the image was a technique found to ease the visualisation of the respective cracks.

Crack measurements were taken periodically and were dependent on the FCP rate that was being monitored closely using plots extracted from a spreadsheet in real-time, which will also be presented in Chapter 4 and explained in a detailed form.

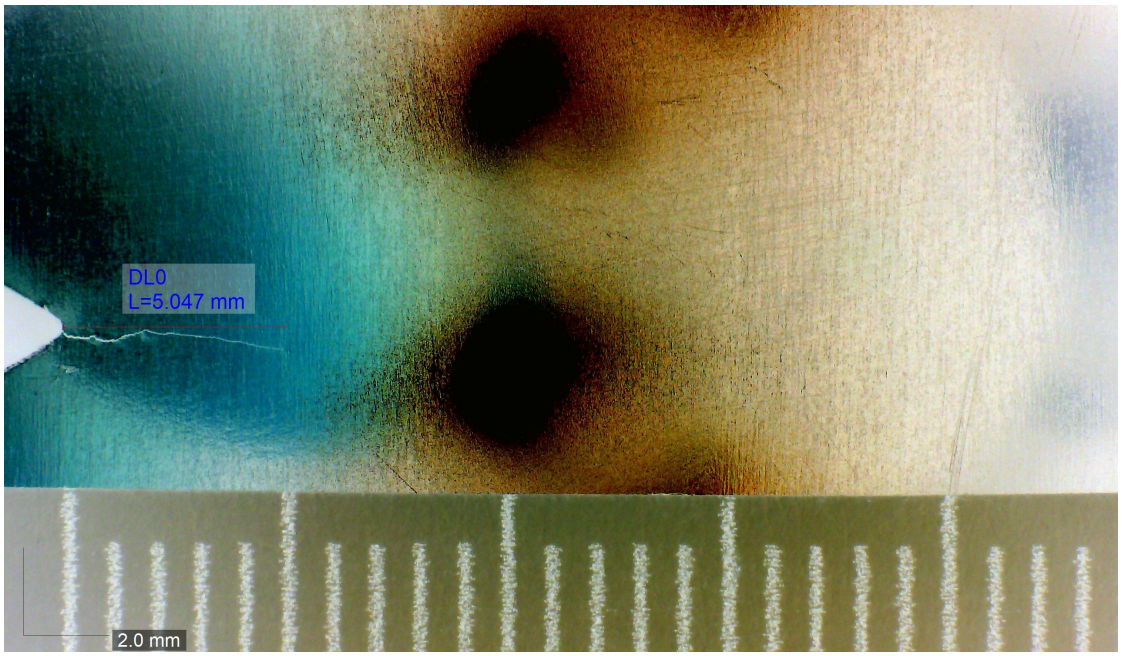


Figure 3.12: Crack visualisation and measurement within *Dino-Lite* software

## 3.3 Finite Element Model

### 3.3.1 Introduction to Abaqus Unified FEA

Abaqus is a commercially available software suite for FE analysis and CAE developed by SIMULIA, a company of Dassault Systèmes®. Due to its powerful and complete tools and solutions, Abaqus revealed to be the best choice to simulate the crack growth behaviour in this case study, as it enables the user to withdraw results that are very similar to the ones predicted in theoretical equations, as long as accurately modeled in the software. The numerical analysis of this Master Thesis was entirely performed in the latest version of this software released in 2020.

A complete Abaqus analysis usually consists of three distinct stages [54]:

1. **Preprocessing** - In this stage user must define the model of the physical problem and create an Abaqus input file. The model is usually created graphically using Abaqus/CAE or another preprocessor, although the Abaqus input file for a simple analysis can be created directly using a text editor.

2. **Simulation** - The simulation, which normally is run as a background process, is the stage in which Abaqus/Standard or Abaqus/Explicit solves the numerical problem defined in the model. Examples of output from a stress analysis include displacements and stresses that are stored in binary files ready for postprocessing. Depending on the complexity of the problem being analyzed and the power of the computer being used, it may take anywhere from seconds to days to complete an analysis run.

3. **Postprocessing** - This is the last stage of the analysis where the user can evaluate the results once the simulation has been completed and the displacements, stresses, or other fundamental variables have been calculated. The evaluation is generally done interactively using the *Visualisation module* of Abaqus/CAE or another postprocessor. This module reads the neutral binary output database file and has a variety of options for displaying the results, including color contour plots, animations, deformed shape plots, and X–Y plots.

### 3.3.2 Specimen and crack modelling

In order to study FM of the given specimen, it must be modeled in accordance with the experimental setup with the same dimensions and material properties considered before, which can be found in Table 3.1. The weld line itself was not modeled into FEM as there is not enough information available in the literature. Such a detailed analysis would require critical parameters such as $E$, $\sigma_y$, $C$ and $m$ for each characteristic FSWed zone.

For the crack geometry modelling, a rectangular *shell* geometry had to be created, as XFEM does not accept geometries with volume as cracks. It has been dimensioned with a 5 mm width, considering the main requirement for crack modelling to be that its width has to be the same as the thickness of the specimen or larger. For static analysis, a variable crack length was used to determine a corresponding

value of $K_I$ to later be compared with theoretical approximations provided by Equation 3.2 as in ASTM E647 [66] standard.

After modelling both, an assembly between them was made with the crack beginning at the end of the notch, as can be observed in Figure 3.13.

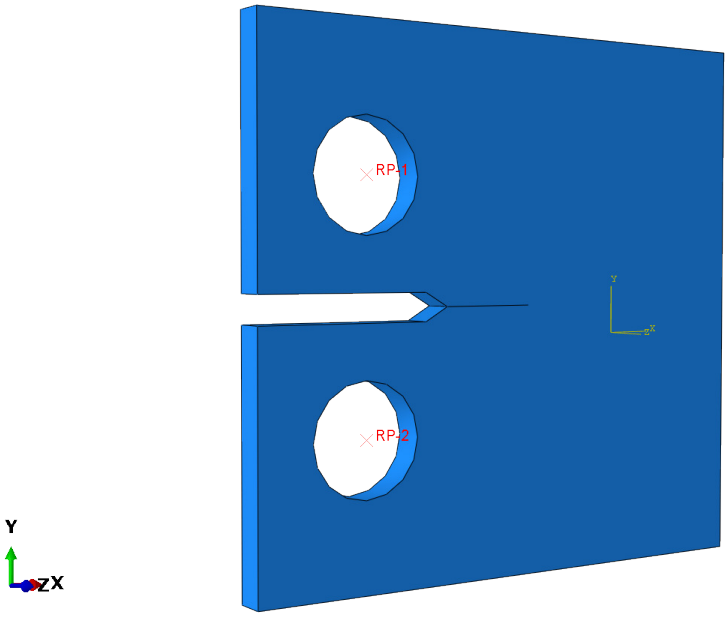


Figure 3.13: Perspective of the assembly between CT specimen and crack with a length of 15 mm

Once assembled and with the material defined, crack geometry needs to be recognized by Abaqus as crack. This is done in the *Interaction module*, under the tab named *Special* $>$ *Crack*. Crack location is specified on the assembly and the solution type, namely XFEM, is also chosen. One of the main differences between static and cyclic analysis, as will be discussed ahead, is that during crack configuration, in the first case crack growth is not allowed, so the correspondent option remains unchecked, while during fatigue analysis this option must be selected so it can grow under Paris law conditions with the increasing amount of cycles.

### 3.3.3 Pin modelling and boundary conditions

Considering that current numerical analysis tries to replicate the experimental setup as closely as possible, after modeling the specimen it was time to model the loading apparatus and establish boundary conditions for the movement of its pins. To do that, firstly a reference point was generated in the geometrical centre of each hole. After that, a *coupling* function was used to join the reference point of each hole with the respective inner surface. This *coupling* between them generates a *virtual pin* and tells Abaqus that during simulation, the load must be applied exactly at the geometrical centre of each pin-hole assembly.

When it comes to Boundary Conditions (BC), these are usually defined as the limits of a certain problem outside of which the problem can not be solved or simply has no valid meaning, or, in other

words, it states the domain of the problem. For the given problem BC are applied to simulate the correct behaviour of the specimen when being loaded by limiting degrees of freedom of each pin, as it happens during the experimental part of this case study - the lower pin is fixed in all directions except for the rotation around its transverse axis and the upper pin, where the load is applied, is allowed to rotate around the same axis as the lower pin and is allowed to move upwards. As we want to replicate loading Mode I as accurately as possible, it is imperative to set up these BC correctly. Figure 3.16 and Table 3.4 display a visual representation of the explanation above.

Table 3.4: Degrees of freedom configured into the model

| | **Translation** | | | **Rotation** | | |
|---|---|---|---|---|---|---|
| | **X** | **Y** | **Z** | **X** | **Y** | **Z** |
| **RP1** | Fixed | **Free** | Fixed | Fixed | Fixed | **Free** |
| **RP2** | Fixed | Fixed | Fixed | Fixed | Fixed | **Free** |

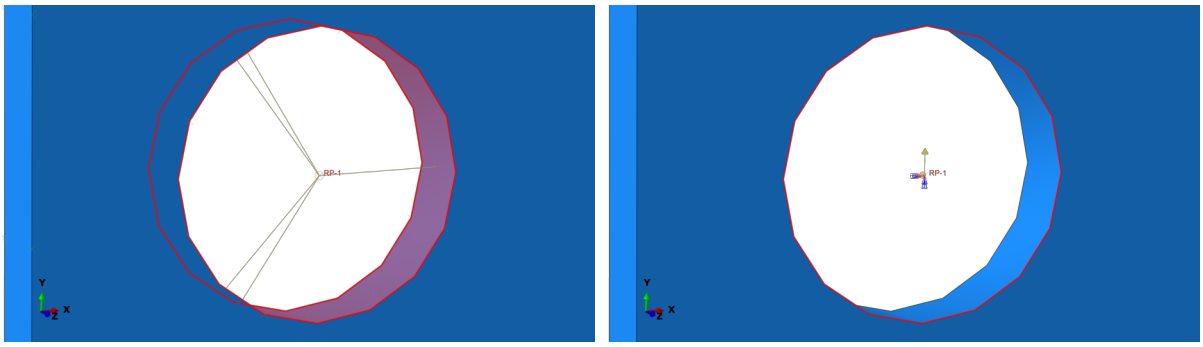

(a) (b)

Figure 3.16: Representation of modelled virtual pin (a) and BC with the respective load applied to the upper pin (b)

### 3.3.4 Model meshing

The idea behind meshing in FE analysis is to transform a continuous domain of an object with an infinite number of DOF, to a finite number of pieces or elements, with a solvable amount of equations. The proper meshing of the model is of extreme importance as it is directly responsible for the accuracy of the final solution.

In the present case study, two different situations were investigated - a static one for $K_I$ calculation, and a dynamic one for FCP simulation. In both cases, the mesh was constructed with the help of 8-node brick elements with linear geometric order. C3D8R elements, with reduced integration, were used in the global mesh with a size of 1.5 mm per element for static and 2.0 mm per element for cyclic analysis, but a different approach for local meshing was considered as it required a greater number of elements for accurate results to be calculated.

For the purpose of $K_I$ determination, the first step was to define local mesh at the crack front and refine it down to a level where a balance between computation time and the accuracy of results was found. To do that, a small 1 x 1 mm$^2$ area was defined at the crack front as can be observed in Figure

3.17. Because it is an enriched area in the model, C3D8 elements were applied in it as these present a greater accuracy in the final solution.

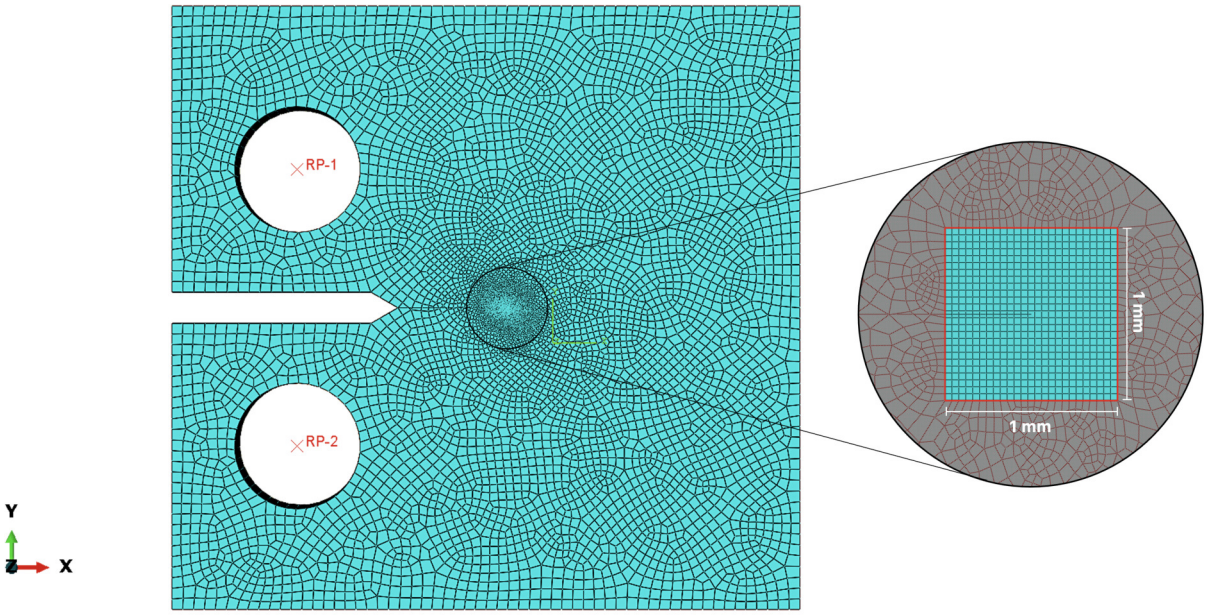


Figure 3.17: Model meshing with a 15 mm crack and a detailed picture of the technique used at the crack front

Table 3.5: Mesh convergence for static analysis

| Mesh | X Y Z | Number of elements | $K_I$ (MPa·mm$^{1/2}$) | Node number | CPU time (s) |
|---|---|---|---|---|---|
| **M1** | 5 5 7 | 35343 | 758.96 | 4 | 14.5 |
| **M2** | 10 10 7 | 42735 | 772.04 | 4 | 16.7 |
| **M3** | 15 15 7 | 49602 | 772.48 | 4 | 22.3 |
| **M4** | 5 5 10 | 50490 | 779.44 | 8 | 26.1 |
| **M5** | 5 5 15 | 75735 | 745.94 | 8 | 97.1 |
| **M6** | 10 10 15 | 91575 | 778.26 | 8 | 56.2 |
| **M7** | 13 13 15 | 100065 | 777.96 | 8 | 63.5 |
| **M8** | 16 16 15 | 109425 | 785.40 | 8 | 169.0 |
| **M9** | 20 20 15 | 123645 | 781.40 | 8 | 86.8 |
| **M10** | 25 25 15 | 125445 | 782.16 | 8 | 85.9 |
| **M11** | 20 20 20 | 164860 | 783.36 | 11 | 380.5 |
| **M12** | 20 20 25 | 206075 | 783.34 | 13 | 665.1 |
| **M13** | 25 25 25 | 209075 | 787.16 | 13 | 697.6 |

Prior to proceeding with $K_I$ calculation for the entire set of valid crack lengths, a convergence study had to be done in order to find the finest set of parameters, with the primary convergence criteria set to be computation time. For that matter, the crack length was fixed at 15 mm - as will be discussed in Chapter 4, this length provided a small error when compared with the theoretical prediction. A total of 3 parameters varied with each iteration: the number of elements in *x* and *y* directions of the enriched zone at the crack front, and the number of elements in *z*-direction of the entire assembly, which corresponds to the number of elements through-thickness of the model. Furthermore, the number of contours around the crack front was fixed at 5. The SIF for each set of parameters was extracted from *.dat* file generated

during each simulation. For this specific case, $K_I$ calculated by Abaqus is given for each contour and each node through the thickness of the specimen resulting in $5 \cdot (Z + 1)$ values. Only values from the central node were considered in the calculation of the final solution as it not only provides the maximum value of SIF but also the most correct approximation of it. In the end, after 13 simulations, all the data was put together in Table 3.5 and a graphical form in Figure 3.18, where the selected set of parameters was highlighted in red.

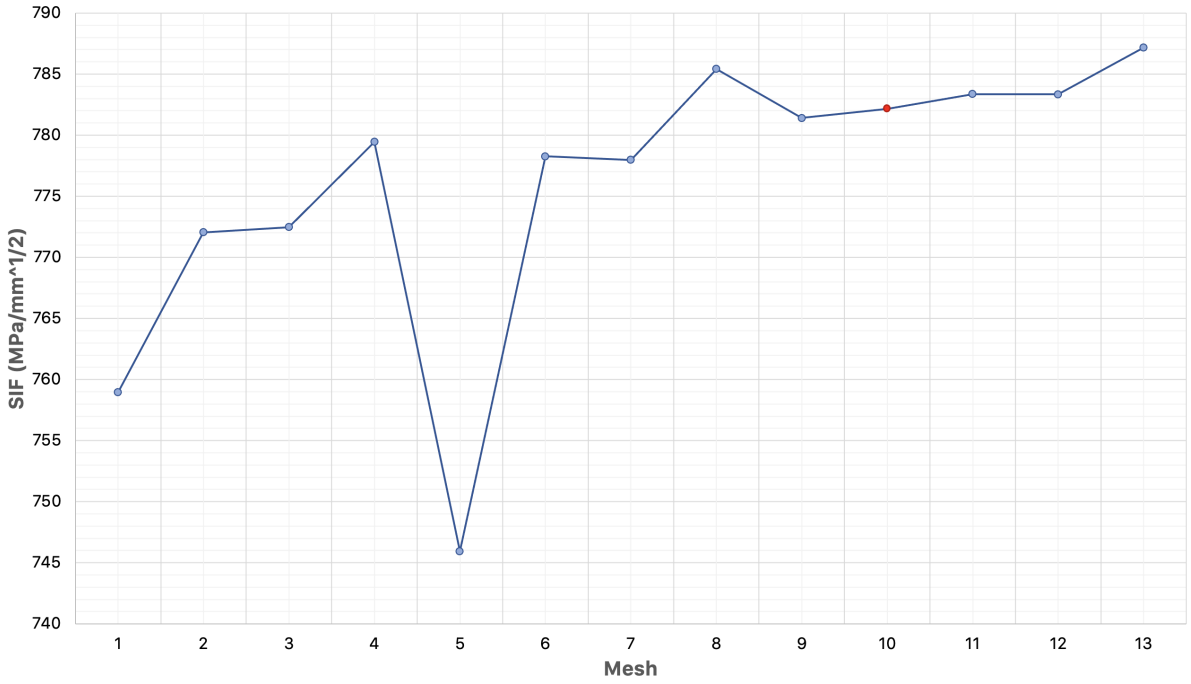


Figure 3.18: Mesh convergence in graphical form

When it comes to dynamic analysis, a different approach had to be implemented in the crack front mesh refinement of the specimen. Taking into account the fact that the crack propagates by itself in an ”uncontrolled” manner, *i.e.*, its length is calculated by Abaqus based on the fracture criteria introduced during the model configuration, a greater region had to be refined in order to account for possible deviations in the direction of FCP. For that reason, entire width of the specimen was refined starting from the notch, as can be observed in Figure 3.19.

The elements used to construct this mesh were the same as in the static analysis, C3D8R for the global mesh with a size of 2.0 mm per element, and C3D8 elements for the enriched area where the crack shall propagate, with a fixed size of 0.5 mm to ease the crack measurements.

Regarding the size of the elements in through-thickness direction, it was maintained at 0.83 mm per element. This decision resulted from several iterations made with the number of elements in *z*-direction, prior to withdrawing any kind of solution provided by Abaqus. It is a known fact that a greater number of elements in the model requires more computational power and directly impacts the computation time of the simulation. Thus, configuring the model mesh with 6 elements through-thickness direction, not only provided similar results when compared to a bigger number of elements but also reduced the calculation time of the solution, providing the required balance between accuracy and time.

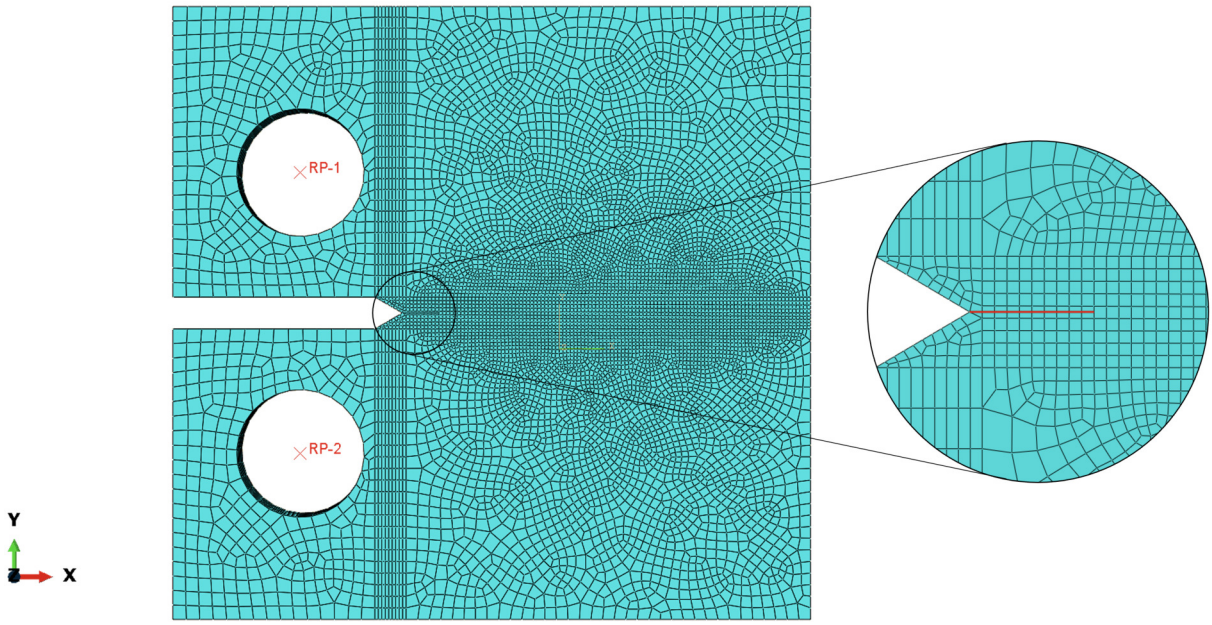


Figure 3.19: Model meshing with a 5 mm pre-crack and a detailed picture of the technique used to mesh the entire area where FCP shall occur

### 3.3.5 Static analysis

The main objective of this analysis was to evaluate and later on validate, the correct parameters set to the numerical model with varying crack size. With this simulation, it was possible to calculate $K_I$ for a range of crack lengths and compare them to theoretical values by the formulation given in 3.2.

For that matter, a nominal load of $P_{max}$ = 4 kN was applied to the upper pin of the model, with the purpose of having a Mode I only loading. The loading itself is done in two time steps, with a total duration of 1 s, where in the initial time step there is no load applied and in the second one, a maximum load is applied. In other words, the growth of the load over this time period is gradual. Because the main goal in this analysis was to measure the SIF for the entire range of valid crack dimensions, this process was iterative and required manual change in crack length after every simulation, *i.e.*, the measurements were taken every 1 mm.

In regards to the model validation, Expression 3.2 [66] was manipulated to calculate theoretical values of $K_{max}$ by replacing $\Delta P$ with $P_{max}$, with the results presented in Table 4.3 and analyzed in the same Chapter.

$$\Delta K = \frac{\Delta P}{B \cdot \sqrt{W}} \cdot \frac{(2+\alpha)}{(1-\alpha)^{\frac{3}{2}}} \cdot (0.886 + 4.64\alpha - 13.32\alpha^2 + 14.72\alpha^3 - 5.6\alpha^4) \tag{3.2}$$

with $\alpha = a/W$ and $a/W > 0.2$.

At last, the only three parameters required to perform the given analysis from the elastic standpoint were $E$, $\nu$, and $\sigma_y$, and can be found in Table 3.1.

### 3.3.6 Cyclic analysis

The direct cyclic analysis was used to simulate crack growth under fatigue conditions to, later on, be benchmarked against the theoretical values using Paris' law and experimental data. A similar nominal load of $P_{max}$ = 4 kN was applied in this analysis with the purpose of allowing a satisfactory maximum crack growth length of about 33 mm, complying with the ASTM E647 [66] standard requirement and with the region of interest. The only difference from the static analysis is that the load was applied in a cyclic mode, allowing the crack to grow while increasing the number of cycles, *i.e.*, it is not pre-determined as in static analysis but calculated within the XFEM. The only elastic material properties assigned to the model in this part were $E$ and $\nu$, presented in Table 3.1.

In this study, the plane stress situation was assumed to calculate the critical energy release rate $G_c$ according to Equation 2.3. Fracture toughness, $K_{Ic}$, as well as Paris constants, $C$ and $m$, for AA5083-H111, were withdrawn from the experimental tests performed by Shahani et al. [73] and are displayed in Table 3.6.

Table 3.6: AA5083-H111 experimental parameters

| $K_{Ic}$ (MPa·mm$^{1/2}$) | C (mm/cycle; MPa·mm$^{1/2}$) | m |
|---|---|---|
| 948.68 | $5.218 \cdot 10^{-11}$ | 2.03 |

An initial crack flaw of 5.0 mm in length was introduced in the assembly to reduce an already long time of computation. After that, the model was attributed a set of parameters in the form of keywords, presented in Table 3.7, to specify crack behaviour during simulation. Constants $c_1$, $c_2$, $c_3$, and $c_4$ refer to the specific material properties, where the first two are responsible for fatigue crack initiation, the other two are responsible for FCP as already discussed in Chapter 2. As the main objective of this numerical study was to investigate FCP and not its initiation, material constants $c_1$ and $c_2$ were kept negligible as 0.001 and 0, respectively. Also, Power law mix-mode model was selected for evaluating the equivalent fracture energy release rate and the respective exponents $a_m$, $a_n$ and $a_o$, were kept with standard values.

Table 3.7: Abaqus parameters used to define the fracture criterion

| $c_1$ | $c_2$ | $c_3$ | $c_4$ | $G_c$ | $a_m$ | $a_n$ | $a_o$ |
|---|---|---|---|---|---|---|---|
| 0.001 | 0 | $4.337 \cdot 10^{-6}$ | 1.015 | 12.802 | 1 | 1 | 1 |

The load was applied in the form of a periodic wave, given by Equation 3.3, with a frequency of 1 Hz and $R = 0.1$, to simulate the exact conditions of the experimental FCP

$$x = A_0 + A_1 \cos(t - t_0) + B_1 \sin(\omega(t - t_0)) \tag{3.3}$$

with $A_0 = 0.55$, $A_1 = 0$, $B_1 = 0.45$, $t = -0.25$ and $\omega = 2\pi$.

### 3.3.7 Final remarks for Chapter 3

This chapter overviewed an entire range of equipment and techniques employed during the development of this investigation. It was split into 3 main parts and covered them as thoroughly as possible to give the ability for anyone to recreate what has been done.

In the first part, an introduction was made to the material used in this study with its main properties tabled and schematics for specimen manufacture presented. It was followed by experimental tests performed on a range of the manufactured specimens that included tensile tests in conjunction with DIC for strain measurements, welding surface roughness measurements, microhardness, and microstructure analysis.

The second part focused on the development of FCP experimental tests that were done according to the ASTM E647 standard. The employed apparatus as well as the crack measurement techniques were described and shown.

At last, FE modelling of the CT specimen closed this chapter with an introduction to Abaqus as a software and the step by step instructions to develop the static and dynamic FE analysis. The main difference between both is the fact that the static analysis does not allow crack growth and was used to validate the model by determining the respective $K_I$ for each crack size in the valid crack domain, while dynamic analysis was performed to evaluate the capabilities of XFEM to correctly simulate the rate of FCP in accordance with Paris law.

# Chapter 4

# Results

This chapter presents all the results obtained in the experimental part of this investigation as well as the numerical part performed in Abaqus using the XFEM-based LEFM approach. In this section, a series of results withdrawn during both parts are presented and analysed in detail.

## 4.1 Experimental Results

### 4.1.1 Joint roughness measurements

A total of 90 measurements have been taken and an average of $R_a$ was calculated for each of the three FSW zones, presented in Table 4.1. A complete set of measurements can also be found in Table A.1. These results are in line with what can be found in the available literature on this topic with the SZ presenting the lowest value, as in [74].

Table 4.1: Obtained $R_a$ measurements. Units are in $\mu m$

| | **TMAZ + HAZ AS** | **SZ** | **TMAZ + HAZ RS** |
|---|---|---|---|
| **Total Mean Value** | 1.016 | 0.914 | 1.113 |

In Figure 4.1 can be observed a 3D image that was stitched together from a total of 189 smaller images. It can be clearly seen the circular marks left by the tool during welding and a central line that was made on purpose by a caliper, to serve as a guideline during the process of the specimen manufacture. The 2D profile across the entire weld, represented in Figure 4.2, reveals the existence of a ”valley” in the central part of the weld with an approximate depth of 20 - 30 $\mu m$. A probable cause for the formation of the given ”valley” is the fact that during the stirring process the tool pushes some of the material to the edges of the welding line. This depth is consistent with the volume of material that had to be removed in specimen preparation, with mechanisms such as surface milling, grinding, and polishing, resulting in a final sample thickness of roughly 4.5 mm.

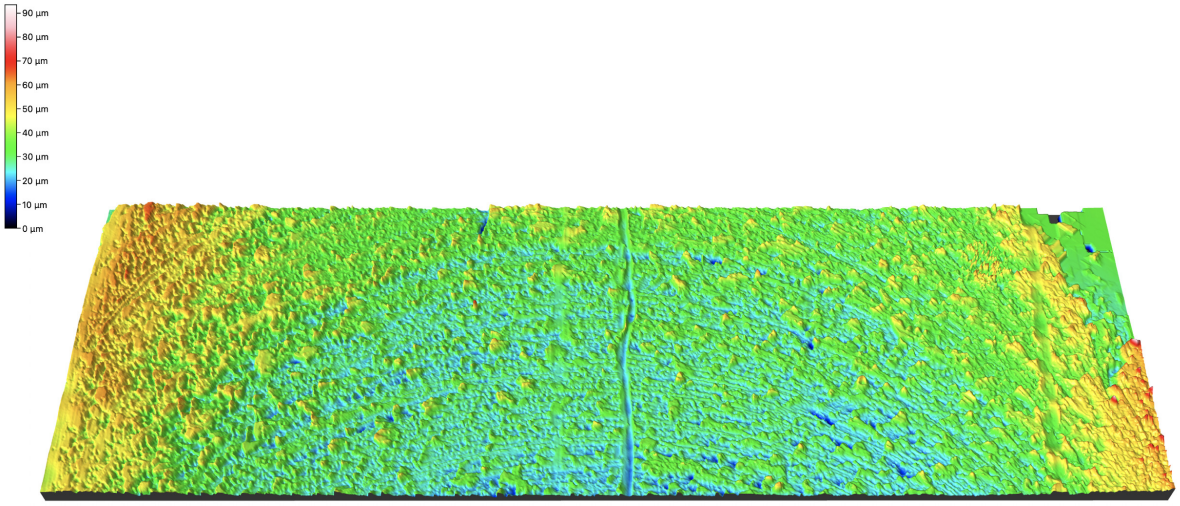


Figure 4.1: Optical profilometry image showing surface morphology of a 17 x 5 mm$^2$ area across the weld with a visible center line left by a caliper

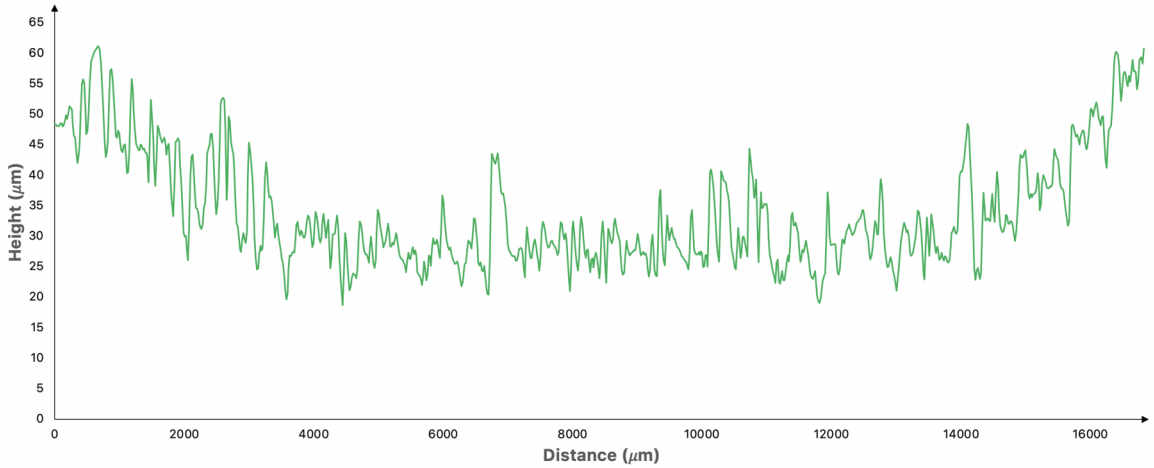


Figure 4.2: Linear profile of the surface represented on Figure 4.1

### 4.1.2 Tensile tests

Nominal stress-strain curves extracted from DIC analysis for both specimens, 1 and 2, are presented in Figures 4.3 and 4.4, respectively. In order to obtain accurate data from these tests, the rate of data acquisition from the testing equipment had to be set different from the frame rate used to capture images - the first one was writing data with a frequency of 10 Hz while the camera was shooting on a variable frame rate of about 3 FPS. For that reason and to be able to plot the curves, the data acquired from the testing equipment had to be interpolated with the amount of data available from DIC post-processing. This was done in *Matlab* software using a one-dimensional linear interpolation function called *interp1*. In the end, the extracted stress vector had the same length as the strain vector and it was possible to correctly plot the above-mentioned curves.

Each figure is presented with 4 curves, 3 of them corresponding to different characteristic FSW areas (TMAZ AS, SZ, TMAZ RS) and another one corresponding to a virtual clip gauge with a length

of 25 mm (REF), used as a reference value to measure strain in the center of the specimens. All the measurements were extracted from the middle of each specimen and clip gauges for TMAZ and SZ were applied based on the information extracted from microhardness testing, in Figure 4.13.

A first direct comparison between two graphs reveals a greater tensile behaviour in specimen 1 than in specimen 2, due to greater maximum stress and strain values observed in Figure 4.3. While in Figure 4.4 all curves display similar elastic behaviour, in Figure 4.3 reference strain gauge revealed the greatest value of $E$, followed by the values of SZ, TMAZ AS, and TMAZ RS. Also, an irregular shape of all curves should be noted as it might represent a possible tensile slippage during the tensile tests.

Overall, the shape of the curves resembles the stress-strain curves obtained for the similar aluminium alloy in the form of a base material [75, 76]. Although, the mechanical properties of the analysed joint deteriorated, with reduction of both, $\sigma_y$ and $\sigma_{UTS}$, due to the heat generated during welding promoting metallographic transformations, hence causing the material to behave differently.

It is possible to observe that different regions of the joint display different behaviours. In both specimens, TMAZ AS presented inconsistent results by having a similar value of strain for two different values of stress. However, SZ and TMAZ RS presented a more in line behaviour in both cases, where SZ displayed a slightly lower ductility when compared to TMAZ RS. This situation is consistent with the measurements taken during microhardness tests with SZ having the highest values, thus lower ductility.

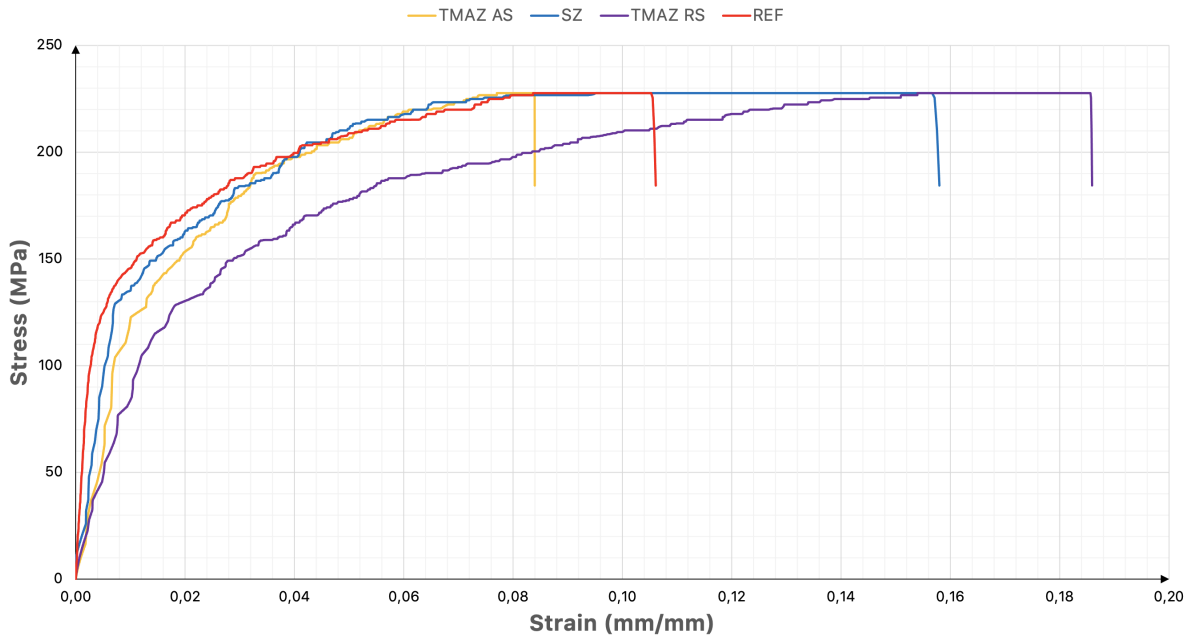


Figure 4.3: Obtained nominal stress-strain curves for specimen 1 from data extracted using DIC

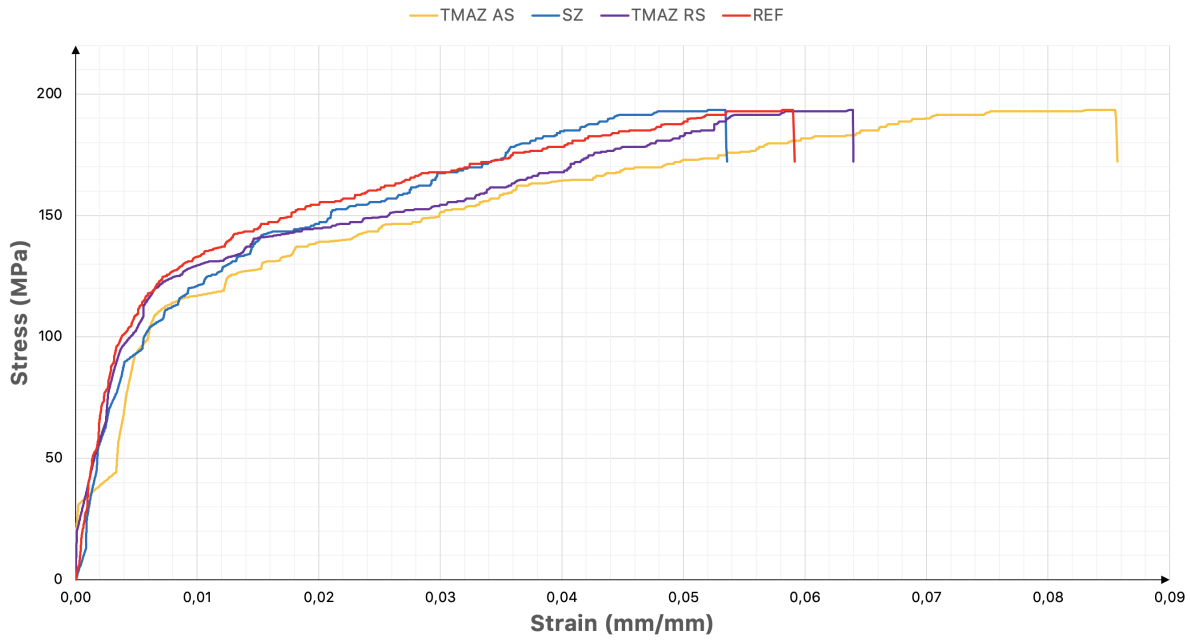


Figure 4.4: Obtained nominal stress-strain curves for specimen 2 from data extracted using DIC

Load-displacement curves were also extracted for both specimens as shown in Figure 4.5, and its maximum values are presented in Table 4.2. Specimen 1 showed greater mechanical properties when compared to specimen 2 with a difference of 34.2 MPa in its Ultimate Tensile Strength (UTS). Nonetheless, both results are far from UTS presented for BM in Table 3.1 or found in the literature [70, 77, 78], having a weld efficiency of, according to Equation 2.1, 76% and 64% for specimen 1 and 2, respectively. Another observation regarding the elastic behaviour of both is that specimen 1 displays 2 different slopes - a steeper one at the beginning, up until 1000 N of load and similar to specimen 2, and another with a more gentle slope until entering the plastic domain.

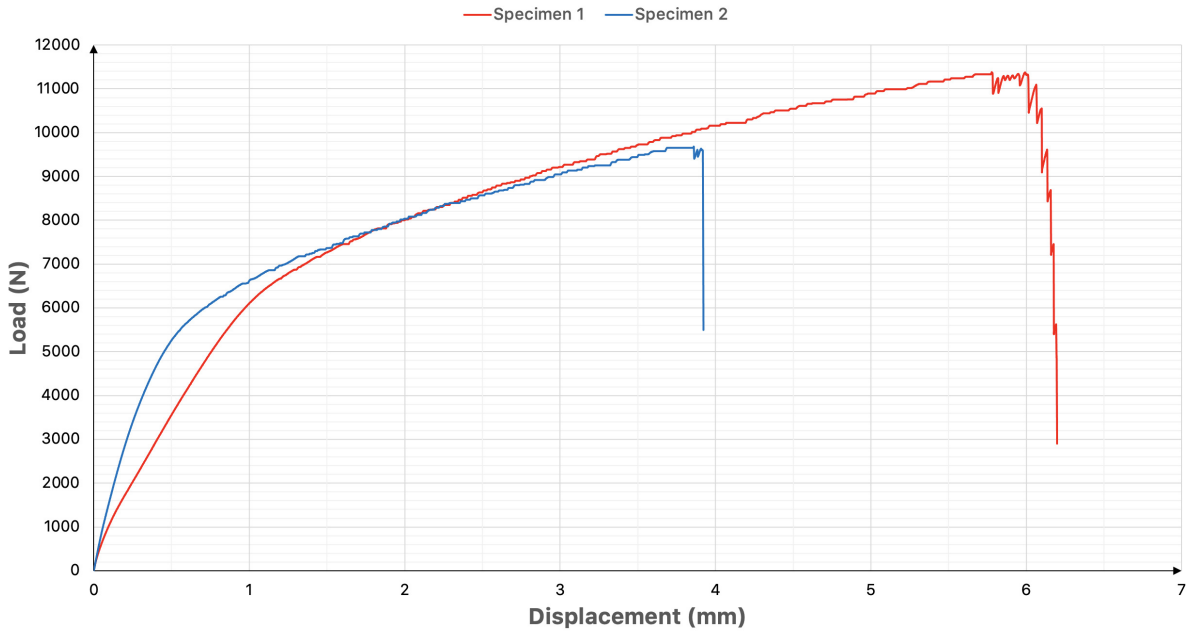


Figure 4.5: Load-displacement graphical representations of tensile specimen 1 and 2

Table 4.2: Maximum load-displacement values for each specimen

| Specimen | Maximum load (kN) | Maximum disp. (mm) | $\sigma_{UTS}$ (MPa) |
|---|---|---|---|
| **1** | 11.38 | 6.20 | 227.70 |
| **2** | 9.67 | 3.92 | 193.50 |

It is also worth noticing the fact that both specimens suffered their tensile failure at approximately the same region, between SZ and TMAZ AS, and with a similar rupture pattern as can be observed in Figure 4.6. The pattern itself is identical to the KB defect, found in microstructure analysis, that runs across the entire thickness of the specimen, and is indeed a critical point that can compromise structural integrity.

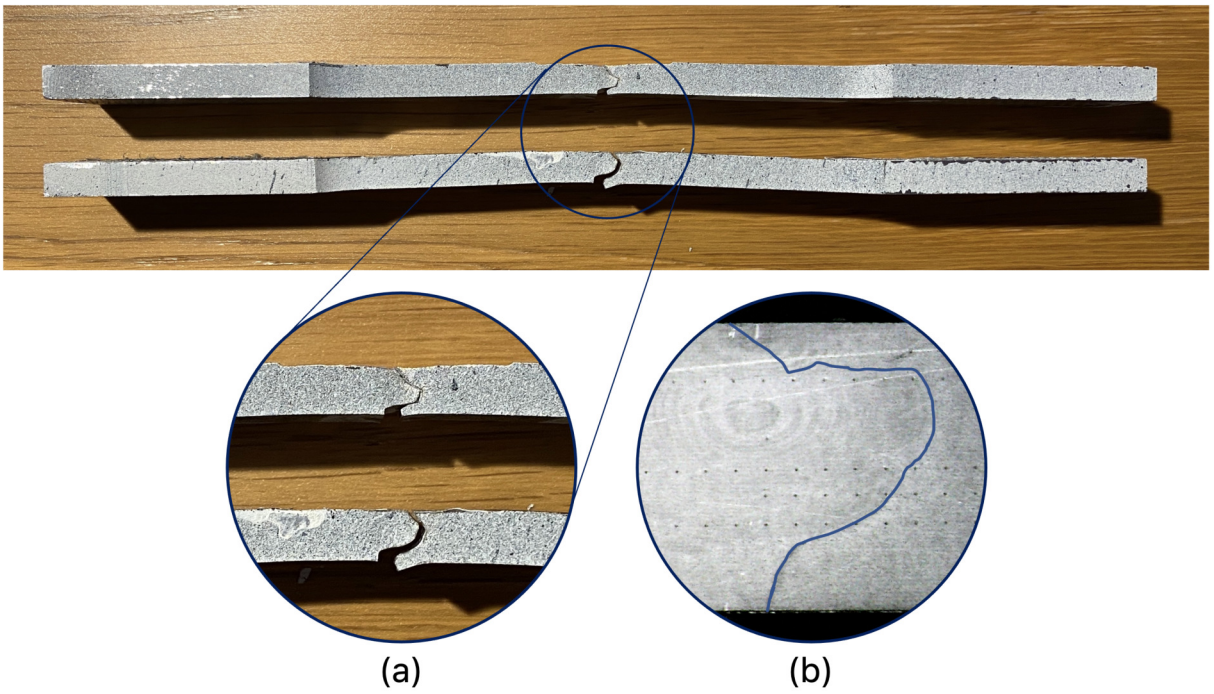


Figure 4.6: (a) Close-up of tensile specimen failure compared with (b) a microscopical image of the cross-sectional area with KB defect represented by a dark blue line

### 4.1.3 Microstructure analysis

At first glance, a macroscopic observation, *i.e.*, with the naked eye, did not reveal any visible defects or imperfections in the joint although SZ could be easily identified.

Although not very clearly seen due to microscopical limitations of the equipment, some grain refinement was displayed in SZ when compared to BM, as shown in Figure 4.9, suggesting that this region underwent dynamic recrystallisation and redistribution of the strengthening phase - this behaviour was confirmed during micro-hardness testing of the sample. In accordance with the Hall-Petch relationship, finer grains have less misalignment and concede to the material higher tensile properties, better fatigue resistance, and better mechanical properties [79]. Due to the grain boundaries not being clearly visible, it was not possible to determine the grain size in any of the analysed areas.

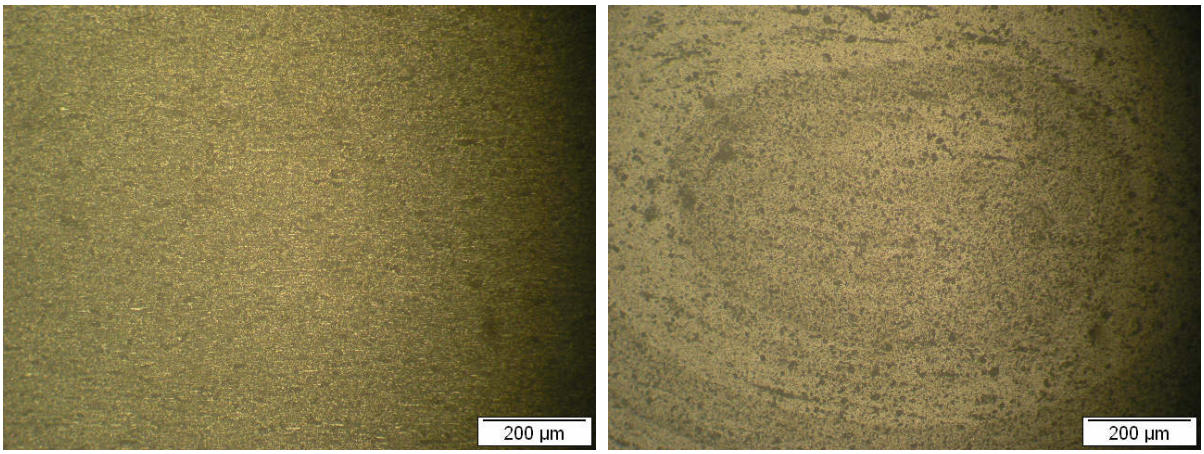


(a) (b)

Figure 4.9: Microstructure of (a) base material AA5083-H111 and (b) stir zone in the metalographic sample. Bigger darker ”spots” indicate the presence of Mg in the alloy

The boundary between TMAZ and SZ is shown in Figure 4.12, on both AS and RS of the weld, respectively. Figure 4.12 (a) unveils a common defect found in FSW called Kissing Bond (KB). A kissing bond is a specific type of defect in solid-state bonding, in which two solid materials are in contact but with little or no metallurgical bonding present. One of the major causes of KB defects in FSW is insufficient penetration of the tool pin into the workpiece material, causing incomplete welding [80]. Schneider et al. [81] also stated that aluminium and its alloys are known to form a native, protective oxide on the surface, $Al_2O_3$. If these native surface oxides are not sufficiently broken up during the FSW process, they are reported to remain in the FSW interior and weaken the bond strength, promoting the formation of KB. Contrarily, Figure 4.12 (b) shows a correct boundary between SZ and TMAZ on RS with no visible sign of defects whatsoever.

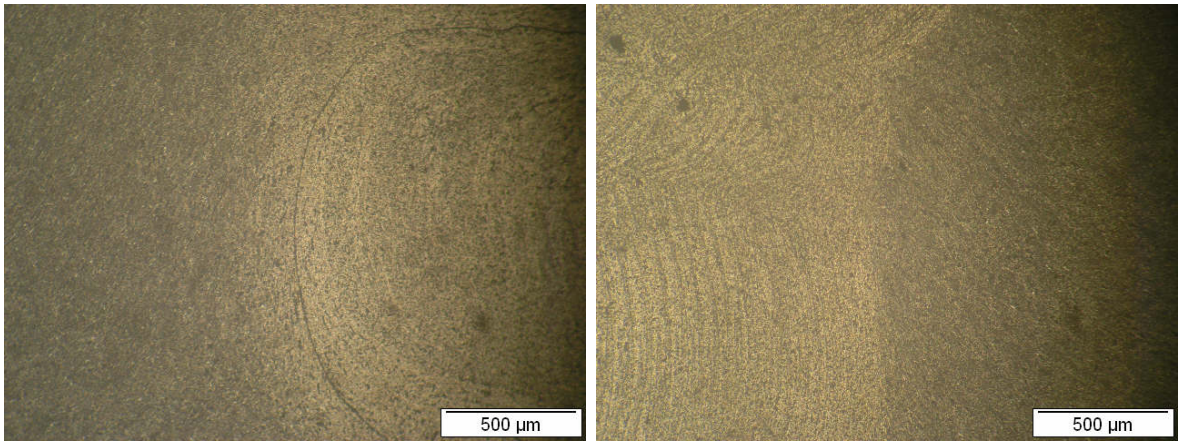


(a) (b)

Figure 4.12: Microstructure of boundary between SZ and TMAZ on (a) AS with kissing bond defect visible and (b) RS with no aparent defects.

Apart from the provided explanation, optical microscopy did not reveal any other interesting observation that should be mentioned.

### 4.1.4 Microhardness measurements

In this subsection, microhardness measurements are analysed. Figure 4.13 illustrates the obtained profiles from 3 different measuring lines taken across the thickness of the specimen, symbolically marked with the dotted lines. In the interval between -5.0 and 5.0 mm from the weld centre, all points are spaced equally with a distance of 0.5 mm from one another. Outside this interval, all remaining points are spaced with a distance of 1.0 mm between one another.

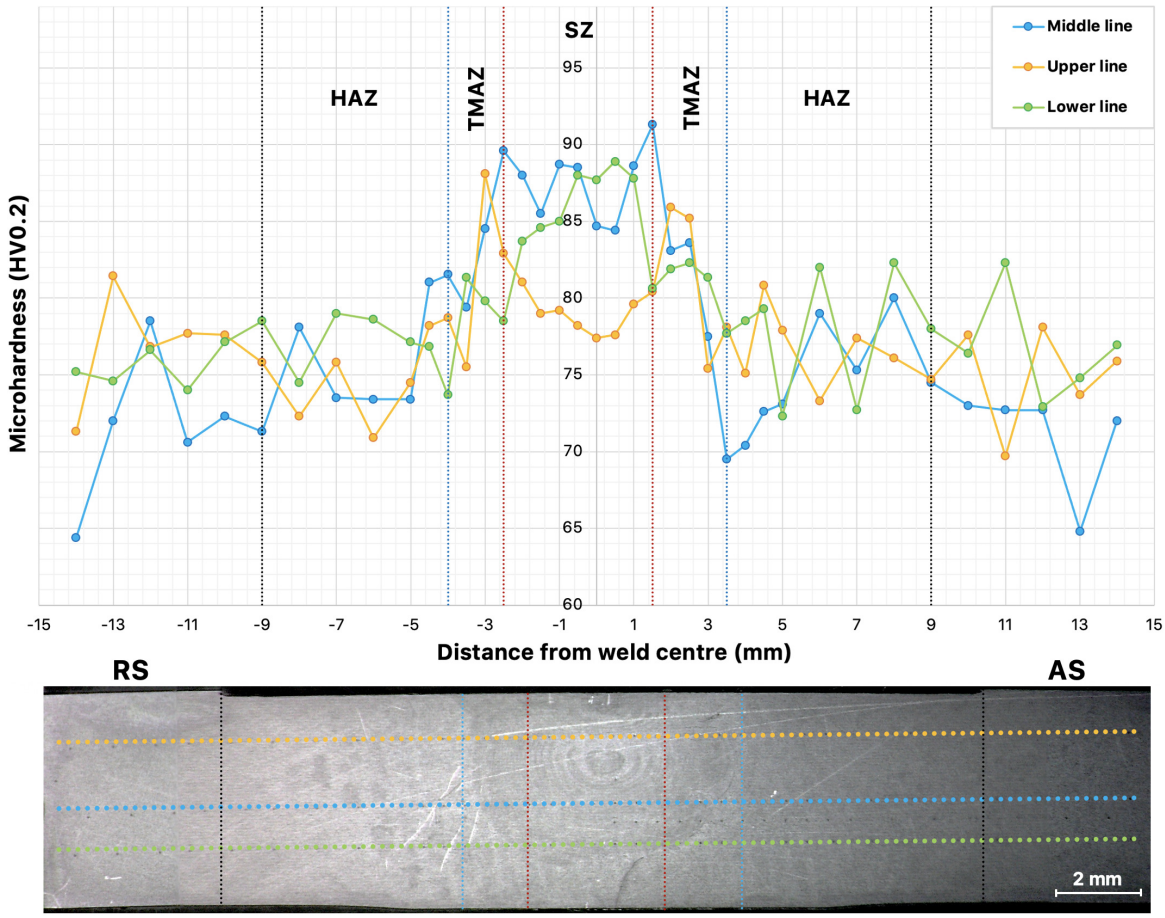


Figure 4.13: Graphical representation of microhardness profiles and a microscopical image of the analysed samples crossection

Upper and middle hardness profiles exhibit some sort of symmetry, unlike the lower profile that manifests an asymmetric behaviour with an irregular profile on AS. In terms of obtained values, these are coherent with what could be found in the literature for AA5083 FSWelded joints [70, 77, 78, 82].

The highest microhardness values were observed in SZ indicating that dynamic recrystallisation occurred in that area and finer grains were formed. However, the upper profile showed a dip in the same area with values very close to ones of BM - this can be explained by the proximity to the top of the weld where the tool softens the material more due to higher temperatures being generated during FSW.

TMAZ showed an accentuated decrease in hardness values to levels of BM as the distance to the center increased due to the coarsening of the hardening phase. HAZ hardness values did not appear to suffer any effect from the heat, presenting values very similar to ones found outside the welding width.

These results confirm the positive influence of grain refinement in SZ area observed in Figure 4.13 on the strength properties of AA5083-H111.

### 4.1.5 Experimental FCP

Experimental results obtained in FCP tests are presented in this subsection. The initial idea behind these experimental procedures was to evaluate the rate of FCP when traversing various characteristic FSW across the entire joint. According to ASTM E647 [66] standard, the highest load that would allow for the entire weld width to be crossed, with a few mm of base material *to spare* on each side of the joint , was $P_{max}$ = 3 kN. This scenario was applied to specimen 1, after opening a pre-crack with an approximate length of 1 mm, using $P_{max}$ = 4 kN and $R$ = 0.1 within 4000 cycles. The tests proceeded as planned and after 655897 cycles applied to the specimen with $P_{max}$ = 3 kN, the crack had grown 0.5 mm, leading to believe that the pre-crack was not opened in the beginning. With an already limited time to do this research and 2 more specimens to be tested, a decision was made to ramp up $P_{max}$, and consider that every cycle and load applied to date served to open a pre-crack with a length between 1.37 and 1.56 mm, depending on the side.

After resetting the cycle counters, $P_{max}$ = 5 kN, $R$ = 0.1, and a maximum frequency $f$ = 4 Hz, were applied to the same specimen. Rapid crack growth was observed from the beginning, with the crack reaching a little over 5 mm in length after 70000 cycles. The total rupture of the specimen occurred when the cycle counter totalled 93210 cycles. This sudden and uncontrolled crack growth can be explained by the possible existence of microscopic cracks provoked by the previous tests with $P_{max}$ = 3 kN, which could not be observed with the available equipment. Another plausible explanation is the existence of voids and imperfections, such as the already detected KB, in the FSW joint itself. Figure 4.14 depicts the fractured specimen with the top and bottom of the crack zoomed-in, where the defects can be observed.

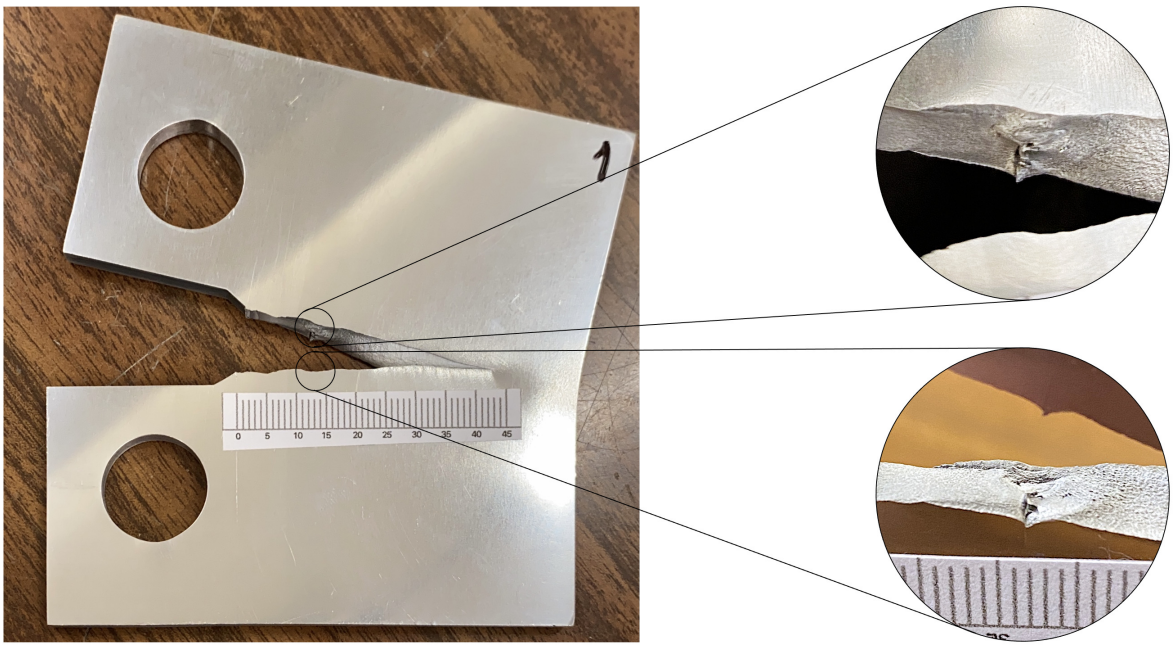


Figure 4.14: CT specimen with apparent defects in the welded joint

The location of the defect is coincident with the location of the previously found KB and with the region where both sheets of aluminium alloy meet, reassuring the fact that this imperfection was present along the entire length of the joint. All the results retrieved during the testing are presented in graphical form in Figures 4.15 and 4.16.

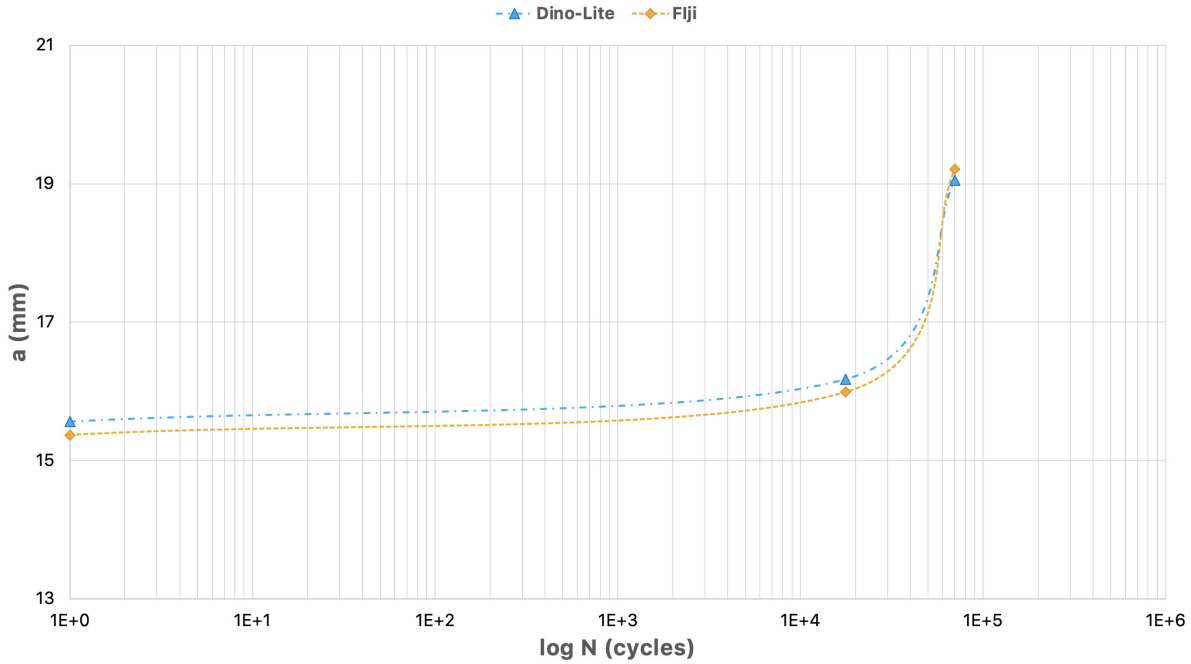


Figure 4.15: Crack growth with $P_{max}$ = 5 kN. Each color represents each side of the specimen and the software used to measure the crack length

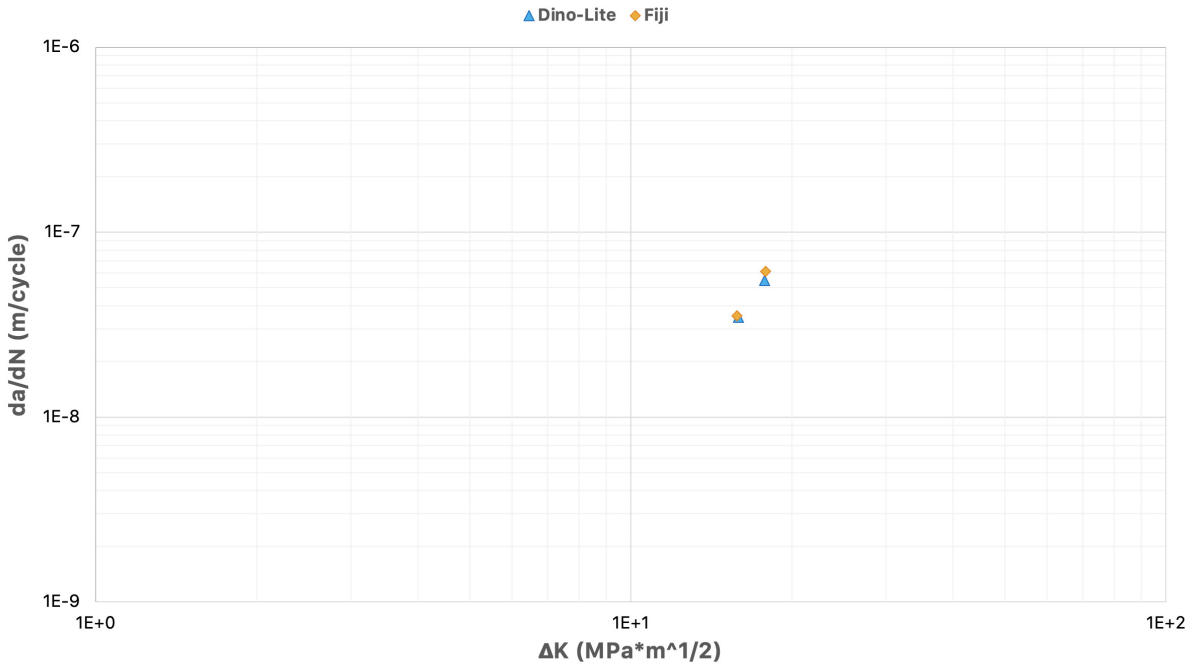


Figure 4.16: FCP curve for $P_{max}$ = 5 kN

Due to rapid FCP caused by $P_{max}$ = 5 kN, it was later decided to test the following specimens with reduced load $P_{max}$ = 4 kN. Not only this cutback would allow covering a greater width of the joint, but also to slow down the rate of FCP. To ensure the opening of the pre-crack, $P_{max}$ = 6 kN and $R$ = 0.1 was

applied to this specimen during 2036 cycles with $f$ = 3 Hz, resulting in an approximate opening ranged between 1.06 and 1.55 mm, depending on the side where it was measured. The tests followed according to plan, with $P_{max}$ = 4 kN, $R$ = 0.1, and $f$ = 4 Hz, up until the failure of the fatigue testing equipment, making it impossible to continue with the experimental FCP. At this point in time, the specimen totalled 170316 cycles and the crack presented a length that ranged between 2.12 and 2.39 mm. In Figures 4.17 and 4.18 can be observed a graphical representation of the collected data for specimen 2. Further analysis is not possible due to the lack of information in this experimental part.

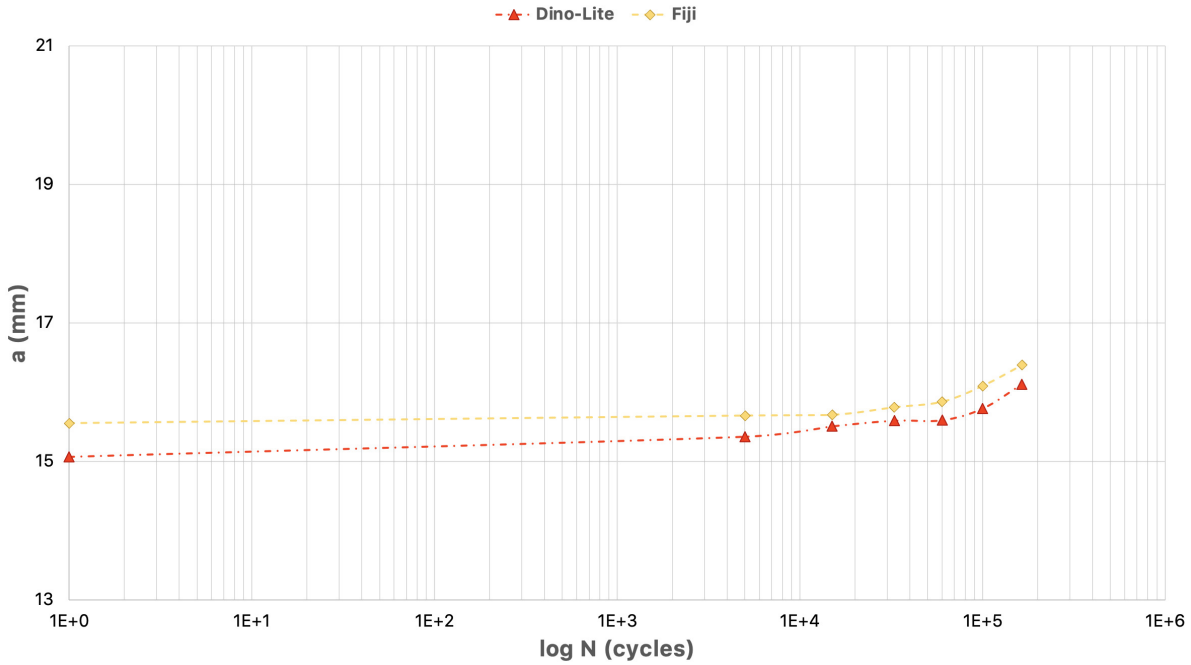


Figure 4.17: Crack growth with $P_{max}$ = 4 kN. Each color represents each side of the specimen and the software used to measure the crack length

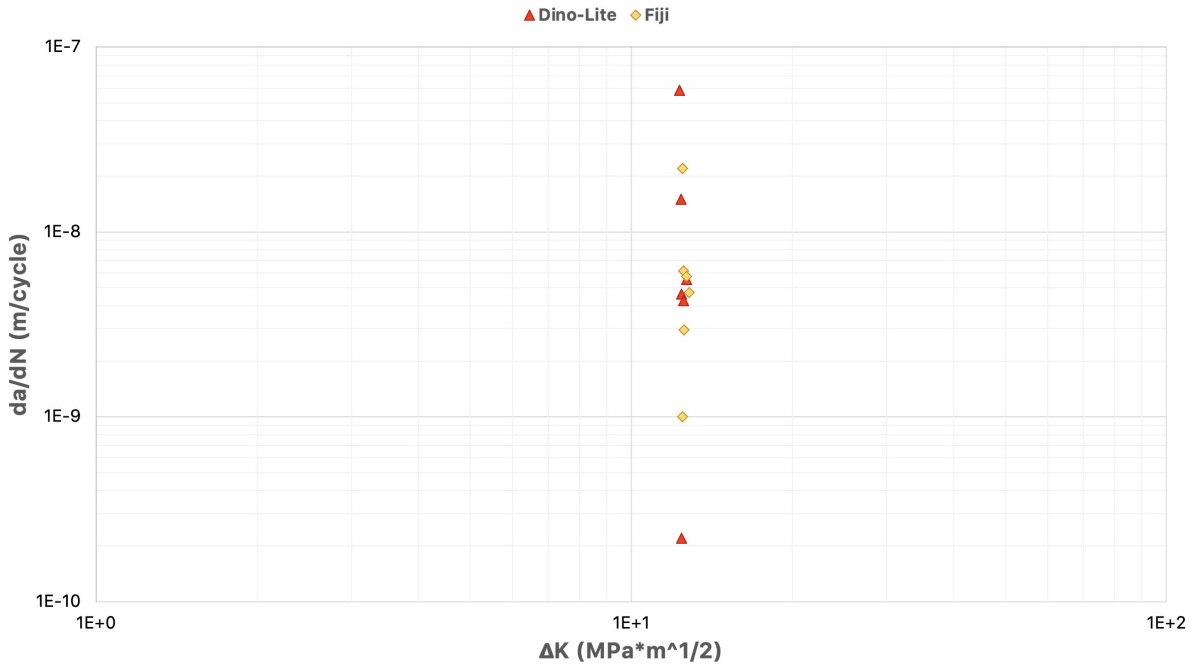


Figure 4.18: FCP curve for $P_{max}$ = 4 kN

## 4.2 Numerical Results

This last section of the Chapter will present and analyse the numerical results obtained from simulations made in Abaqus, using an approximate recreation of the CT specimen with a totally elastic behaviour.

### 4.2.1 Static analysis results

As already explained in Chapter 3, the purpose of the static analysis was to evaluate the accuracy of the model by comparing the SIF values computed within the XFEM, and ASTM E647 standard used as a guide throughout this master's thesis. This was mainly done due to the fact of Abaqus being unable to determine SIF while simulating FCP. For that matter, after studying the mesh convergence and selecting the final mesh configuration, $K_I$ was calculated by Abaqus for the entire valid crack length domain according to the standard.

From the results displayed in Table 4.3, it is possible to observe that with an increasing crack size the error between the theoretical and the calculated XFEM values decreases down to despicable values of a little over 7 %. A greater error, in the beginning, can be explained by the proximity of the crack front to the sharp notch which, mostly because of its geometry, creates difficulties for the software to generate a proper mesh in that particular region. Another possible explanation for the given situation is the fact that the number of elements generated in the mesh increased with the increase of the crack size, leading to greater accuracy in the calculation of the solution. Overall, the number of elements in this analysis varied between 96030 and 136245, for the smallest and biggest crack length, respectively.

Table 4.3: SIF comparison between ASTM E647 and XFEM

| **Crack size (mm)** | **$K_I$ ASTM (MPa·mm$^{1/2}$)** | **$K_I$ XFEM (MPa·mm$^{1/2}$)** | **Error (%)** |
|---|---|---|---|
| **15** | 426.12 | 497.52 | 16.8 |
| **16** | 443.81 | 514.66 | 16.0 |
| **17** | 461.78 | 531.38 | 15.1 |
| **18** | 480.08 | 548.56 | 14.3 |
| **19** | 498.74 | 565.84 | 13.5 |
| **20** | 517.85 | 582.64 | 12.5 |
| **21** | 537.46 | 601.94 | 12.0 |
| **22** | 557.65 | 620.58 | 11.3 |
| **23** | 578.49 | 640.52 | 10.7 |
| **24** | 600.08 | 660.94 | 10.1 |
| **25** | 622.51 | 682.48 | 9.6 |
| **26** | 645.89 | 705.46 | 9.2 |
| **27** | 670.34 | 730.02 | 8.9 |
| **28** | 695.98 | 755.24 | 8.5 |
| **29** | 722.97 | 782.52 | 8.2 |
| **30** | 751.46 | 812.16 | 8.1 |
| **31** | 781.64 | 842.64 | 7.8 |
| **32** | 813.70 | 874.94 | 7.5 |
| **33** | 847.87 | 911.30 | 7.5 |

Figure 4.19, which gives a graphical representation of the information written in Table 4.3, made it possible to make yet another observation about the obtained data that may not be so evident by only looking at the table. Although there is a difference in magnitude, the SIF obtained from XFEM shows a similar trend when compared to the ASTM E647 curve. The reason behind this deviation may lay in the difference of the shape factor $Y$ definition. While in the standard, the shape factor is given based on an extensive experimental database of the same geometry, in Abaqus the shape factor must be calculated based on another more broad expression valid for a range of different geometries.

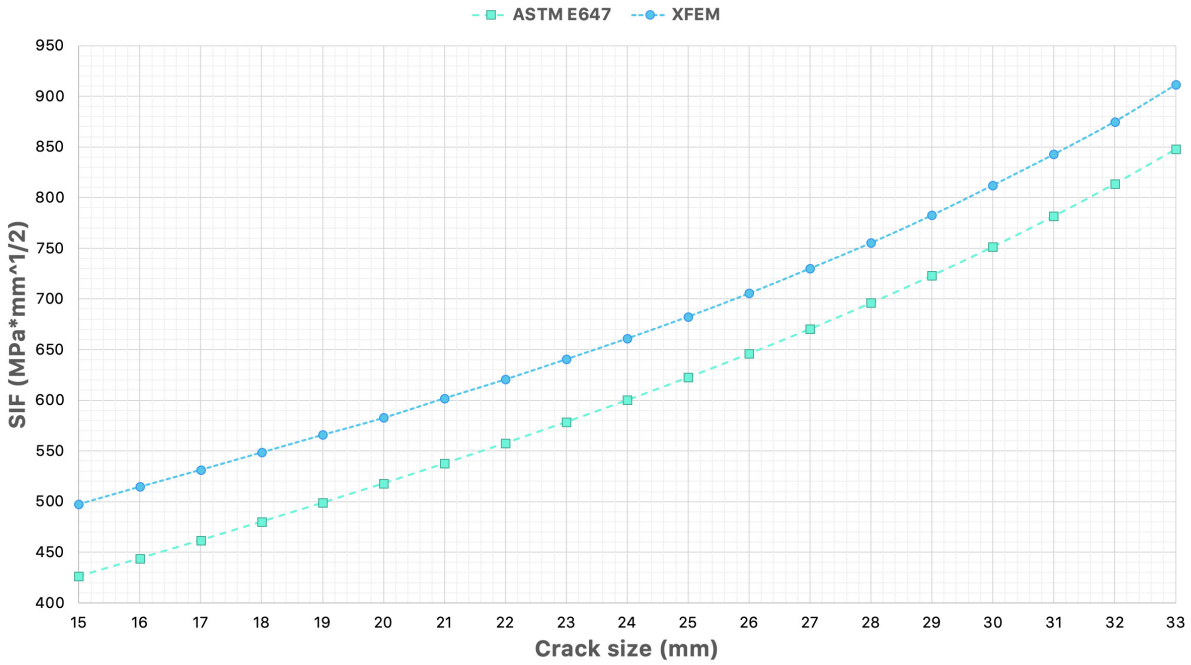


Figure 4.19: SIF estimation for XFEM model validation

Another possible explanation for the variation observed in Figure 4.19 can be attributed to the through-thickness effect found at the crack tip. This complex mechanism is observed in 3D models, where SIF is not constant at all nodes across the thickness of the specimen, as shown in Figure 4.20. Maximum values of SIF can be observed in the central nodes of the specimen with a decreasing behaviour of the calculated parameter towards the surface. On the other hand, the dashed line represents the theoretical value calculated for the same crack length according to the standard that is considered to be constant along with the entire thickness of the specimen.

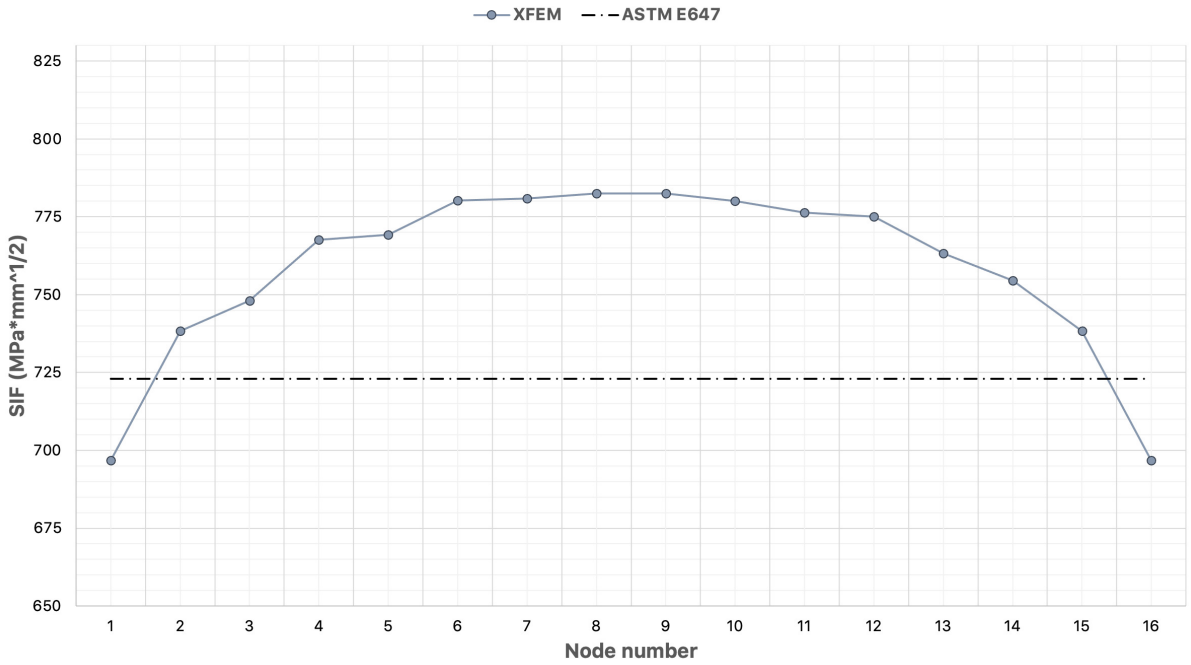


Figure 4.20: Comparison of SIF distribution across the thickness of the model, with 29 mm crack size

### 4.2.2 Dynamic analysis results

The final topic of this research presents the results of a dynamic analysis of FCP simulated in Abaqus. The primary goal of this simulation was to compare the results withdrawn from the software with the experimental study of FCP, by introducing a similar field of residual stresses caused by FSW in the modelled specimen. Considering the difficulties found during the experimental analysis and the small amount of information collected to be compared with, the idea was rapidly dropped, and replaced with a comparison between theoretical and numerically calculated values.

For that matter, and after many iterations, a final mesh with 47616 elements was generated with the majority of them being present in the enriched area for an accurate crack growth prediction. During the simulation, FCP occurs perpendicular to the load applied by splitting the element into two parts. After the element is entirely cracked, the load is redistributed for the next cycle, and the SIF is captured based on fracture energy release. This energy release is accounted by the following element ahead of the crack tip when the previous one is completely fractured. The entire process is repeated respecting the fracture criteria configured at the beginning (Table 3.7) up until the established number of cycles for the simulation is attained. In the end, the number of load cycles was precisely noted for every cracked element as the fatigue crack propagated over time.

When it comes to the crack propagation itself, the end result correspondent to the last value inside the valid crack domain, *i.e.*, $a$ = 33 mm, was achieved after 685189 cycles on one side and 752113 cycles on the other. The discrepancy between both values is attributed to the way the FCP happens within the software. Two fracture mechanisms were observed during the simulation - an initial one characterized by a *regular* FCP mechanism in through-thickness direction, and an *uncontrolled* one with an irregular fashion after a certain crack length is achieved. The irregular behaviour is observed

when the crack propagation changes its direction and intersects the boundary between the elements, as shown in Figure 4.21, thus forcing the calculation to become more complex.

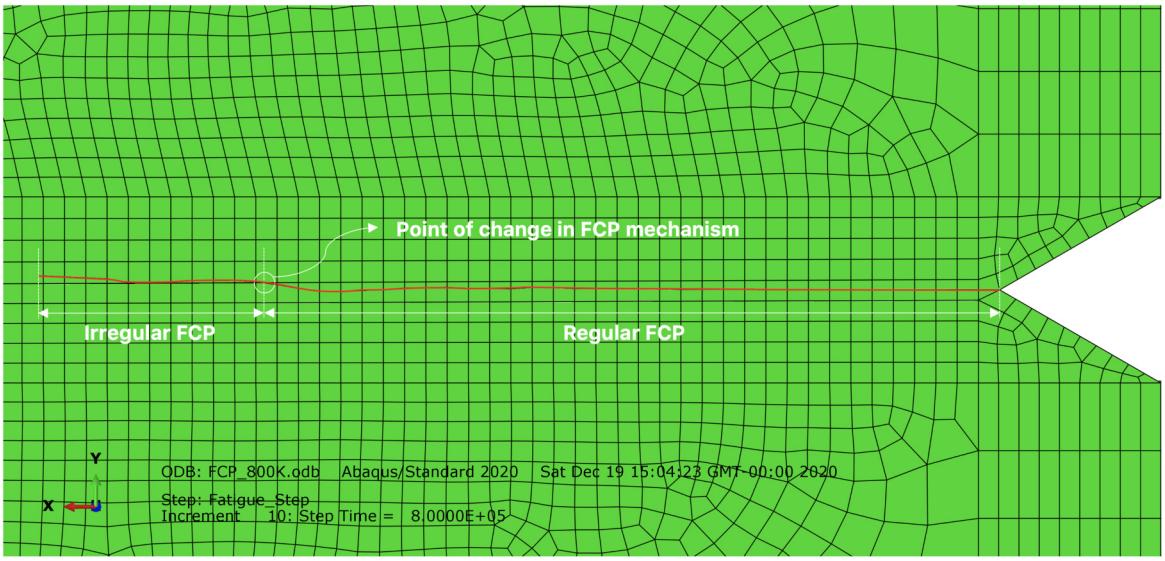


Figure 4.21: Representation of FCP mechanisms in Abaqus

Moreover, in Figure 4.22 is depicted a 3D image of the crack itself where it is possible to observe FCP behaviour through the thickness of the specimen.

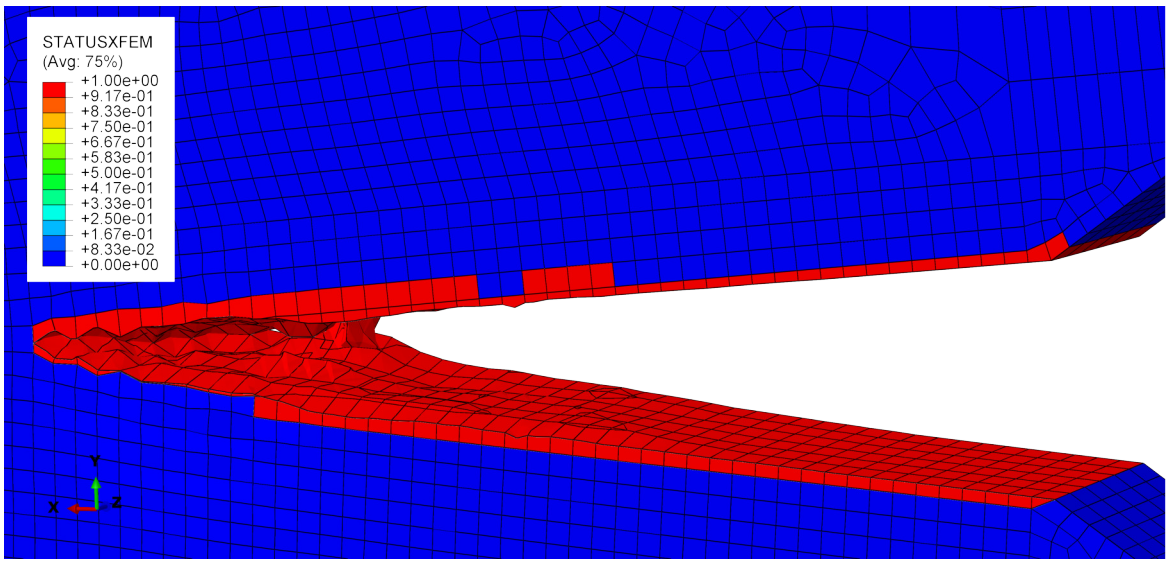


Figure 4.22: 3D image of FCP through the thickness of the specimen

As for the results, these were plotted in the common form in Figures 4.23 and 4.24. Overall, the results were found to be similar to what was expected from theoretical equations given by Paris law. The FCP rate represented in Figure 4.24 showed a good agreement between the points extracted from Abaqus and the Paris law prediction. Greater dispersion of the extracted points can be observed on the right-hand side of the plot, symbolizing the change in the FCP mechanism.

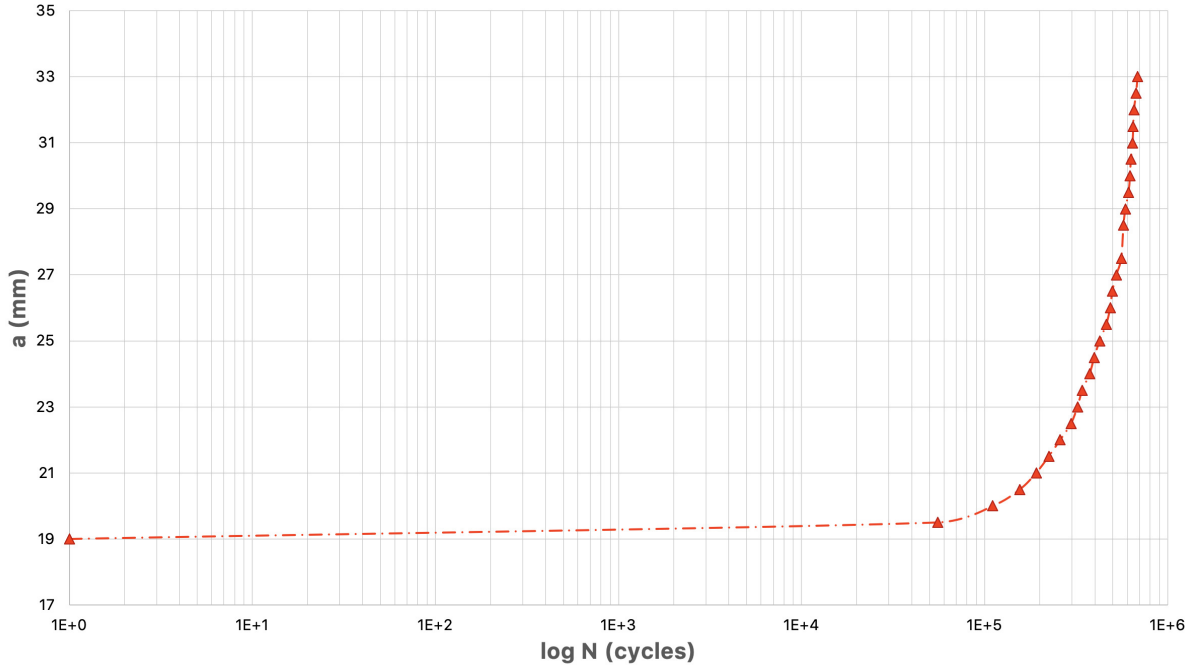


Figure 4.23: FCP behaviour in XFEM

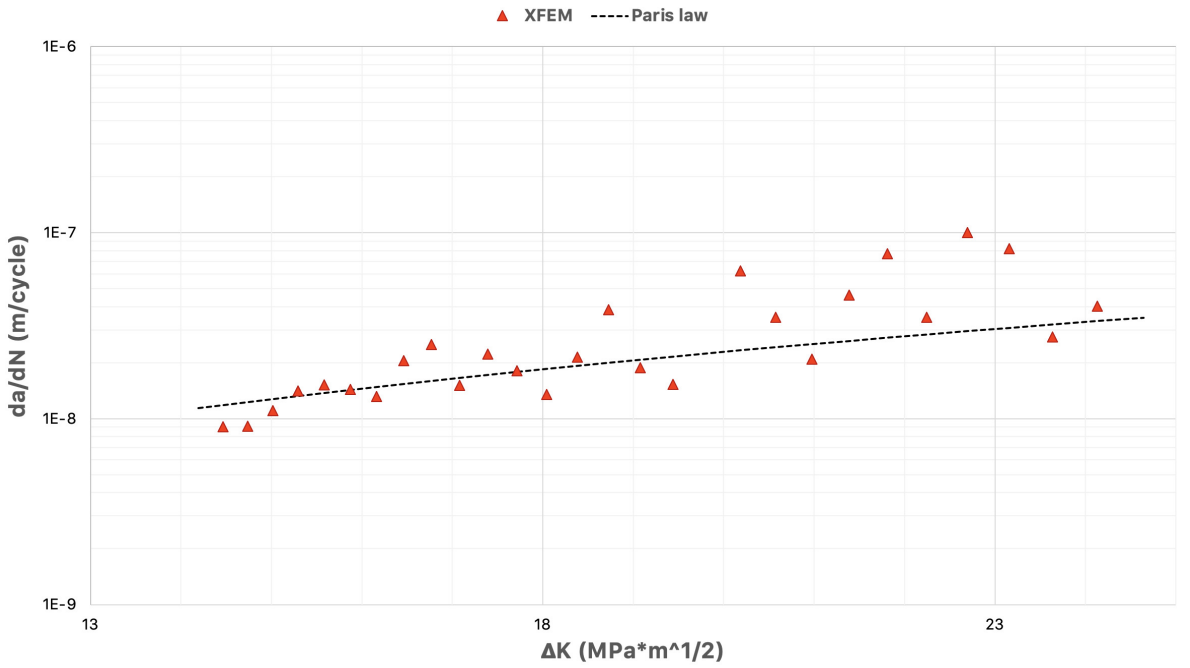


Figure 4.24: Graphical comparison of FCP rate between data withdrawn from XFEM and Paris law

### 4.2.3 Final remarks for Chapter 4

This chapter focused on thoroughly analyzing all the data collected from the experimental and numerical studies performed throughout this research. It was split into two parts to provide the reader a clear separation between the experimental and numerical analysis areas.

In the first section, within the material characterization, roughness measurements provided similar

results to what was found in the literature. Additionally, the linear profile surface revealed an existence of a small ”valley” left by the tool during FSW. Tensile tests were performed on two similar specimens and DIC was used to measure strain fields of characteristic FSW regions. One of them ruptured sooner than the other one and both of them showed an identical rupture pattern resembling the KB defect found in the following subsection. Microstructure analysis confirmed the grain refinement in SZ that leads to an improvement in mechanical and fatigue properties. On the other hand, it unveiled a defect on AS of the interface between SZ and TMAZ, commonly found in FSW joints. At last microhardness testing not only provided similar profiles and values found in the literature for the same material but also confirmed the hardening of the WN.

Experimental FCP suffered several unforeseen events that limited this study. Although not enough data was collected to draw valid conclusions, one of the specimens confirmed once again the existence of defects across the entire length of the joint.

At last, numerical analysis was performed on the modelled specimen with the help of Abaqus and XFEM. A static and dynamic investigations were carried out, with the first one to assess the accuracy of the model, and the second one to investigate the capabilities of the software in simulating FCP. In both cases, close results were obtained when compared to their theoretical counterpart. Moreover, in cyclic analysis, two mechanisms were found to be responsible for FCP, a regular and irregular.

# Chapter 5

# Conclusions and Future Works

## 5.1 Achievements

This research focused on performing a multi-subject investigation of a non heat-treated aluminium alloy, AA5083-H111, in the form of 5 mm sheets joined together using FSW. Among the various topics studied throughout, the spotlight of this master's thesis was to evaluate the FCP rate across the joint's typical regions and how each of them affects the speed of crack growth. To complement the research, a numerical study was carried out on a commercially available CAE software where an exact replica of CT specimen was modelled within an elastic domain.

In the course of this research project, a complete material characterization was performed on the FSWed joint from the mechanical and microstructural perspectives. Microstructure and microhardness analysis helped to define and limit welding regions, information that was taken into account in all phases of this study. Additionally, microstructure analysis unveiled the expected behaviour resulting from FSW process, where SZ underwent dynamic recrystallisation, promoting grain refinement in that area which impacted positively the mechanical properties of the material. The grain refinement and consecutive hardening of the region were later confirmed by the microhardness test curves, with 2 out of 3 displaying similar values and profiles to those found in the literature. The third curve displayed a dip in the SZ region which is explained by the proximity of the measurements to the surface where the shoulder was in contact with during welding and caused softening of that particular spot. Moreover, microstructural observations allowed to detect a common butt joint defect which at the same time promoted mechanical and fatigue degradation of the piece, as was observed in tensile tests, where both specimens presented lower mechanical properties when compared to the BM but also ruptured with a similar pattern to presented by the KB defect. The roughness of the joint surface was the last topic to be investigated in the material definition, which allowed to observe the formation of a *valley* in the central part of the weld width caused by the material being pushed to the outer parts of the joint. In this way, the first research question set in Chapter 1, *What mechanical and microstructural properties does the FSWed material present and how can they influence the outcome of FCP?* is addressed, without further remarks to be written.

Concerning the second research question of this project, *How does the crack behave when crossing characteristic FSW regions?*, this one remains unanswered due to several factors that limited this investigation and are explained in Section 5.2. The amount of data collected during experimental FCP does not allow for an in-depth overview and conclusions to be written.

As for the last question set for this investigation, *What capabilities does the Abaqus offer in FCP analysis and how reliable are the results when compared to the experimental study?*, it was possible to assess it partially, mostly due to limitations found in the experimental part of the study. Overall, Abaqus revealed very promising results when the object is correctly modelled into the software and the BC are accurately defined. Even with the simulations being performed on a domestic machine with a small amount of computer power, the SIF and FCP calculations revealed reliable results with reduced deviations when compared to their theoretical predictions. With that in mind, numerical studies of FCP not only can deliver viable results but also to bring economical benefits by saving resources and time on performing experimental studies.

In the end, there is a great potential in the application of FSW in a highly regulated industry such as aerospace, but much more research focused on FCP shall be carried out, either experimentally or numerically.

## 5.2 Limitations and future work recommendations

Unfortunately, this study was severely time-limited due to a combination of factors that were beyond anyone's control. The pandemic that struck the world, in conjunction with faulty fatigue testing equipment that did not allow for a satisfactory amount of data to be collected, led to an unsuccessful experimental study of FCP. Moreover, the FE study was limited by the available computational resources of the hardware used in the simulations, *i.e.*, portable computer with a quad-core CPU and 16 GB of RAM, leading to simulation times of several hours. For those reasons, several recommendations can be done regarding the development of future researches.

In the first place, with the aim to achieve a detailed study of FCP rate when traversing several characteristic FSW regions, this research can be done in a different way. A defect-free FSW joint must be obtained at the beginning of the investigation, either by doing a parametric study or by using an optimal set of parameters for a given material from the literature. Also, using a material with different mechanical properties that would allow for a greater load to be applied without sacrificing the valid domain of the crack length.

Another recommendation for the future work would be to simulate the FCP in an elasto-plastic environment. A more detailed analysis would include the calculation of Paris constants for every FSWed region during experimental procedures and the FE modelling of the specimen with each region being assigned different fracture criteria in respect to the constants determined previously.

At last, it would be interesting to observe the influence of different parameters and configurations of the FE model, namely the difference in FCP for a range of stress ratios or to assess the behaviour of the crack in 2D and 3D models.

# Bibliography


[1] M. Supermarkets. History Of Aluminum In The Aerospace Industry, Visited on 12/09/2019. URL https://www.metalsupermarkets.com/history-of-aluminum-in-the-aerospace-industry/.

[2] B. Smye. Aluminum Alloys for Aerospace, Visited on 12/09/2020. URL https://www.aerospacemanufacturinganddesign.com/article/aluminum-alloys-for-aerospace/.

[3] R. Rudrapati. Recent Advances in Joining of Aluminum Alloys by Using Friction Stir Welding. *IntechOpen*, Nov. 2019.

[4] TWI. What is Friction Stir Welding (FSW)? - Process and Aplications, Visited on 13/09/2020. URL https://www.twi-global.com/technical-knowledge/faqs/faq-what-is-friction-stir-welding.

[5] H. Li, J. Gao, and Q. Li. Fatigue of Friction Stir Welded Aluminum Alloy Joints: A Review. *Applied Sciences*, 8, 11 2018.

[6] M. Zadeh, A. Ali, A. F. Golestaneh, and B.B.Sahari. Analysis of Fatigue Crack Growth in Friction Stir Welded Joints of 2024 Al Alloy. 09 2009.

[7] P. Sivaraj, D. Kanagarajan, and V. Balasubramanian. Fatigue crack growth behaviour of friction stir welded AA7075-T651 aluminium alloy joints. *Transactions of Nonferrous Metals Society of China*, 8, 06 2014.

[8] G. Labeas and S. Peppa. Fatigue Crack Growth Behaviour of Friction Stir Welded Aluminium Alloys. *Key Engineering Materials*, 665:89–92, 09 2015.

[9] J. Das, S. Banik, S. Reddy, M. Sankara, and P. Robia. Review on process parameters effect on fatigue crack growth rate in friction stir welding. *Materials Today: Proceedings*, 18, 07 2019.

[10] N. Zhou, D. Song, W. Qi, X. Li, J. Zou, and M. M. Attallah. Influence of the Kissing Bond on the Mechanical Properties and Fracture Behaviour of AA5083-H112 Friction Stir Welds. *Materials Science & Engineering*, 18, 02 2018.

[11] L. Zhang, H. Zhong, S. Li, H. Zhao, J. Chen, and L. Qi. Microstructure, mechanical properties and fatigue crack growth behavior of friction stir welded joint of 6061-T6 aluminum alloy. *International Journal of Fatigue*, 135, 07 2020.

[12] P. Donga, Z. Liua, X. Zhaia, Z. Yana, W. Wanga, and P. K. Liaw. Incredible improvement in fatigue resistance of friction stir welded 7075-T651 aluminum alloy via surface mechanical rolling treatment. *International Journal of Fatigue*, 124:15–25, 02 2019.

[13] M. Ilman, Sehono, M. Muslihb, and H. Wibowo. The application of transient thermal tensioning for improving fatigue crack growth resistance of AA5083-H116 FSW joints by varying secondary heating temperature. *International Journal of Fatigue*, 133, 07 2020.

[14] M. A. Bozorgzadeh and M. Idris. Friction stir welding. *International Journal of Review in Life Sciences*, 5(3):72–75, Oct. 2015. ISSN:2231-2935.

[15] R. Mishra and Z. Ma. Friction-stir welding and processing. *Materials Science & Engineering*, (50): 1–78, 2005.

[16] N. E. International. Welding stir-up, Visited on 13/09/2020. URL `https://www.neimagazine.com/features/featurewelding-stir-up-4363560/featurewelding-stir-up-4363560-458584.html`.

[17] K. Fraser, L. St-Georges, and L. I. Kiss. A Mesh-Free Solid-Mechanics Approach for Simulating the Friction Stir-Welding Process. *IntechOpen*, 09 2016.

[18] C. He, Y. L. J. Dong, Q. Wang, D. Wagner, and C. Bathias. Fatigue crack initiation behaviors throughout friction stir welded joints in AA7075-T6 in ultrasonic fatigue. *International Journal of Fatigue*, 81, 12 2015.

[19] M. K. B. Givi and P. Asadi. *Advances in Friction-Stir Welding and Processing*. Woodhead Publishing, 2014. ISBN:978-0-85709-455-1.

[20] M. Srubar. Friction Stir Welding application, Visited on 13/09/2020. URL `http://www.fswelding.com/application-of-friction-stir-welding-in-aircraft-structures/fsw-application`.

[21] Friction Stir and Laser Beam Welding processes used in advanced joining of dissimilar materials. Technical Report ANM-112N-05-06, IDMEC, 08 2019.

[22] T. W. Institute. Friction Stir Welding of Airframe Structures, Visited on 24/09/2019. URL `https://www.twi-global.com/who-we-are/who-we-work-with/industry-sectors/aerospace/joining-of-airframe-structures/friction-stir-welding-of-airframe-structures`.

[23] M. Pacchione and J. Telgkamp. Challenges of the Metallic Fuselage. pages 1–12, 2006.

[24] A. Boitsov, D. Kuritsyn, M. Siluyanova, and V. Kuritsyna. Friction Stir Welding in the Aerospace Industry. *Russian Engineering Research*, 38:1029–1033, 12 2018.

[25] SpaceX. Falcon 9 progress update, Visited on 24/09/2019. URL `https://www.spacex.com/news/2013/02/11/falcon-9-progress-update-12`.

[26] T. W. Institute. A Flying Success Story For Friction Stir Welding, Visited on 24/09/2019. URL https://www.twi-global.com/media-and-events/connect/2003/january-february-2003/a-flying-success-story-for-friction-stir-welding.

[27] I. A. T. Association. IATA Forecast Predicts 8.2 billion Air Travelers in 2037, Visited on 30/09/2019. URL https://www.iata.org/pressroom/pr/Pages/2018-10-24-02.aspx.

[28] K. Gangwar and M. Ramulu. Friction stir welding of titanium alloys: A review. *Materials & Design*, 141:230–255, 2018.

[29] A. P. Mouritz. *Introduction to Aerospace Materials*, chapter 18 - Fracture processes of aerospace materials, pages 428–453. Woodhead Publishing, 2012. ISBN: 978-0-85709-515-2.

[30] S. Gürgen, M. Kushan, and S. Diltemiz. *Fatigue failure in aircraft structural components*, pages 261–277. 08 2015. ISBN: 978-0-12801-177-5.

[31] MechaniCalc. Fracture Mechanics, Visited on 01/12/2020. URL https://mechanicalc.com/reference/fracture-mechanics.

[32] A. A. Griffith. The Phenomena of Rupture and Flow in Solids. *Philosophical Transactions of the Royal Society of London, Series A, Containing Papers of a Mathematical or Physical Character*, 221:163–198, 1921.

[33] G. R. Irwin. Analysis of stresses and strains near the end of a crack traversing a plate. *Journal of Applied Mechanics*, 24:361–364, 1957.

[34] T. Hellen. *How To- Undertake Fracture Mechanics Analysis with Finite Elements*. NAFEMS, 2001. ISBN:978-1-87437-640-8.

[35] J. Schijve. *Fatigue of Structures and Materials*, chapter Stress Intensity Factors of Cracks, pages 105–140. Springer, 2009. ISBN: 978-1-4020-6808-9.

[36] Fracture Mechanics, Visited on 04/12/2020. URL https://en.wikipedia.org/wiki/Fracture_mechanics#/media/File:Fracture_modes_v2.svg.

[37] J. Qian and A. Fatemi. Mixed mode fatigue crack growth: A literature survey. *Engineering Fracture Mechanics*, 55:969–990, 1996.

[38] Y.-S. Wu. *Hydraulic Fracture Modeling*. Gulf Professional Publishing, 2018. ISBN:978-0-12812-999-9.

[39] T. L. Anderson. *Fracture Mechanics: Fundamentals and Applications*. CRC Press, 2004. ISBN:978-0-84931-656-2.

[40] M. Schiaretti. Numerical Simulation of Fatigue Crack Growth in a Stiffened Plate. Master's thesis, Delft University of Technology, 09 2017.

[41] W. D. Callister and D. G. Rethwisch. *Materials Science and Engineering: An Introduction*. John Wiley & Sons, 2013. ISBN:978-1-11832-457-8.

[42] N. Perez. *Fracture Mechanics*, chapter Fatigue Crack Growth, pages 199–238. Springer, 2004. ISBN: 978-1-4020-7861-3.

[43] D. Liu and D. J. Pons. Crack Propagation Mechanisms for Creep Fatigue: A Consolidated Explanation of Fundamental Behaviours from Initiation to Failure. *Metals*, 623:230–255, 2018.

[44] A. P. Mouritz. *Introduction to Aerospace Materials*, chapter 20 - Fatigue of aerospace materials, pages 469–497. Woodhead Publishing, 2012. ISBN: 978-0-85709-515-2.

[45] P. Paris and F. Erdogan. A Critical Analysis of Crack Propagation Laws. *Journal of Basic Engineering*, 85:528–533, 1963.

[46] M. Turner, R. Clough, H. Martin, and L. Topp. Stiffness and Deflection Analysis of Complex Structures. *Journal of the Aeronautical Sciences*, 23, 09 1956.

[47] D. V. Swenson and A. R. Ingraffea. Modeling mixed-mode dynamic crack propagation using finite elements: Theory and applications. *Computational Mechanics*, 3:381–397, 09 1988.

[48] X.-P. Xu and A. Needleman. Numerical Simulations of Fast Crack Growth in Brittle Materials. *Journal of the Mechanics and Physics of Solids*, 9:1397–1434, 1994.

[49] J.-H. Song, P. M. Areias, and T. Belytschko. A method for dynamic crack and shear band propagation with phantom nodes. *International Journal for Numerical Methods in Engineering*, 67:868–893, 02 2006.

[50] T. Belytschko and T. Black. Elastic Crack Growth in Finite Elements with Minimal Remeshing. *International Journal for Numerical Methods in Engineering*, 45:601–620, 1999.

[51] C. Duarte, O. Hamzeh, T. Liszka, and W. Tworzydlo. A generalized finite element method for the simulation of three-dimensional dynamic crack propagation. *Computer Methods in Applied Mechanics and Engineering*, 190:2227–2262, 2001.

[52] J. Melenk and I. Babuška. The partition of unity finite element method: Basic theory and applications. *Computer Methods in Applied Mechanics and Engineering*, 139:289–314, 1996.

[53] N. Moës, J. Dolbow, and T. Belytschko. A Finite Element Method for Crack Growth Without Remeshing. *International Journal for Numerical Methods in Engineering*, 46:131–150, 1999.

[54] Dassault Systèmes SIMULIA Corp. Abaqus Documentation 2017. .

[55] Dassault Systèmes SIMULIA Corp. Abaqus Documentation 2016. .

[56] A. Solob, A. Grbovic, Z. Bozic, and S. Sedmak. XFEM based analysis of fatigue crack growth in damaged wing fuselage attachment lug. *Engineering Failure Analysis*, 112, 2020.

[57] M. Nikfama, M. Zeinoddinia, F. Aghebatia, and A. Arghaei. Experimental and XFEM modelling of high cycle fatigue crack growth in steel welded T-joints. *International Journal of Mechanical Sciences*, 153-154:178–193, 2019.

[58] M. Kumar, V. Pandey, I. Singh, B. Mishra, S. Ahmad, A. Rao, and V. Kumar. A Numerical Study of Creep Crack Growth in an Aero-engine Turbine Disc using XFEM. *Procedia Structural Integrity*, 14:839–848, 2019.

[59] B. Wang, H. D. Backer, and A. Chen. An XFEM based uncertainty study on crack growth in welded joints with defects. *Theoretical and Applied Fracture Mechanics*, 86B:125–142, 2016.

[60] A. Bergara, J. Dorado, A. Martin-Meizoso, and J. Martínez-Esnaola. Fatigue crack propagation in complex stress fields: Experiments and numerical simulations using the Extended Finite Element Method (XFEM). *International Journal of Fatigue*, 103:112–121, 10 2017.

[61] T. London, D. D. Bono, and X. Sun. An evaluation of the low cycle fatigue analysis procedure in Abaqus for crack propagation: numerical benchmarks and experimental validation. pages 1–15, 11 2015.

[62] T. Aluminum Association. Aluminum Alloys 101, Visited on 22/11/2020. URL `https://www.aluminum.org/resources/industry-standards/aluminum-alloys-101`.

[63] E. Canepa, R. Stifanese, L. Merotto, and P. Traverso. Corrosion behaviour of aluminium alloys in deep-sea environment: A review and the KM3NeT test results. *Marine Structures*, 54:271–284, 05 2018.

[64] C. Vidal, V. Infante, and P. Vilaça. Fatigue behaviour at elevated temperature of friction stir channelling solid plates of AA5083-H111 aluminium alloy. *International Journal of Fatigue*, 62:85–92, 10 2014.

[65] R. Stahl. What is Electrical Discharge Machining and how does it work?, Visited on 22/11/2020. URL `https://www.etmm-online.com/what-is-electrical-discharge-machining-and-how-does-it-work-a-689686/`.

[66] ASTM E647-00. Standard Test Method for Measurement of Fatigue Crack Growth Rates. Standard, ASTM International, West Conshohocken, PA, 2000.

[67] ASTM E8/E8M-13a. Standard Test Methods for Tension Testing of Metallic Materials. Standard, ASTM International, West Conshohocken, PA, 2013.

[68] R. E. Brister. Using Digital Image Correlation to Measure Large Areas of Strain and Displacement, Visited on 30/11/2020. URL `https://www.stress.com/dic-to-measure-large-areas-of-strain-displacement/`.

[69] Keyence. White light interferometers, Visited on 13/11/2020. URL `https://www.keyence.com/ss/products/microscope/roughness/equipment/interferometers.jsp`.

[70] O. J.D. Fracture mechanics and mechanical behaviour in AA5083-H111 friction stir welds. *Scientific African*, 8, 07 2020.

[71] C. Genevoisa, A. Deschampsa, A. Denquinb, and B. Doisneau-Cottignies. Quantitative investigation of precipitation and mechanical behaviour for AA2024 friction stir welds. *Acta Materialia*, 53: 2447–2458, 05 2005.

[72] G. England. Vickers Hardness Test, Visited on 28/11/2020. URL `https://www.gordonengland.co.uk/hardness/vickers.htm`.

[73] A. R. Shahani, I. Shakeri, and C. D. Rans. Fatigue crack growth of Al 5083-H111 subjected to mixed-mode loading. *Journal of the Brazilian Society of Mechanical Sciences and Engineering*, 42, 08 2020.

[74] R. K. Bhushan and D. Sharma. Investigation of mechanical properties and surface roughness of friction stir welded AA6061-T651. *International Journal of Mechanical and Materials Engineering*, 15, 06 2020.

[75] V. Prakash, D. R. Kumar, A. Horn, H. Hagenah, and M. Merklein. Modeling material behavior of AA5083 aluminum alloy sheet using biaxial tensile tests and its application in numerical simulation of deep drawing. *The International Journal of Advanced Manufacturing Technology*, 10 2019.

[76] P. Tayebi, A. Fazli, P. Asadi, and M. Soltanpour. Formability analysis of dissimilar friction stir welded AA 6061 and AA 5083 blanks by SPIF process. *CIRP Journal of Manufacturing Science and Technology*, 25, 03 2019.

[77] J. Torzewski, K. Grzelak, M. Wachowski, and R. Kosturek. Microstructure and Low Cycle Fatigue Properties of AA5083 H111 Friction Stir Welded Joint. *Materials*, 05 2020.

[78] M. Ahmed, M. Habba, A. Mohamed, and A. EL-Nikhaily. Effect of friction stir welding parameters on the mechanical properties of AA5083-H111. 05 2014.

[79] D. Hrishikesh and D. Chakraborty. High-cycle fatigue behavior of friction stir butt welded 6061 aluminium alloy. *Transactions of Nonferrous Metals Society of China*, 4:648–656, 05 2014.

[80] C. EU. Detection of kissing bonds in friction stir welds of aero structures and automotive components., Visited on 27/11/2020. URL `https://cordis.europa.eu/article/id/117276-detection-of-kissing-bonds-in-friction-stir-welds-of-aero-structures-and-automotive-comp`

[81] J. Schneider, P. Chen, and A. C. N. Jr. Formation of oxides in the interior of friction stir welds. 05 2016.

[82] P. Vilaça, N. Pépe, and L. Quintino. Metallurgical and Corrosion Features of Friction Stir Welding of AA5083-H111. *Welding in the World*, 50:55–64, 05 2006.

# Appendix A

# Roughness data

Table A.1: All $R_a$ measurements taken from the analyzed specimen. Units are in $\mu m$

| | | 1 | 2 | 3 | 4 | 5 | 6 | Mean | Total Mean Value |
|---|---|---|---|---|---|---|---|---|---|
| TMAZ AS | A | 1,169 | 0,663 | 1,126 | 0,963 | 0,819 | 0,789 | 0,921 | 1,016 |
| | B | 1,053 | 1,108 | 0,681 | 0,853 | 0,943 | 1,151 | 0,965 | |
| | C | 1,555 | 0,870 | 1,299 | 1,292 | 1,149 | 0,894 | 1,177 | |
| | D | 0,775 | 0,907 | 1,151 | 1,098 | 1,097 | 0,799 | 0,971 | |
| | E | 0,817 | 0,891 | 1,265 | 1,129 | 1,296 | 0,879 | 1,046 | |
| SZ | A | 0,691 | 0,606 | 0,493 | 0,843 | 1,020 | 0,837 | 0,748 | 0,914 |
| | B | 0,623 | 0,883 | 0,525 | 1,048 | 0,821 | 0,810 | 0,785 | |
| | C | 0,944 | 0,950 | 1,049 | 0,883 | 1,253 | 0,979 | 1,010 | |
| | D | 0,748 | 1,020 | 0,877 | 1,530 | 1,000 | 1,091 | 1,044 | |
| | E | 0,772 | 0,842 | 0,895 | 0,999 | 1,129 | 1,247 | 0,981 | |
| TMAZ RS | A | 0,917 | 1,016 | 1,113 | 1,322 | 1,266 | 1,048 | 1,114 | 1,113 |
| | B | 1,104 | 1,051 | 1,244 | 0,856 | 1,689 | 0,845 | 1,132 | |
| | C | 1,208 | 0,913 | 1,344 | 1,229 | 0,967 | 1,017 | 1,113 | |
| | D | 1,099 | 1,303 | 1,335 | 1,075 | 1,072 | 1,043 | 1,155 | |
| | E | 1,490 | 1,208 | 0,788 | 0,919 | 0,994 | 0,927 | 1,054 | |

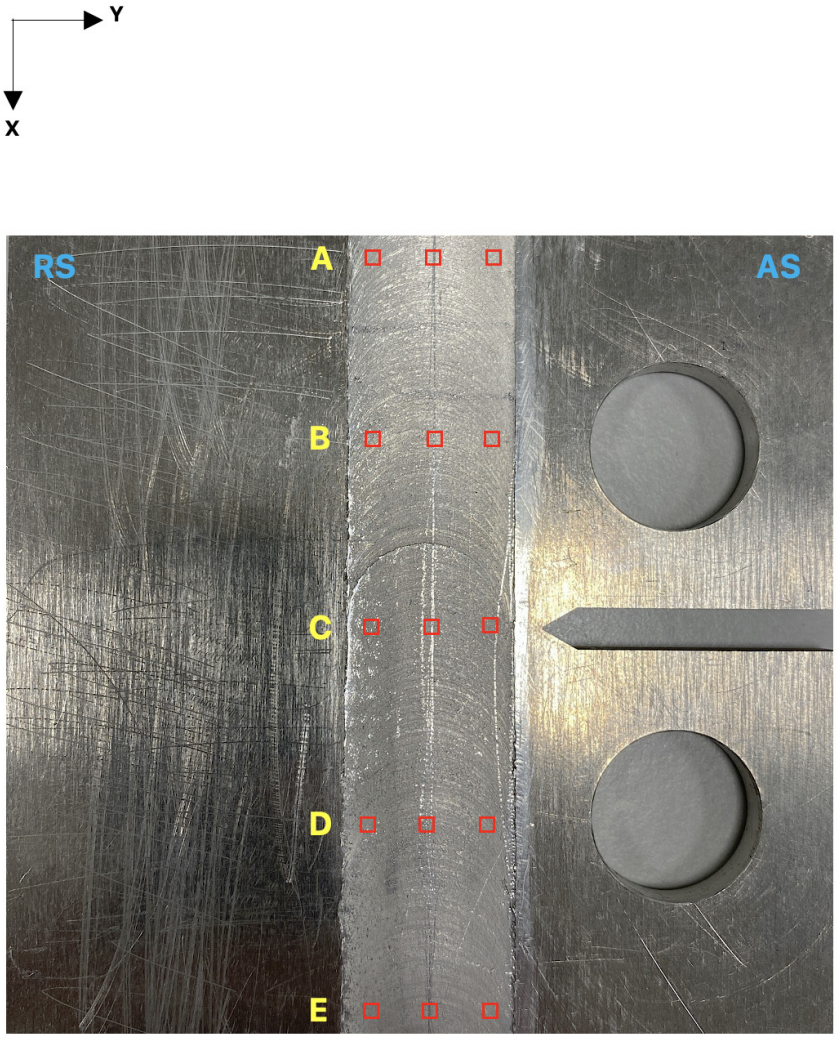


Table A.2: Measurement areas for surface roughness